UNIVERSITAT ROVIRA I VIRGILI

Development of wearable electronic devices, on low-cost flexible support for gas sensing Applications

Alejandro Santos Betancourt

ADVERTIMENT. L'accés als continguts d'aquesta tesi doctoral i la seva utilització ha de respectar els drets de la persona autora. Pot ser utilitzada per a consulta o estudi personal, així com en activitats o materials d'investigació i docència en els termes establerts a l'art. 32 del Text Refós de la Llei de Propietat Intel·lectual (RDL 1/1996). Per altres utilitzacions es requereix l'autorització prèvia i expressa de la persona autora. En qualsevol cas, en la utilització dels seus continguts caldrà indicar de forma clara el nom i cognoms de la persona autora i el títol de la tesi doctoral. No s'autoritza la seva reproducció o altres formes d'explotació efectuades amb finalitats de lucre ni la seva comunicació pública des d'un lloc aliè al servei TDX. Tampoc s'autoritza la presentació del seu contingut en una finestra o marc aliè a TDX (framing). Aquesta reserva de drets afecta tant als continguts de la tesi com als seus resums i índexs.

ADVERTENCIA. El acceso a los contenidos de esta tesis doctoral y su utilización debe respetar los derechos de la persona autora. Puede ser utilizada para consulta o estudio personal, así como en actividades o materiales de investigación y docencia en los términos establecidos en el art. 32 del Texto Refundido de la Ley de Propiedad Intelectual (RDL 1/1996). Para otros usos se requiere la autorización previa y expresa de la persona autora. En cualquier caso, en la utilización de sus contenidos se deberá indicar de forma clara el nombre y apellidos de la persona autora y el título de la tesis doctoral. No se autoriza su reproducción u otras formas de explotación efectuadas con fines lucrativos ni su comunicación pública desde un sitio ajeno al servicio TDR. Tampoco se autoriza la presentación de su contenido en una ventana o marco ajeno a TDR (framing). Esta reserva de derechos afecta tanto al contenido de la tesis como a sus resúmenes e índices.

WARNING. Access to the contents of this doctoral thesis and its use must respect the rights of the author. It can be used for reference or private study, as well as research and learning activities or materials in the terms established by the 32nd article of the Spanish Consolidated Copyright Act (RDL 1/1996). Express and previous authorization of the author is required for any other uses. In any case, when using its content, full name of the author and title of the thesis must be clearly indicated. Reproduction or other forms of for profit use or public communication from outside TDX service is not allowed. Presentation of its content in a window or frame external to TDX (framing) is not authorized either. These rights affect both the content of the thesis and its abstracts and indexes.

UNIVERSITAT
ROVIRA i VIRGILI

Development of wearable electronic devices, on low-cost flexible support for gas sensing applications

---

ALEJANDRO SANTOS BETANCOURT

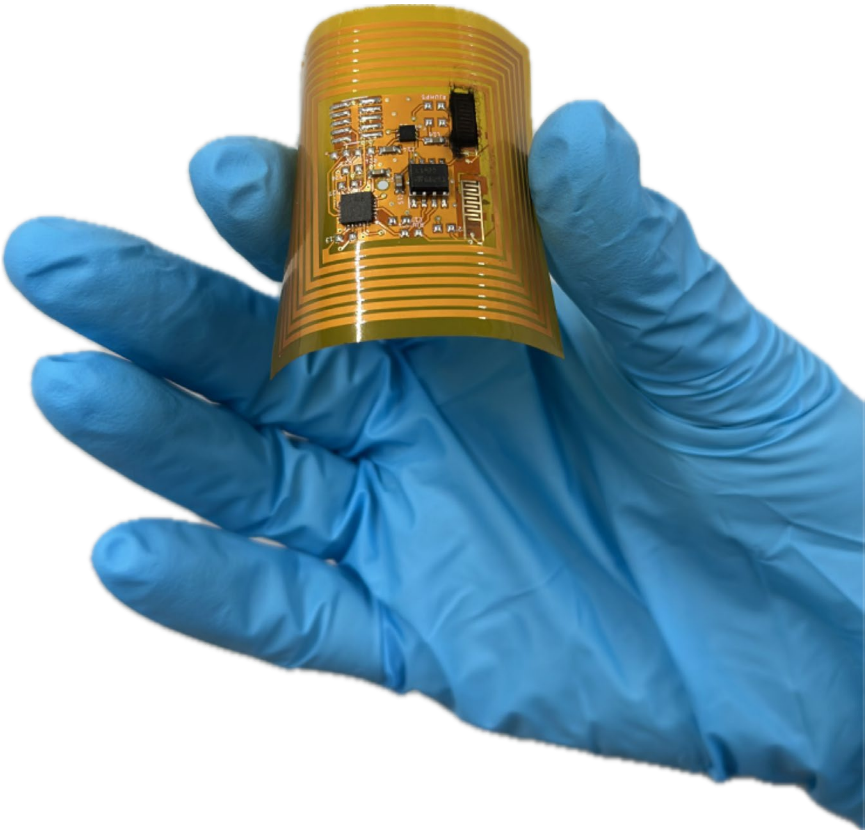

DOCTORAL THESIS

2024

DOCTORAL THESIS

Development of wearable electronic devices, on low-cost flexible support for gas sensing applications

Ph.D. Thesis
Alejandro Santos Betancourt

Supervised by:
Prof. Alfonso José Romero Nevado
Prof. José Luis Ramírez Falo

Department of
Electronic, Electrical, and Automation Engineering

UNIVERSITAT ROVIRA i VIRGILI

Tarragona
2024

UNIVERSITAT ROVIRA i VIRGILI

FAIG CONSTAR que aquest treball, titulat “Development of wearable electronic devices, on low-cost flexible support for gas sensing applications”, que presenta Alejandro Santos Betancourt per a l’obtenció del títol de Doctor, ha estat realitzat sota la meva direcció al Departament d’Enginyeria Electrònica, Elèctrica i Automàtica d’aquesta universitat.

HAGO CONSTAR que el presente trabajo, titulado “Development of wearable electronic devices, on low-cost flexible support for gas sensing applications”, que presenta Alejandro Santos Betancourt para la obtención del título de Doctor, ha sido realizado bajo mi dirección en el Departamento de Ingeniería Electrónica, Eléctrica y Automática de esta universidad.

I STATE that the present study, entitled “Development of wearable electronic devices, on low-cost flexible support for gas sensing applications”, presented by Alejandro Santos Betancourt for the award of the degree of Doctor, has been carried out under my supervision at the Department of Electronic, Electrical and Automation Engineering of this university.

Tarragona, 24th November 2024

Els directors de la Tesi Doctoral
Los directores de la Tesis Doctoral
Doctoral Thesis Supervisors

Prof. Alfonso José Romero Nevado

Prof. José Luis Ramírez Falo

**"… caminante, no hay camino,
se hace camino al andar, …"**

Acknowledgments

I would like to express my deepest gratitude to all professors at Minos' research group: Alfonso Romero, José Luis Ramírez, Xavier Vilanova, and Eduard Llobet, whose expertise, patience, and solid support were crucial in completing this work. Their guidance not only provided me with academic clarity but also motivated me during moments of doubt.

My gratitude also extends to my colleagues and collaborators who participated in this research, especially to José Carlos, Foad, Xavi, Èric, Ayoub, and Shuja. You guys pushed me to move forward and overcome challenges.

To my family, I am profoundly grateful for their unconditional love and constant support. Their faith in me has been the driving force that allowed me to complete this journey. To my wife, for her patience, because living with a doctoral student is not an easy task. Without you, this achievement would not have been possible.

To my friends, thank you for your companionship and support during moments of stress and joy. You were my safety net, and your friendship helped me stay positive during the toughest moments. Grichar, Piro, Fono, Bistel, and Mawa, each of you contributed to making this process more bearable and meaningful.

Finally, I would like to say that this thesis is the result of collective effort. To all of you, thank you for being part of this journey.

Table of content

Resum

Aquesta tesi combina materials de baixa dimensió per a la detecció de gasos amb dispositius electrònics per recopilar dades ambientals com la contaminació i la qualitat de l'aire. La tesi aborda la base de coneixements per dissenyar i desenvolupar dispositius portàtils en suports flexibles de baix cost per monitoritzar l'exposició humana a gasos objectiu. La tesi integra conceptes de ciència de materials, electrònica i anàlisi de dades, i es divideix en quatre parts principals.

La primera part proporciona dades estadístiques històriques sobre gasos contaminants i la seva relació amb el benestar humà, destacant la importància d'obtenir una alta precisió de mesura en aplicacions de detecció de gasos. Presenta una visió general dels sensors de gasos i les principals característiques que haurien de tenir les properes generacions de dispositius electrònics per a aquestes aplicacions, com IoT i ANNs.

En segon lloc, es va utilitzar AACVD per sintetitzar sensors basats en WO_3. Es van avaluar les respostes dels sensors davant de gasos oxidants i reductors com NO_2, EtOH i H_2. Les dades mesurades es van recollir amb una matriu de sensors i es van processar utilitzant un enfocament multivariant. A continuació, es van emprar PCA y MLP per obtenir una alta capacitat de discriminació i quantificació dels gasos.

En tercer lloc, es va dissenyar i configurar una plataforma de nivell de preparació tecnològica (TRL-4) per interconnectar aquest tipus de sensors de gasos químico-resistius. La plataforma consta de diversos nodes connectats a un servidor centralitzat mitjançant el protocol MQTT de IoT. Es presenta una metodologia per configurar la plataforma quan es desplega en diferents escenaris o s'interconnecta amb altres sensors. Per desenvolupar aquesta metodologia es van mesurar dos gasos contaminants, NO_2 i NH_3, tant de manera individual (sota variacions de % HR) com en la seva mescla. Es proporcionen tots els detalls sobre el disseny del maquinari, el programari i el procés d'entrenament de ANNs.

La secció final de la tesi presenta la fabricació de sensors basats en grafè que incorporen elèctrodes interdigitats en la mateixa placa de circuit

imprès flexible que els components electrònics. Els sensors basats en grafè es van obtenir mitjançant la tècnica de deposició per aerografia. Es va fabricar un dispositiu portàtil acumulatiu amb comunicació NFC per a aplicacions de detecció de NO_2. El dispositiu portàtil obtingut es pot fixar fàcilment a una armilla de treball, permetent una integració senzilla en qualsevol entorn laboral. Cal destacar que les propietats estructurals, les característiques morfològiques i les composicions químiques de tots els sensors fabricats es van verificar utilitzant tècniques com FESEM, EDX, XRD, espectroscòpia Raman, HR-TEM i ToF-SIMS.

Abstract

This thesis combines low-dimensional materials for gas sensing with electronic devices to collect environmental data such as pollution and air quality. The thesis reaches the knowledge base of designing and developing wearable devices on low-cost flexible support to monitor humans' exposure to target gases. The thesis integrates concepts from materials science, electronics, and data analysis and it is divided into four main parts.

The first part gives historical statistical data on pollutant gases and their relationship with human well-being, highlighting the importance of obtaining high measurement precision on gas sensing applications. It presents an overview of gas sensors and the main characteristics next-generation electronics for gas sensing applications should have such as IoT and ANNs.

Second, aerosol-assisted chemical vapor deposition (AACVD) was used to synthesize WO_3-based sensors on alumina substrates with platinum-interdigitated electrodes. Sensors´ responses were evaluated towards oxidizing and reducing gases such as NO_2, EtOH, and H_2. Measured data was collected as a sensor array and was processed using a multivariate approach. Then, Principal Component Analysis and Multilayer Perceptron were employed to obtain high discrimination and quantization ability of the target gases.

Third, to interface this type of chemoresistor gas sensors a technology readiness level (TRL-4) platform was designed and set up. The platform consists of several nodes (electronics boards) connected to a centralized server using the MQTT IoT protocol. A methodology is presented to set up the platform when deployed in different scenarios or interfacing with other sensors. To develop this methodology two pollutant gases were measured, NO_2 and NH_3, in a single form (under % RH variation) and under their mixture. Full details about the design of hardware, software, and ANNs training process are given.

The final section of the thesis presents the fabrication of graphene-based sensors incorporating interdigitated electrodes in the same flexible printed circuit board as the electronics. Graphene-based sensors were obtained using the airbrushing deposition technique. A cumulative near-field communication (NFC) wearable for NO_2 sensing applications was fabricated. The obtained wearable device can be easily attached to a working vest allowing simple integration in any working environment. It is worth mentioning that the structural properties, morphological characteristics, and chemical compositions of all fabricated sensors were checked using techniques such as FESEM, EDX, XRD, Raman spectroscopy, HR-TEM, and ToF-SIMS.

Resumen

Esta tesis combina materiales de baja dimensión para la detección de gases con dispositivos electrónicos para recopilar datos ambientales como la contaminación y la calidad del aire. La tesis aborda la base de conocimientos para diseñar y desarrollar dispositivos portátiles en soportes flexibles de bajo costo para monitorizar la exposición humana a gases objetivo. La tesis integra conceptos de ciencia de materiales, electrónica y análisis de datos, y se divide en cuatro partes principales.

La primera parte proporciona datos estadísticos históricos sobre gases contaminantes y su relación con el bienestar humano, destacando la importancia de obtener una alta precisión de medición en aplicaciones de detección de gases. Presenta una visión general de los sensores de gases y las principales características que deberían tener las próximas generaciones de dispositivos electrónicos para estas aplicaciones, como IoT y ANNs.

En segundo lugar, se utilizó aerosol-assisted chemical vapor deposition (AACVD) para sintetizar sensores basados en WO_3 en sustratos rígidos de alúmina con electrodos interdigitados de platino. Se evaluaron las respuestas de los sensores frente a gases oxidantes y reductores como NO_2, EtOH y H_2. Los datos medidos se recopilaron con una matriz de sensores y se procesaron utilizando un enfoque multivariable. Luego, se emplearon Principal Component Analysis y Multilayer Perceptron para obtener una alta capacidad de discriminación y cuantificación de los gases.

En tercer lugar, se diseñó y configuró una plataforma de nivel de preparación tecnológica (TRL-4) para interconectar este tipo de sensores de gas químico-resistivos. La plataforma consta de varios nodos (placas electrónicas) conectados a un servidor centralizado utilizando el protocolo MQTT de IoT. Se presenta una metodología para configurar la plataforma cuando se despliega en diferentes escenarios o se interconecta con otros sensores. Para desarrollar esta metodología se midieron dos gases contaminantes, NO_2 y NH_3, tanto de forma individual (bajo variaciones de % HR) como en su mezcla. Se

proporcionan todos los detalles sobre el diseño del hardware, el software y el proceso de entrenamiento de ANNs.

La sección final de la tesis presenta la fabricación de sensores basados en grafeno que incorporan electrodos interdigitados en la misma placa de circuito flexible que los componentes electrónicos. Los sensores basados en grafeno se obtuvieron utilizando la técnica de deposición airbrushing. Se fabricó un dispositivo wearable acumulativo con comunicación NFC para aplicaciones de detección de NO_2. El dispositivo wearable obtenido puede acoplarse fácilmente a un chaleco de trabajo, permitiendo una integración sencilla en cualquier entorno laboral. Cabe mencionar que las propiedades estructurales, características morfológicas y composiciones químicas de todos los sensores fabricados se verificaron utilizando técnicas como FESEM, EDX, XRD, espectroscopía Raman, HR-TEM y ToF-SIMS.

Chapter 1

Introduction

1. Introduction

1.1. Air pollution and human health relationship

Air pollution is a significant global health and environmental issue affecting people's well-being worldwide. It can be classified as ambient pollution related to outdoor scenarios and household pollution often named indoor air pollution; both are the second risk factor for death globally. In the past ten years, more than 80 million people passed away due to illnesses caused by breathing contaminated air [1]. Nowadays the World Health Organization (WHO) estimates that air pollution takes around seven million people's lives worldwide every year [2].

Indoor and outdoor pollution are caused by stoves for cooking, fueled by kerosene, biomass, and coal; and emissions from industrial facilities, vehicles, power generation, and agricultural waste, respectively. Because of these, most of the global population is exposed daily to different contaminants. In some cases, the presence of these pollutants exceeds the WHO guideline limits. For instance, exposure to NO_2 could harm the human respiratory system, is fatal if inhaled, and causes severe skin burns and eye damage [3]. Another hazardous and important gas in atmospheric chemistry is NH_3, which causes severe skin burns and eye damage, is toxic if inhaled, is very dangerous to aquatic life and is a flammable gas. Other common pollutant gases can be found in Figure 1.

The figure shows the change in the world's emissions of pollutant gases since 2010. It is noticed that the emission of NH_3 has increased by 10 %, emissions of non-methane volatile organic compounds (VOCs) have been stable, and NO_2, CO, SO_X, and other carbon-based emissions (Organic Carbon, Black Carbon) have been decreasing in this period [4]. These pollutants are mainly used in industrial facilities and agricultural activities. According to the International Labour Organization (ILO) from the United Nations, 1.6 billion workers are probably to be exposed to air pollution, resulting in up to 860 thousand work-related losses of life among outdoor workers annually. Over 870 million workers in agriculture, are likely to be exposed to pesticides, with more than 300 thousand fatalities attributed to pesticide poisoning annually [5].

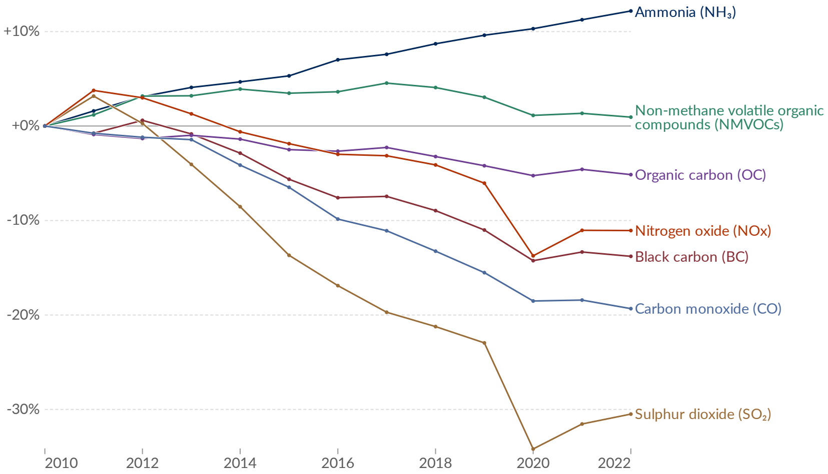

Figure 1: Change in the emissions of air pollutants from 2010 to 2022 [4].

There are some regulations and standards for the number of emissions and exposure times to comply with to protect workers and the environment from breathing or being exposed to contaminated air. For instance, the European Chemicals Agency (ECHA) establishes the Occupational Exposure Limits (OELs) in a Long-Term Period Limit (LTEL) for NO_2 is 0.5 ppm and the OELs in a Short-Term Period Limit (STEL) is 1 ppm. In the case of NH_3, the LTEL is 20 ppm and STEL is 50 ppm, to mention some [3].

1.2. Types of gas sensors

The first step to fulfilling regulations and helping to reduce pollution is to have reliable and robust gas sensors. In past decades, many research efforts have been directed at creating gas sensors aiming to enhance sensors’ response and selectivity to specific target analytes. Also, improving their durability and long-term stability.

Different types of gas sensors have been developed such as electrochemical gas sensors. They use oxidation-reduction reactions to measure gas concentration. They are good for detecting toxic gases and are resistant to interferences but have short lifespans. On the other hand, optical sensors such as photoionization gas sensors (PID) use ultraviolet light to ionize gases for detection. They are highly sensitive to volatile organic compounds (VOCs). Non-dispersive infrared (NDIR) gas sensors use infrared light absorption to detect gases. They are highly accurate and long-lasting; they can detect CO_2 and other gases that absorb infrared light. Another type of gas sensor is the thermal conductivity sensor, Pellistors. They measure gas concentration based on thermal conductivity differences and can detect high concentrations but have low accuracy and sensitivity [6,7].

Among all these types of gas sensors, this thesis uses chemoresistor sensors: semiconductor metal oxides (MOXs) and graphene-based sensors. Both can detect gases by measuring changes in the electrical resistance of a semiconductor material. They are sensitive to many gases and have fast response and recovery times. They have a drawback by being susceptible to environmental factors such as the variation of % RH and ambient temperature [7,8]. MOXs work better at high temperatures, but graphene-based sensors can operate at room temperature, which is suitable for use in battery-powered systems since they have low power consumption [9].

Both types are built in simple steps. The manufacturing process is easy and low-cost. A sensitive layer is deposited on top of the IDEs. The IDEs are used to acquire the variation in the electrical conductivity of the sensitive layer while reacting with the target gas [10]. For example, p-type materials like graphene reacting with an oxidant gas such as NO_2 increase the electrical conductivity, therefore, its electrical resistance will drop in value proportional to the analyte concentration in contact with the sensitive layer. This simple mechanism allows chemoresistor sensors to have a simple read-out chain design and cheap maintenance costs. Therefore, they are appropriate for build-in with commercial intelligent electronics to monitor, process, and send their data remotely.

Figure 2 shows a general block diagram describing the integration of chemoresistor sensors with smart electronics. The main parts are highlighted as the IDEs, the chemoresistor gas-sensitive material, the substrate, and the smart electronics.

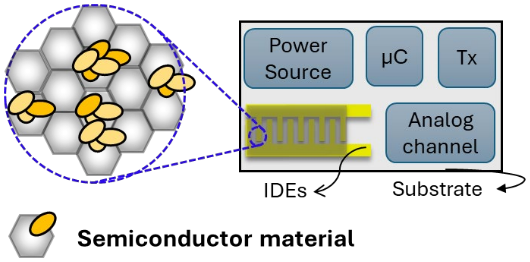

Figure 2: Integration process of chemoresistor gas sensors with intelligent electronics.

1.2.1. IDEs

IDEs interconnect the gas-sensitive materials with the smart electronics. Traditionally, thin films of conducting materials are used for this purpose like Au [11], Ag [12], Pt [13], and Al [14,15]. When choosing them, particular attention should be paid to their high electrical conductivity and adhesion to the selected substrate. It is important to highlight that in some applications, the flexibility of those conducting layers is desirable. Ideally, good IDEs must retain high conductivity even under extreme mechanical deformation. One of the most used geometry and dimensions of IDEs by researchers is presented in Figure 3. Note that IDEs have 5 pairs of fingers; the width and gap distance between them are 300 μm, and the length is 1.90 mm. This is the selected geometry for this thesis to be comparable with other published results. IDEs were purchased from CeramTech GmbH, Plochingen, Germany.

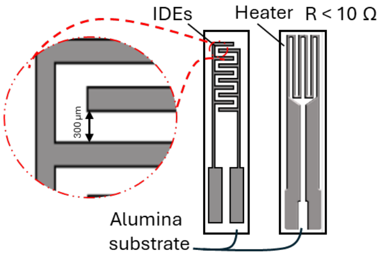

Figure 3: Geometry of IDEs.

1.2.2. *Chemoresistor gas-sensitive material*

MOXs exhibit a great variety of functional properties making them ideal for gas sensing applications. MOXs' functional properties are strongly determined by their crystalline structure, composition, native defects, and doping, among other parameters. These parameters influence their electrical, chemical, and mechanical characteristics. Growth parameters influence the morpho-structural characteristics and therefore their physicochemical properties [16]. Different growing techniques can be envisaged for building a MOXs-based sensor, such as liquid-phase (LPS) and vapor-phase synthesis (VPS). LPS enables obtaining different morphologies for the sensing layer, like nanoplates, nanowires, and nanorods [17]. Likewise, using VPS the thickness of the sensing layer can be controlled by optimizing the deposition parameters such as temperature, gas flow, solvents, and precursors [18]. One of the most used methods of VPS is aerosol-assisted chemical vapor deposition (AACVD) [19]. In the literature, several oxide structures have been reported by researchers to enable gas sensing applications such as WO_3 [20], In_2O_3 [21], Co_3O_4 [22], Cr_2O_3 [23], CeO_2 [24], MgO [25], MnO_2 [26], Al_2O_3 [27], CuO [28], and Fe_2O_3 [26]. On the other hand, carbon-based nanomaterials such as carbon nanotubes (CNTs) [29], graphene [30], and reduced graphene oxide (rGO) [31] have been explored for gas sensing applications due to their room temperature operation ability, and outstanding chemical and physical properties [32]. Different deposition methods have been reported like spin coating [33], airbrush spray coating [34], hot pressing [35], and CVD [36]. Figure 4 shows a general block diagram of the AACVD and Airbrush processes used in this thesis.

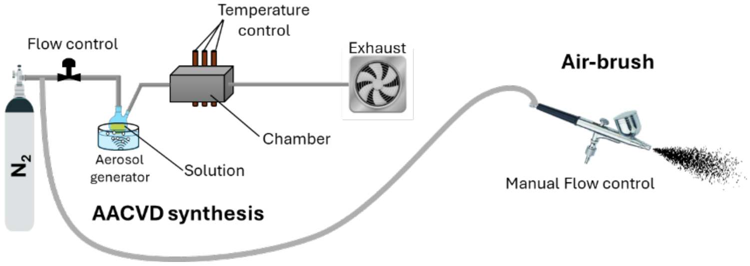

Figure 4: Block diagram of AACVD and Airbrush processes to synthesize chemoresistor sensors.

1.2.3. Substrates

The object that provides the surface where all pieces are integrated as one device is a substrate. Usually, rigid substrates are mainly used, e.g. silicon, glass, and indium tin oxide (ITO)-coated glass. However, in wearable applications, the substrate should be lightweight, small, and easy to integrate with clothes and accessories. Tattoo papers [37], textile-based platforms [38], masks and gloves [39,40], and commercially available polymers [41] have been utilized as a substrate for wearable gas sensors. Among polymer substrates, flexible polyimide (PI) [42], polyethylene terephthalate (PET) [43], and silk [44] have been widely used for gas sensing applications due to their advantages. For example, PI has been used as a flexible substrate due to its bendability properties. Also, it is thermally and chemically stable and can be used in conventional microelectronics fabrication processes. In this thesis, a specific type of PI, Kapton, was used. The main features can be found on the main website of the manufacturer [45].

1.3. Smart electronics for gas sensing applications

The next-generation electronic interfacing with chemoresistor gas sensors should be able to integrate acquiring data, processing data, and wireless communication functionalities. They should also have low-cost and low-power consumption characteristics enabling them to operate with low-capacity batteries or even powered by an alternative energy harvesting element. Integrating IoT and ANNs plays a crucial role in meeting measurement systems' modern demands for precision, efficiency, and regulation compliance.

1.3.1. IoT applied to gas sensing applications

The IoT consists of interconnected devices by wireless technology spread out worldwide. Many low-power wireless communication technologies and protocols such as ZigBee, Bluetooth Low Energy (BLE), LoRa, SigFox, Z-Wave, WiFi, and Near Field Communication (NFC) can be used to connect the smart gas sensors for further data processing and future IoT applications. Some of them have been reported as part of gas-sensing devices. Chen et al. demonstrated a Bluetooth wearable NO_2 sensor based on zinc sulfide nanoparticles/nitrogen-doped reduced graphene oxide [46]. Zhang et al. reported a flexible NFC based on an NH_3 sensor of reduced graphene oxide decorated with Ag-NPs, which sense low concentrations at room temperature [47]. González et al. developed a LoRa network for detecting gas leakage events and air quality monitoring based on a graphene sensor [48]. Song et al. presented a wireless self-powered high-performance integrated nanostructured gas-sensor network for future smart homes using Bluetooth [49]. Nath et al. did a performance analysis of a gas-sensing device and corresponding IoT framework in mines connected through Wi-Fi technology [50]. Seok et al. presented a low-power wireless multichannel gas sensing system using a capacitive micromachined ultrasonic transducer array through BLE [51].

1.3.2. ANNs applied to gas sensing applications

ANNs are widely applied in gas sensing applications to enhance the reliability of gas detection systems. ANNs can detect patterns in the data from gas sensors to increase the discrimination process of specific target analytes, quantify the concentration values, and compensate for environmental interferences like temperature and humidity [52–54]. ANNs have also been used to detect a mixture of gases. Chu et al. identify a mixture of NO_2 and CO in a wide range of concentrations using a sensor array and PCA, BPNN, and CNN. They also evaluate the effect of % RH and compensate for it [55]. Kim et al. used PCA and ANNs to recognize a mixture of CO and NH_3 under the presence of NO_2 and recognize NO_2 in the presence of CO and NH_3 [56]. Similarly, Zhang et al. used LDA, PCA, and BP-ANN methods to classify CO and CH_4 and their mixture. Also, the authors repeated the experiment by adding interfering species such as H_2 and formaldehyde [57].

1.4. Wearable devices for gas sensing applications

Wearable devices for gas sensing applications are changing personal and environmental safety by providing real-time air quality data. These devices can be adapted to protect vulnerable populations, such as workers in industrial settings, firefighters, or individuals in polluted urban areas. Plenty of research has been done developing wearable devices for gas sensing to be applied to different scenarios. For instance, in environmental monitoring, Cho et al. integrated an optically reduced graphene oxide sensor on a flexible printed circuit board with wireless Bluetooth communication, demonstrating outstanding sensing properties [58]. In health monitoring applications, La Li et al. presented a flexible planar concentric circular micro-supercapacitor array for wearable gas sensing applications, obtaining good selectivity towards ethanol at room temperature [59]. Also in the food industry, Tang et al. developed a flexible nanowire-based chemoresistor NH_3 sensor for smartphone-enabled detection of food freshness in real-time. The authors used a flexible PET substrate and soft lithography technique. The researchers integrated the flexible nanowire sensor onto an FPCB with a Bluetooth module to fabricate a wristband-type portable electronic system.

1.5. Outline of the thesis structure

Combining all the features mentioned above is very complex. Integrating the mentioned elements in a small electronic device puts together different fields of knowledge such as material science, electronics, programming, and data analysis. During this research, the author acquired the know-how about combining low-dimensional materials for gas sensing with electronic devices to collect environmental data such as pollution and air quality. Chemoresisor sensors were fabricated, electronics to interface with chemoresistor sensors were designed, and IoT and ANNs principles were applied. Finally, the thesis reaches the knowledge base of designing and developing wearable devices on low-cost flexible support to monitor humans' exposure to target gases.

The first challenge for developing this thesis was obtaining comprehensive learning about the gas sensing mechanisms of chemoresistor gas sensors and their fabrication methods. As described in Chapter 2, aerosol-assisted chemical vapor deposition (AACVD) was the first fabrication method learned during this research. It was employed to synthesize WO_3-based sensors. Tungsten oxide nanowires were loaded with two levels of concentrations of osmium oxide. The resultant sensors were coupled as an array and their data were analyzed using a multivariate approach to discriminate and quantify gases such as NO_2, EtOH, and H_2. As a result, combining a 3-element sensor array, made of cross-responsive sensors, with methods such as Principal Component Analysis and Multilayer Perceptron enhanced the discrimination and quantification ability of the system. The application of these mathematical methods served to gain knowledge related to ANNs applied to gas-sensing applications.

Chapter 3 presents the integration of chemoresistor sensors with a hardware and software design, including data analysis. The hardware and software bridge the chemical reaction (between the sensitive layer of the sensors with the target analyte), to a final visual user interface. Implementing statistical methods on the software (user interface) enhances the system’s output. Also, incorporating related algorithms in the code improves the accuracy and metrics of the discrimination and quantification process for the final system. As a result, a platform was obtained in level four of the technology readiness level (TRL-4). This platform consists of several nodes connected to a centralized server using the Message Queuing Telemetry Transport (MQTT) protocol. For testing the platform, two pollutants gases, NO_2 and NH_3, were measured in a single form (under % RH variation) and under their mixture. While doing so, a methodology was established to adapt the platform deployment to different scenarios, add new chemoresistor gas sensors in the nodes, and configure new nodes to the platform.

The integration process described in Chapter 3: sensors plus electronics plus ANNs; creates a system composed of the so-called e-Noses. However, building a wearable device on flexible support requires extra features to be aware of such as the sensitive layer of the sensor must operate at room temperature. This is translated into a substantial reduction in the device's power consumption; meaning small batteries could power source the device. There is also a relationship between weight and battery capacity, consequently, the device's working life and lightness. Besides, the electronic design must be as small as possible and integrated with some low-power wireless communication technology. To show insights into this topic, Chapter 4 presents the fabrication of graphene-based sensors incorporating interdigitated electrodes (IDEs) in the same flexible printed circuit board as the electronics. Graphene-based material facilitates the required working temperature for wearable devices. Plus, selecting the airbrush deposition technique helps the manufacturing process without interfering with the electronic design. In this chapter, a cumulative near-field communication (NFC) wearable for NO_2 sensing applications is fabricated. The obtained wearable device can be easily attached to a working vest allowing simple integration in any working environment.

During the mentioned Chapters, the sensors' sensitive layers were fully fabricated and characterized. The structural properties, morphological characteristics, and chemical compositions were checked using techniques such as Field Emission Scanning Electron Microscopy (FESEM), Energy-Dispersive X-ray (EDX), X-ray Diffraction (XRD), Raman spectroscopy, High-Resolution Transmission Electron Microscopy (HR-TEM), and Time-of-Flight Secondary Ion Mass Spectrometry (ToF-SIMS). The sensors' responses through oxidizing and reducing gases were proven using a calibrated measurement system available in the facilities of the Universitat Rovira i Virgili, Microsystems Nanotechnologies for Chemical Analysis (MINOS) group, Department d'Enginyeria Electronica. Details can be found in the corresponding chapter. Furthermore, a complete step-by-step guide is presented for the hardware and software designs, and details are given for the training models process to discriminate and quantify different analytes.

Finally, in Chapter 5, some highlights are commented on the next steps that should be taken to continue this study. Research should be directed at implementing Machine Learning algorithms inside low-cost and low-power microcontrollers with wireless communication combined with materials that work at room temperature. Furthermore, integrating wearable devices on flexible support using energy harvesters from temperature or movement could be an interesting path to continue this study. These wearable devices should have an available low-power wireless technology and be integrated into the IoT.

References

1 IHME, Global Burden of Disease (2024) – with minor processing by Our World in Data, https://ourworldindata.org/air-pollution, (accessed 7 November 2024).

2 World Health Statistics, https://www.who.int/data/gho/publications/world-health-statistics, (accessed 7 November 2024).

3 Información sobre sustancias químicas ECHA, https://echa.europa.eu/es/information-on-chemicals, (accessed 7 November 2024).

4 Community Emissions Data System (CEDS) 2024. – processed by Our World in Data, https://ourworldindata.org/air-pollution, (accessed 7 November 2024).

5 Climate change creates a ‘cocktail’ of serious health hazards for 70 per cent of the world’s workers | International Labour Organization, https://www.ilo.org/resource/news/climate-change-creates-cocktail-serious-health-hazards-70-cent-worlds, (accessed 8 November 2024).

6 J. Chou, *Hazardous gas monitors: a practical guide to selection, operation and applications*, McGraw-Hill, New York, NY, 2000.

7 P. Gründler, *Chemical Sensors: An Introduction for Scientists and Engineers*, 2007, 1–273.

8 G. Korotcenkov, *Materials Science and Engineering: B*, 2007, **139**, 1–23.

9 J. Zhang, X. Liu, G. Neri and N. Pinna, *Advanced Materials*, 2016, **28**, 795–831.

10 F. J. Ibañez and F. P. Zamborini, *Small*, 2012, **8**, 174–202.

11 Y. Zhao, J. G. Song, G. H. Ryu, K. Y. Ko, W. J. Woo, Y. Kim, D. Kim, J. H. Lim, S. Lee, Z. Lee, J. Park and H. Kim, *Nanoscale*, 2018, **10**, 9338–9345.

12 M. K. Smith and K. A. Mirica, *J Am Chem Soc*, 2017, **139**, 16759–16767.

13 Y. Huang, W. Jiao, Z. Chu, S. Wang, L. Chen, X. Nie, R. Wang and X. He, *ACS Appl Mater Interfaces*, 2020, **12**, 997–1004.

14 È. Navarrete, C. Bittencourt, X. Noirfalise, P. Umek, E. González, F. Güell and E. Llobet, *Sens Actuators B Chem*, 2019, **298**, 126868.

15 M. Asad, M. H. Sheikhi, M. Pourfath and M. Moradi, *Sens Actuators B Chem*, 2015, **210**, 1–8.

16 M. L. Grilli, *Metals (Basel)*, 2020, **10**, 820.

17 X. Gao, X. Su, C. Yang, F. Xiao, J. Wang, X. Cao, S. Wang and L. Zhang, *Sens Actuators B Chem*, 2013, **181**, 537–543.

18 H. Zheng, J. Z. Ou, M. S. Strano, R. B. Kaner, A. Mitchell and K. Kalantar-zadeh, *Adv Funct Mater*, 2011, **21**, 2175–2196.

19 S. Vallejos, P. Umek, T. Stoycheva, F. Annanouch, E. Llobet, X. Correig, P. De Marco, C. Bittencourt and C. Blackman, *Adv Funct Mater*, 2013, **23**, 1313–1322.

20 E. Rossinyol, J. Arbiol, F. Peiró, A. Cornet, J. R. Morante, B. Tian, T. Bo and D. Zhao, *Sens Actuators B Chem*, 2005, **109**, 57–63.

21 B. Tian, X. Liu, L. A. Solovyov, Z. Liu, H. Yang, Z. Zhang, S. Xie, F. Zhang, B. Tu, C. Yu, O. Terasaki and D. Zhao, *J Am Chem Soc*, 2004, **126**, 865–875.

22 A. Rumplecker, F. Kleitz, E.-L. Salabas and F. Schüth, *Chemistry of Materials*, 2007, **19**, 485–496.

23 M. Hafeez, A. Siddique Saleemi, S. Ur Rehman, M. Adrees, S. Mehmood, I. A. Mir and L. Zhu, *Appl Surf Sci*, 2021, **536**, 147713.

24 W. B. Carter, G. W. Book, T. A. Polley, D. W. Stollberg and J. M. Hampikian, *Thin Solid Films*, 1999, **347**, 25–30.

25 G. Carta, N. El Habra, L. Crociani, G. Rossetto, P. Zanella, A. Zanella, G. Paolucci, D. Barreca and E. Tondello, *Chemical Vapor Deposition*, 2007, **13**, 185–189.

26 D. Barreca, G. Carraro, E. Fois, A. Gasparotto, F. Gri, R. Seraglia, M. Wilken, A. Venzo, A. Devi, G. Tabacchi and C. Maccato, *The Journal of Physical Chemistry C*, 2018, **122**, 1367–1375.

27 S. Blittersdorf, N. Bahlawane, K. Kohse-Höinghaus, B. Atakan and J. Müller, *Chemical Vapor Deposition*, 2003, **9**, 194–198.

28 M. Lugo-Ruelas, P. Amézaga-Madrid, O. Esquivel-Pereyra, W. Antúnez-Flores, P. Pizá-Ruiz, C. Ornelas-Gutiérrez and M. Miki-Yoshida, *J Alloys Compd*, 2015, **643**, S46–S50.

29 M. Asad, M. H. Sheikhi, M. Pourfath and M. Moradi, *Sens Actuators B Chem*, 2015, **210**, 1–8.

30 B. Cho, J. Yoon, S. K. Lim, A. R. Kim, D. H. Kim, S. G. Park, J. D. Kwon, Y. J. Lee, K. H. Lee, B. H. Lee, H. C. Ko and M. G. Hahm, *ACS Appl Mater Interfaces*, 2015, **7**, 16775–16780.

31 A. Hanif, A. Bag, A. Zabeeb, D. Bin Moon, S. Kumar, S. Shrivastava and N. E. Lee, *Adv Funct Mater*, 2020, **30**, 2003540.

32 S. Z. N. Demon, A. I. Kamisan, N. Abdullah, S. A. M. Noor, O. K. Khim, N. A. M. Kasim, M. Z. A. Yahya, N. A. A. Manaf, A. F. M. Azmi and N. A. Halim, *Sensors and Materials*, 2020, **32**, 759.

33 J. K. Wassei and R. B. Kaner, *Materials Today*, 2010, **13**, 52–59.

34 S. Gilje, S. Han, M. Wang, K. L. Wang and R. B. Kaner, *Nano Lett*, 2007, **7**, 3394–3398.

35 T. L. Chen, D. S. Ghosh, V. Mkhitaryan and V. Pruneri, *ACS Appl Mater Interfaces*, 2013, **5**, 11756–11761.

36 Y. Zhang, L. Zhang and C. Zhou, *Acc Chem Res*, 2013, **46**, 2329–2339.

37 R. K. Mishra, A. Barfidokht, A. Karajic, J. R. Sempionatto, J. Wang and J. Wang, *Sens Actuators B Chem*, 2018, **273**, 966–972.

38 B. U. Hwang, J. H. Lee, T. Q. Trung, E. Roh, D. Il Kim, S. W. Kim and N. E. Lee, *ACS Nano*, 2015, **9**, 8801–8810.

39 F. Güder, A. Ainla, J. Redston, B. Mosadegh, A. Glavan, T. J. Martin and G. M. Whitesides, *Angewandte Chemie International Edition*, 2016, **55**, 5727–5732.

40 R. K. Mishra, L. J. Hubble, A. Martín, R. Kumar, A. Barfidokht, J. Kim, M. M. Musameh, I. L. Kyratzis and J. Wang, *ACS Sens*, 2017, **2**, 553–561.

41 S. Guo, D. Yang, S. Zhang, Q. Dong, B. Li, N. Tran, Z. Li, Y. Xiong and M. E. Zaghloul, *Adv Funct Mater*, 2019, **29**, 1900138.

42 Y. S. Kim, *Sens Actuators B Chem*, 2006, **114**, 410–417.

43 J. Ma, H. Fan, Z. Li, Y. Jia, A. K. Yadav, G. Dong, W. Wang, W. Dong and S. Wang, *Sens Actuators B Chem*, 2021, **334**, 129677.

44 W. T. Jung, J. W. Jeon, H. S. Jang, D. Y. Kim, H. K. Lee and B. H. Kim, *Sens Actuators B Chem*, 2020, **307**, 127596.

45 Home | DuPont, https://www.dupont.com/, (accessed 23 November 2024).

46 X. Chen, T. Wang, Y. Han, W. Lv, B. Li, C. Su, M. Zeng, J. Yang, N. Hu, Y. Su and Z. Yang, *Sens Actuators B Chem*, 2021, **345**, 130423.

47 L. Zhang, Q. Tan, H. Kou, D. Wu, W. Zhang and J. Xiong, *Sci Rep*, 2019, **9**, 9942.

48 E. González, J. Casanova-Chafer, A. Romero, X. Vilanova, J. Mitrovics and E. Llobet, *Sensors*, 2020, **20**, 6225.

49 Z. Song, W. Ye, Z. Chen, Z. Chen, M. Li, W. Tang, C. Wang, Z. Wan, S. Poddar, X. Wen, X. Pan, Y. Lin, Q. Zhou and Z. Fan, *ACS Nano*, 2021, **15**, 7659–7667.

50 S. Nath, A. Dey, P. Pachal, J. K. Sing and S. K. Sarkar, *Microsystem Technologies*, 2021, **27**, 3977–3985.

51 C. Seok, M. M. Mahmud, M. Kumar, O. J. Adelegan, F. Y. Yamaner and O. Oralkan, *IEEE Internet Things J*, 2019, **6**, 831–843.

52 Z. Ye, Y. Liu and Q. Li, *Sensors*, 2021, **21**, 7620.

53 N. Ha, K. Xu, G. Ren, A. Mitchell and J. Z. Ou, *Advanced Intelligent Systems*, 2020, **2**, 2000063.

54 H. Chen, D. Huo and J. Zhang, *IEEE Trans Biomed Circuits Syst*, 2022, **16**, 169–184.

55 J. Chu, W. Li, X. Yang, Y. Wu, D. Wang, A. Yang, H. Yuan, X. Wang, Y. Li and M. Rong, *Sens Actuators B Chem*, 2021, **329**, 129090.

56 J.-Y. Kim, S. P. Bharath, A. Mirzaei, S. S. Kim and H. W. Kim, *Sens Actuators B Chem*, 2023, **386**, 133767.

57 J. Zhang, Y. Xue, Q. Sun, T. Zhang, Y. Chen, W. Yu, Y. Xiong, X. Wei, G. Yu, H. Wan and P. Wang, *Sens Actuators B Chem*, 2021, **326**, 128822.

58 S. J. Choi, S. J. Kim and I. D. Kim, *NPG Asia Materials 2016 8:9*, 2016, **8**, e315–e315.

59 L. Li, C. Fu, Z. Lou, S. Chen, W. Han, K. Jiang, D. Chen and G. Shen, *Nano Energy*, 2017, **41**, 261–268.

60 Z. Song, W. Ye, Z. Chen, Z. Chen, M. Li, W. Tang, C. Wang, Z. Wan, S. Poddar, X. Wen, X. Pan, Y. Lin, Q. Zhou and Z. Fan, *ACS Nano*, 2021, **15**, 7659–7667.

61 S. Nath, A. Dey, P. Pachal, J. K. Sing and S. K. Sarkar, *Microsystem Technologies*, 2021, **27**, 3977–3985.

62 W. Dargie, J. Wen, L. A. Panes-Ruiz, L. Riemenschneider, B. Ibarlucea and G. Cuniberti, *IEEE Sens J*, 2023, **23**, 12274–12283.

63 J.-H. Suh, I. Cho, K. Kang, S.-J. Kweon, M. Lee, H.-J. Yoo and I. Park, *Sens Actuators B Chem*, 2018, **265**, 660–667.

64 C. Seok, M. M. Mahmud, M. Kumar, O. J. Adelegan, F. Y. Yamaner and O. Oralkan, *IEEE Internet Things J*, 2019, **6**, 831–843.

Chapter 2

Comprehensive learning on gas sensors: fabrication (AACVD) and data analysis

The following chapter gives insights into gaining comprehensive learning about gas sensors' fabrication techniques, sensitive layer material characterization, and gas sensing properties of chemoresistor gas sensors. Also, it introduces knowledge about ANNs applied to gas sensing applications.

These explanations are presented in Section 2.1, through a published paper named "AACVD synthesized tungsten oxide-NWs loaded with osmium oxide as a gas sensor array: enhancing detection with PCA and ANNs".

Development of wearable electronic devices, on low-cost flexible support for gas sensing Applications
Alejandro Santos Betancourt

Section 2.1

AACVD synthesized tungsten oxide-NWs loaded with osmium oxide as a gas sensor array: enhancing detection with PCA and ANNs

Alejandro Santos-Betancourt, Eric Navarrete, Damien Cossement, Carla Bittencourt, and Eduard Llobet

RSC Advances, Issue 47, 2024, 14, 34985-34995, November 1st, 2024

DOI: https://doi.org/10.1039/D4RA05346J

Abstract

This paper presents the fabrication of sensors based on tungsten trioxide nanowires decorated with osmium oxide nanoparticles using the aerosol-assisted chemical vapor deposition (AACVD) technique. This methodology allows the obtention of different osmium oxide decoration loadings on the tungsten oxide nanowires. The morphological and chemical characteristics; and the structural properties of the sensing layers of the sensors were studied using different techniques such as FESEM, HR-TEM, and ToF-SIMS. The gas sensing properties were analyzed for pure tungsten trioxide sensors and tungsten trioxide loaded with osmium exposed to nitrogen dioxide, hydrogen, and ethanol, thus assessing the impact of the loading on the sensor response. A sensor array comprising pure and osmium-loaded tungsten oxide devices coupled to multivariate pattern recognition techniques is shown to perform well in gas identification and quantification tasks, offering promising implications in the field of gas sensing technology.

Keywords

AACVD, tungsten trioxide, osmium, PCA, ANNs, nitrogen dioxide, ethanol, hydrogen.

1. Introduction

Global concern about air quality and the emission of toxic gases is increasing [1]. In that sense, significant progress has been made in developing sensors capable of detecting specific gases in different scenarios. Semiconductor metal oxides (MOXs) have emerged as a group of promising materials, favored for their small size, low manufacturing cost, and simple read-out-chain design [2,3]. Different material synthesis techniques can be envisaged for building a MOXs-based sensor, such as liquid-phase (LPS) and vapor-phase synthesis (VPS). One example of LPS is the sol–gel method, in which porous and thin sensing layers can be obtained [4]. Another example of this technique is hydrothermal growth [5,6]. This method enables obtaining different morphologies for the sensing layer, like nanoplates, nanowires, and nanorods [7,8]. On the other hand, VPS has approaches focused on chemical and physical methods. VPS is used to obtain nanomaterials (*e.g.*, nanoparticles, nanorods, *etc.*), and the thickness of the sensing layer can be controlled by optimizing the deposition temperature, the gas flow, the solvents, and the precursors [9]. One of the most used methods of VPS is aerosol-assisted chemical vapor deposition (AACVD) [10]. This method combines the advantages of fine particle production in aerosol processes with the film-forming capabilities of CVD [11], allowing the deposition of oxide structures like WO_3 [12], In_2O_3 [13], Co_3O_4 [14], Cr_2O_3 [15], CeO_2 [16], MgO [17], MnO_2 [18], Al_2O_3 [19], CuO [20], and Fe_2O_3 [21]. When properly optimized, the AACVD enables also the loading of the aforementioned metal oxides with metal/metal oxide nanoparticles, thus showing good potential for the mass-production of functional nanomaterials. Since all these materials have specific characteristics and react to different chemical analytes, they are widely used as sensitive layers in sensors across numerous industries like automotive or petrochemical. Although MOXs are useful and effective for a long period, they have drawbacks such as lack of selectivity to specific gases, baseline drift, high sensitivity to humidity, and high operating temperatures [22,23]. In that sense, many metal oxides have been modified by doping or loading with other materials to address issues associated with their disadvantages [24–28].

Doping metal oxides with metal ions (*e.g.*, Ti^{3+}, Sm^{3+}, La^{3+}, Ce^{3+}, Pr^{3+}, Cr^{3+}) has been exploited as a way to tune band-gap, charge carrier concentration, carrier mobility and defects, resulting in increased responsiveness to gases [29–32]. Metal oxides loaded with metal catalyst nanoparticles have been widely used to increase the sensitivity and adjust the selectivity of gas sensors. These nanoparticles contribute to chemical sensitization by enhancing the amount of reactive oxygen species adsorbed [33–35] on the semiconductor metal oxide surface and/or by helping break down target molecules by catalytic effects, thereby enhancing their reaction with oxygen through spillover effects [36]. Additionally, recent advancements have led to the creation of single-crystalline, nanostructured metal oxides, such as nanorods and nanowires [11,26,27,37]. Metal nanoparticles (NPs) may also have an electronic sensitization effect *via* developing heterojunctions at the metal oxide/NP interface [38–40]. In particular, combining n-type metal oxide nanowires decorated with p-type metal oxide NPs results in multiple n-p heterojunctions, causing significant electronic sensitization effects [41]. As n–p heterojunctions form, electrons move from the n-type metal oxide to the p-type nanoparticles, creating depletion zones. The adsorption of gases onto these nanoparticles triggers further electronic charge transfers to the n-type metal oxide base, altering the depletion zone width and significantly changing the film's overall electrical conductance, thus giving readable data linked to the target gas. In the literature, the most used p-type nanoparticles are the ones based on noble metals due to their excellent chemical properties, stability, and performance. While the most employed metal NPs are Pt, Pd, and Au, in the last few years we have studied the use of other transition metal NPs such as Ir [26], Co [27], or Ni [28]. Supported on tungsten oxide nanowires. In addition, the literature shows only few papers in which MOXs have been loaded with osmium. Capone *et al.* [42] developed a sensor consisting of SnO_2 decorated with osmium using the sol–gel technique to detect methane at a low working temperature. Quaranta *et al.* [43] used an array of sensors including a pristine SnO_2 sensor and decorated ones with palladium, platinum, and osmium. They analyzed the data using a multivariate approach and used principal component analysis (PCA) to discriminate gaseous species such as carbon monoxide, methane, ethanol, methanol, and nitrogen dioxide. Considering the scarce number of results available on osmium loaded MOX gas sensors, the study of osmium supported on WO_3 seems novel and worthwhile.

It is known from the literature that using gas sensor arrays and chemometrics is a way to enhance the discrimination and quantification ability of individual MOX sensors [44,45]. In this approach, sensors with overlapping selectivity are coupled to multivariate data analysis techniques that process sensor response vectors [46–48]. In particular, the principal component analysis (PCA), a technique that enables building models that maximize the data variance explained (*i.e.*, sensor response variance), has been widely employed as an unsupervised dimensionality reduction and classification technique in gas sensor arrays. Besides enabling data separation and classification, PCA allows for studying how individual sensors contribute to gas discrimination and helps identifying redundant or irrelevant sensors [47,49]. Additionally, artificial neural networks (ANNs) such as the feed-forward multi-layer perceptron (FF-MLP) have been widely employed in quantitative analysis (*e.g.*, to predict gas concentrations). The MLP is a supervised method that learns the intricate patterns and relationships existing between the sensor array responses [50,51]. In this paper, pristine tungsten trioxide (WO_3) and WO_3-based sensors loaded with two levels of osmium oxide concentrations are synthesized for the first time using the AACVD technique. The synthesized sensors were employed in a sensor array to discriminate and quantify chemical species such nitrogen dioxide, ethanol, and hydrogen. The output data from the sensor array was processed through PCA and the multilayer perceptron (MLP) ANNs of studying the discrimination and quantification ability of the sensor system.

2. Experimental

2.1. Description of the fabrication process

Tungsten trioxide (WO_3) nanowires (NWs) and tungsten trioxide loaded with osmium oxide (WO_3/OsO_4) were synthesized through the AACVD at 375 °C. The nanomaterials were grown on top of commercially available alumina substrates, from CeramTech GmbH, that present screen-printed 300 μm gap interdigitated platinum electrodes on the top side and an 8 Ω heating platinum resistor on the bottom side. The AACVD process was performed in two steps. First, the synthesis of pristine WO_3 NWs and then, the loading of the WO_3 NWs with osmium at different concentration levels. To grow the pure WO_3 NWs, as indicated in Fig. 1, 40 mg of tungsten hexacarbonyl $W(CO)_6$, (Sigma Aldrich, St. Louis, MO, USA, CAS: 14040-11-0) as an organometallic precursor was weighted. Subsequently, the precursor was solubilized in a mixture of methanol (Scharlab, Sentmenat, Spain, CAS: 67-56-1) and acetone (Sigma Aldrich, St. Louis, MO, USA, CAS: 67-64-1) with a 1:3 volume ratio (5 mL and 15 mL, respectively). The solution was sonicated using an ultrasonic cleaning machine, SKE-3S (Tangshan UMG Medical Instrument Co., Ltd, Tangshan, Hebei, China) until all the precursor material was fully dissolved (around 15 minutes) and then, placed in an aerosol generator bath (Miniland Humiplus Advanced, Ultrasonic, PO: POD-MNL 15-02435), which generates 1 MHz ultrasonic waves to convert the solution into a micro-droplet aerosol. This aerosol is carried via a pipe system using nitrogen as an inert carrier gas at a constant flow of 1 L min^{-1} towards a preheated CVD hot-wall reactor at 375 °C where the alumina substrates were previously introduced. The resulting WO_3 NWs layer fully coats the electrodes and, as typically, some amorphous carbon remnants are left by the organic precursor and solvents. To remove such impurities and enhance the oxidation stoichiometry, an annealing process is performed right after the deposition, which is conducted in a Carbolite CWF 1200 muffle (Carbolite Gero Ltd, Neuhausen, Germany) at 500 °C for 2 h, with a temperature ramp of 5 °C min^{-1}, under pure dry air. Fig. 1 describes a schematic of the process.

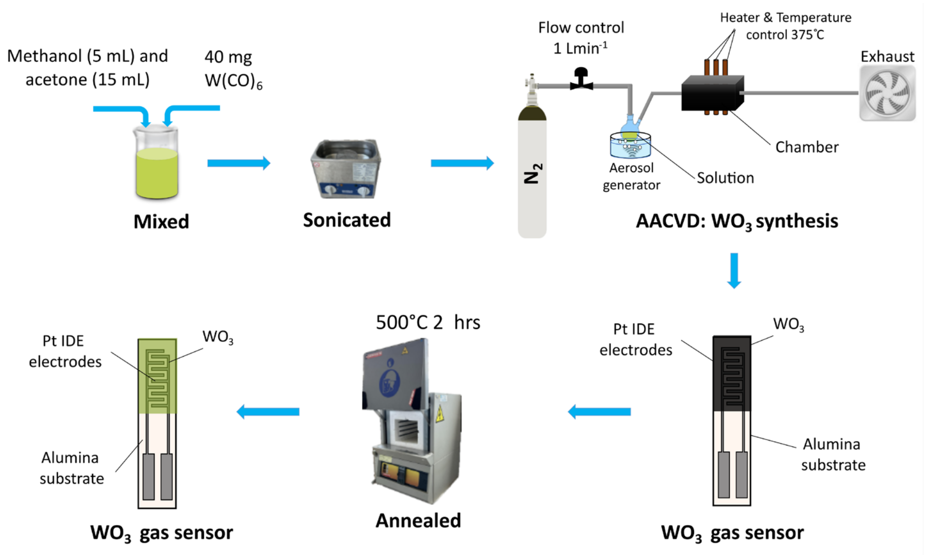

Fig. 1 Block diagram AACVD synthesis of WO_3 sensors.

Afterward, a second AACVD process was conducted to achieve two different levels of osmium loading (low and high concentrations). In this second step, two amounts of osmium were weighted using a KERN (KERN & SOHN GmbH, Germany) 0.0001 g precision balance: 2.5 and 10 mg of osmium(iii) chloride hydrate ($OsCl_3 \times H_2O$) (Sigma Aldrich, St. Louis, MO, USA, CAS: 13444-93-4), subsequently, two methanol 10 mL solutions were prepared. The AACVD process was repeated, as described before, in this case, the previously annealed substrates were placed again inside the CVD reactor and preheated at 350 °C respectively in two separate runs. The processes result in two WO_3/OsO_4 samples at different loading levels: WO_3/OsO_4/2.5 mg and WO_3/OsO_4/10 mg. Finally, an annealing process was performed to clean the remnants of carbon from the surface of the films.

2.2. Material characterization

Field Emission Scanning Electron Microscope (FESEM) Scios 2 DualBeam was used to study the surface morphology of the sensitive layers. Sample characterization was performed at a high vacuum, and the electron acceleration voltage was established between 2 and 5 kV. Also, the energy-dispersive X-ray (EDX) incorporated in the FESEM Scios was used to check the chemical composition of the active layers. HR-TEM characterization of the samples was performed on a Jeol 2100 microscope, working at 200 kV. The material was scratched from the alumina substrate and dispersed in methanol. The dispersion was ultrasonicated for 20 minutes and a drop was deposited on a lacy carbon film supported by a nickel grid. Also, using the same equipment, EDX analysis was performed. Likewise, before ToF-SIMS data acquisition, samples were pre-cleaned with a giant argon cluster beam (Ar_{3000}^+) operated at 10 keV over an area of 500 × 500 μm^2, gently removing surface hydrocarbon contamination while keeping the underlying sensor material intact. At the center of the freshly prepared sputter crater, surface ToF-SIMS spectra were acquired in positive mode using a ToF-SIMS M6 instrument from ION-TOF GmbH, Münster, Germany. A Bi^+30 keV primary ion beam was used at a current of ~0.76 pA and was rastered over a scan area of 200 × 200 μm^2, for 1000 seconds, allowing the sensitivity in the detection of Os^+ to be enhanced.

2.3. Description of the measurement system

The gas-sensing properties of the different sensors were studied. The sensors were exposed to different gases both reducing; ethanol vapors (EtOH) and hydrogen (H_2), and an oxidizing gas as nitrogen dioxide (NO_2). The concentrations analyzed for ethanol vapors were 5, 10, 15, and 20 ppm; for hydrogen 250, 500, 750, and 1000 ppm; and the concentrations were set for nitrogen dioxide in 250, 500, 750, and 1000 ppb. To do so, the sensors were placed inside an airtight Teflon® chamber with an inner volume of 21.18 cm³. The chamber has a connector-type edge dual female 12POS 0.100 FMC06DRYH (©2024 Sullins Connector Solutions, San Marcos, CA 92069, USA) which interfaces the sensors with the measurement instrumentation. Different gases were delivered to the chamber through a computer-controlled mass-flow system to ensure the reproducibility of the concentrations and constant flow. The gases were purchased from Linde® as calibrated gas bottles balanced in dry air and the carrier gas was zero-grade dry synthetic air. The analysis of the gases was programmed as pulses: consisting of increasing target gas concentrations in between of dry air supplying to recover the baseline at a constant flow of 100 mL min⁻¹. The sensor resistance was measured and stored employing a Keysight 3972A data acquisition system. An Agilent U8001A Single Output DC Power Supply was used to power the heating element of the substrates to achieve the operating temperatures of 150 °C, 200 °C, and 250 °C. This system is depicted in Fig. 2.

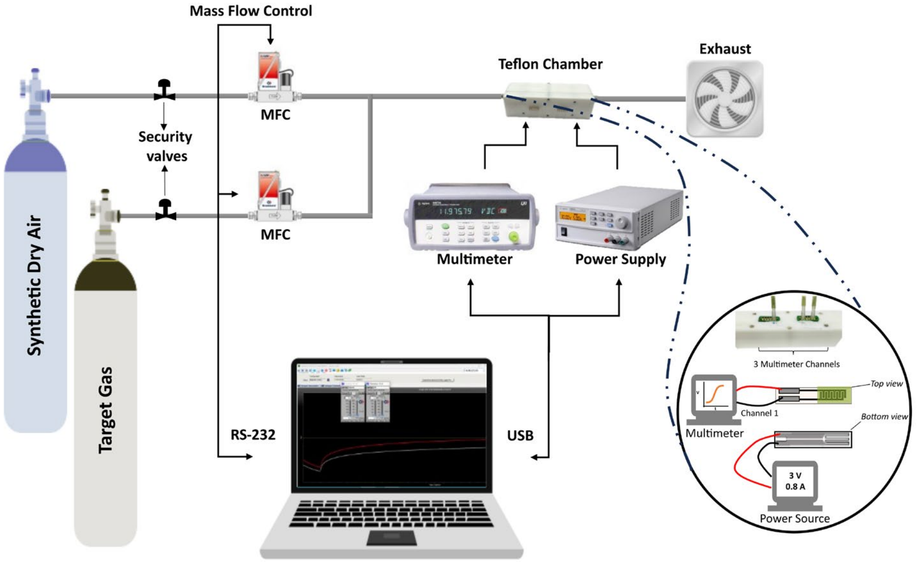

Fig. 2 Schematic representation of the gas measurement system.

2.4. Methodology for data analysis

After measuring the resistance variation of each sensor while reacting with the target gas, specific values were selected from the measurement dataset. The electrical resistance values were taken before and after each pulse of the target gas. Then, the electrical resistance values related to pulses of the same concentration were averaged and PCA was conducted to classify the gases. On the other hand, using the whole dataset of measurements, MLPs were trained, using MATLAB Statistics and Machine Learning Toolbox (academic-available license). Before that, the sensor array raw data was filtered using an asymmetric windowed filter with a left-right length of 12 and 0 samples. Then, the resulting data served as features (input layers) to develop the MLP models. For training the MLPs, 80% of the observations were used, and the remaining 20% were reserved for testing. Training and validation vectors were selected randomly for these purposes. A 5-fold cross-validation scheme was used to avoid overfitting during the training process. The tuning process compared different types of architecture (hidden layers), varying the number of layers (1, 2, 3) and neurons per layer (10, 25, 100). The quantification MLP with best performance was selected based on root mean squared error (RMSE) and coefficient of determination (R^2). Prediction accuracy was the criterion employed for evaluating the performance of MLP classification models. Once the architecture of the MLP was set, the activation function was varied (including None: $f(x) = x$, ReLU: $f(x) = \max(0, x)$, Sigmoid: $f(x) = \frac{1}{1+ e^{-x}}$, and Tanh: $f(x) = \frac{2}{1+ e^{-2x}} - 1$) to determine the best option.

3. Results & Discussion

3.1. Sensing layer characterization

Fig. 3 shows FESEM images for the different sensors fabricated, pure WO3 NWs and WO_3/OsO_4.

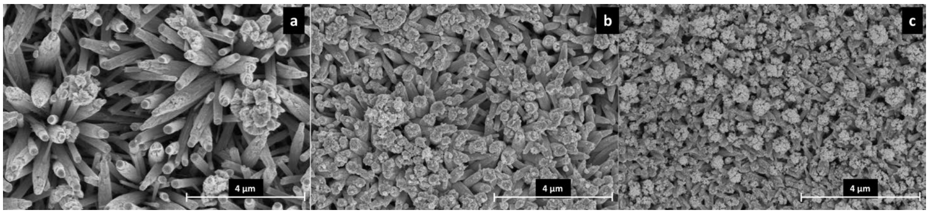

Fig. 3 FESEM at 4 µm of sensors. (a) Pure WO_3 (b) WO_3/OsO_4 (2.5 mg) (c) WO_3/OsO_4 (10 mg).

There is a clear change in the surface morphology as the concentration of osmium increases (see Fig. 3a–c). The pure WO_3 NWs surface shows a smooth surface with well-defined nanowire tips and bodies. As the concentration of osmium increases, the formation of material clusters also increases. The presence of osmium particles could lead to a displacement of material from the already formed layers acting as a seed thus enhancing the nucleation of material around the tips of the nanowires. One major effect of such change in the layer is the increase in the total surface area available for the oxygen species to adsorb and react. Similarly, a sample of the synthesized layer was brought to the HR-TEM to study and determine the crystallinity and composition. Fig. 4 shows a cluster of WO_3/OsO_4/2.5 mg and WO_3/OsO_4/10 mg NWs with an inset depicting that the *d*-spacing between lattice fringes in the inset is 3.78 Å corresponding to (002) planes in WO_3 with monoclinic $P\bar{1}$ structure (ICDD 43e1035), confirming the composition of the tungsten trioxide nanowires. EDX studies were carried out on the sensor samples (*i.e.*, on alumina substrates) and on the samples prepared for TEM analysis (*i.e.*, on TEM grids). These studies (see Fig. S1 and S2 in the ESI†) could not confirm the presence of osmium in loaded samples. The amount of osmium loading achieved remains under the detection limit of the technique.

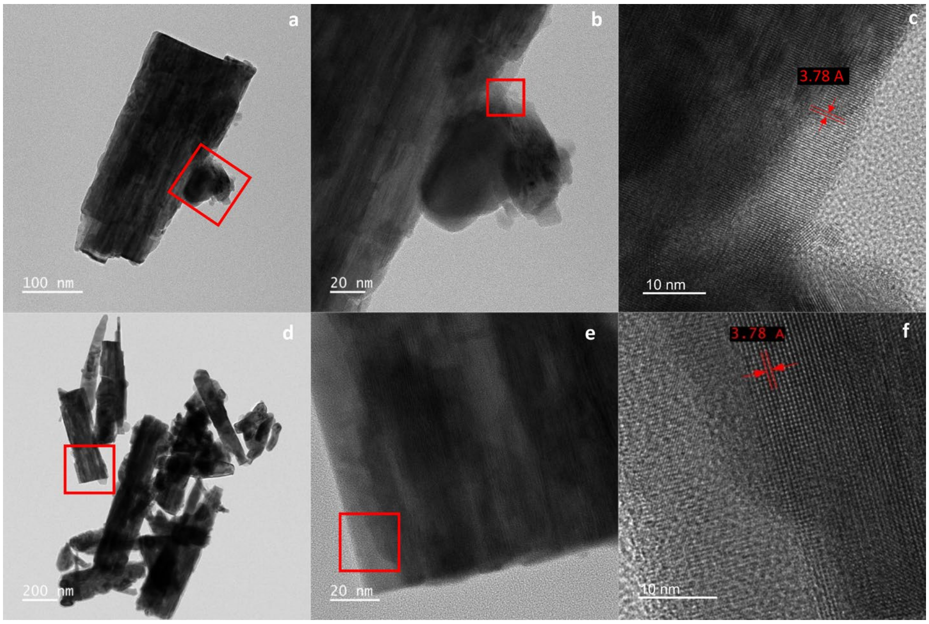

Fig. 4 (a) Broken nanowires, $WO_3/OsO_4/2.5$ mg, from the sonication process during sample preparation. (b) HR-TEM inset from a nanowire body image, $WO_3/OsO_4/2.5$ mg, the caption shows the interplanar structure, probing a high crystallinity. (c) Close up, $WO_3/OsO_4/2.5$ mg, showing the (002) interplanar distance of WO_3 (d) broken nanowires, $WO_3/OsO_4/10$ mg, from the sonication process during sample preparation. (e) HR-TEM inset from a nanowire body image, $WO_3/OsO_4/10$ mg, the caption shows the interplanar structure, probing a high crystallinity. (f) Close up, $WO_3/OsO_4/10$ mg, showing the (002) interplanar distance of WO_3.

On the other hand, Fig. 5 shows the ToF-SIMS analysis on a $WO_3/OsO_4/10$ mg sample. The presence of the Os^+ peak was observed at *m*/*z* 191.96. It is noteworthy to point out that the Os^+ peak region, features a higher background compared to the W^+ peaks, which suggests that osmium occurs with very low abundance. In conclusion, ToF-SIMS has confirmed that osmium is present in loaded samples. Beyond the detection of Os^+ in the ToF-SIMS spectra, simultaneously with the spectra acquisition chemical images were recorded of the surface sample, enabling the location of osmium. ToF-SIMS was used instead of XPS because the former technique is more sensitive than the latter. This aspect is discussed further in the ESI†.

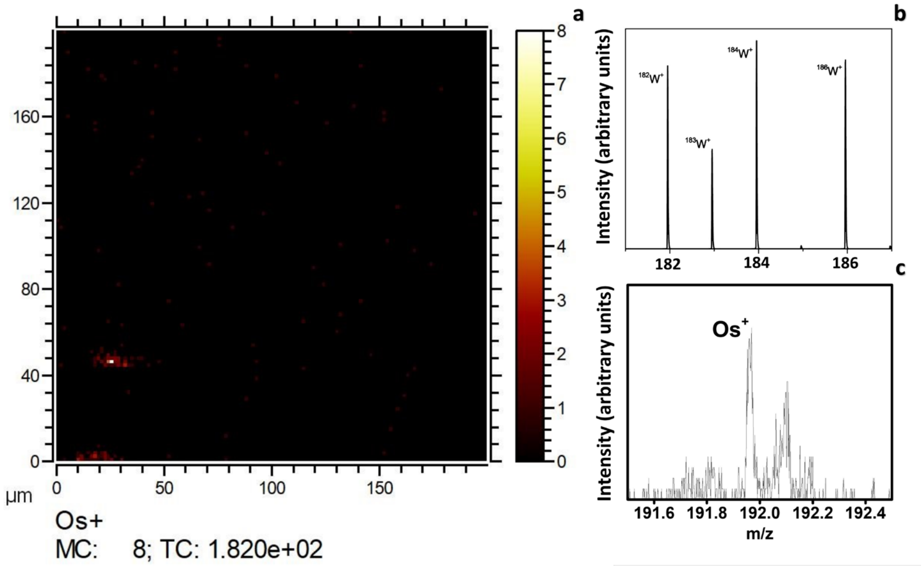

Fig. 5 ToF-SIMS analysis results for a WO_3/OsO_4/10 mg sample. (a) Chemical mapping image of the surface with osmium clusters appearing as red dots/areas, (b) spectrum associated to tungsten detection, and (c) spectrum associated to osmium detection.

3.2. Gas measurement results

The measurements of the electrical resistance of each sensor are shown in Fig. 6–8. Sensors were operated at 250 °C, in which the sensors showed the best response intensity and response dynamics to the target gases. Long-term measurements for the operating temperatures of 150 °C and 200 °C can be found in Fig. S3 and S4 in the ESI †. Fig. 6 to 8, report the responses to three repeated cycles of four increasing pulsed concentrations of the target gases. Each pulse of gas lasted 30 minutes and was followed by 30 minutes of dry air to recover the baseline. For H_2 and EtOH, the resistance of the sensors decreases but in the case of NO_2, the resistance value increases, as expected for an n-type semiconducting nanomaterial.

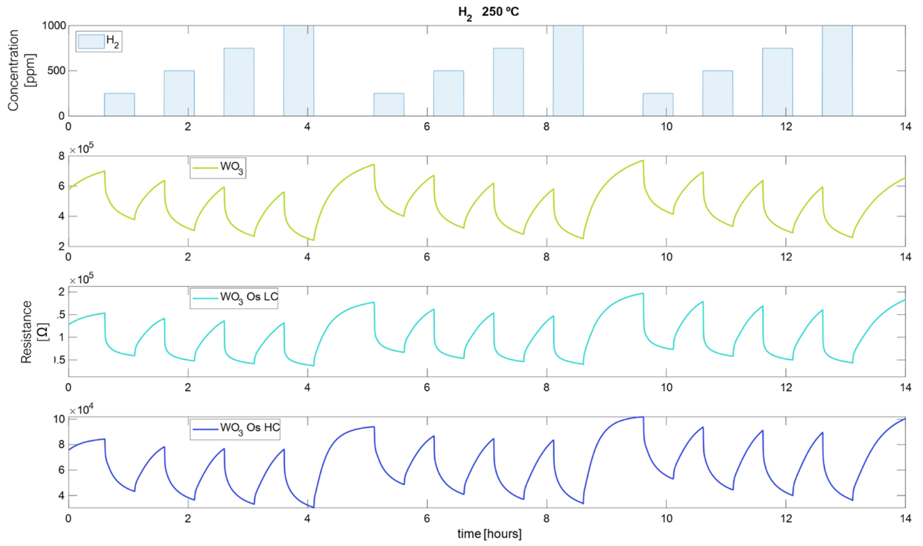

Fig. 6 Measurement of the sensor at an operating temperature of 250 °C throughout H_2 exposures.

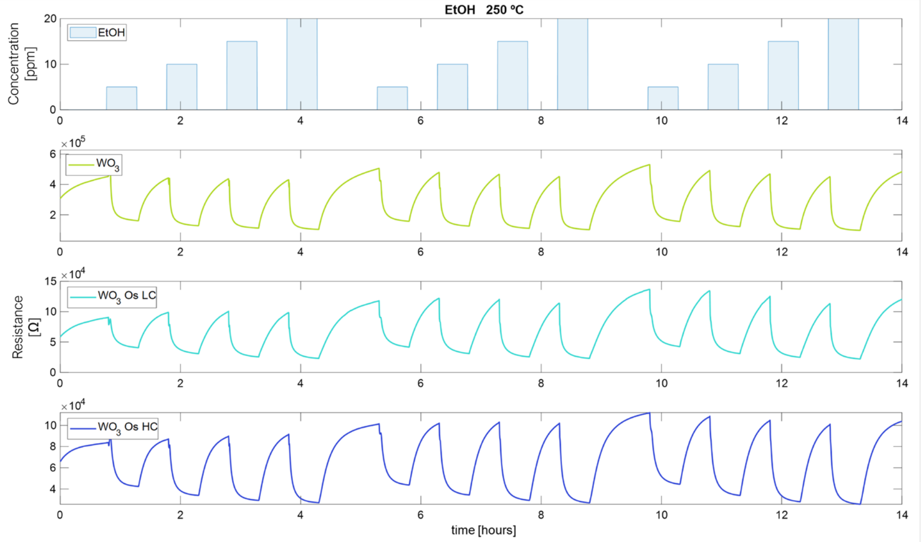

Fig. 7 Measurement of the sensor at an operating temperature of 250 °C throughout EtOH exposures.

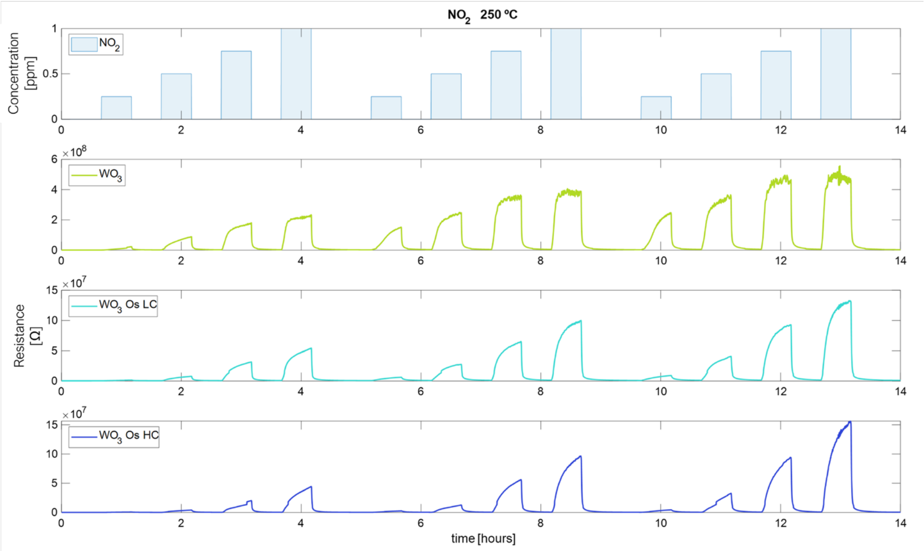

Fig. 8 Measurement of the sensor at an operating temperature of 250 °C throughout NO_2 exposures.

This measurement protocol enabled testing the repeatability of measurements. Fig. S5a–c in the ESI† show the calibration curves for H_2, EtOH, and NO_2 at 250 °C, respectively. Also, they show the mean of the responses of the three repeated cycles in each concentration of the target gases and the error bars corresponding to their variability (or measurement uncertainty). It is noticed that the response increases while the concentration of gases increases. For H_2, Fig. S5a†, the pristine WO_3 sensor increases its measurement uncertainty when increasing the gas concentration from 0.18% to 0.4% (Table S1 in the ESI† shows numerical details). While the sensors loaded with osmium keep this uncertainty almost constant throughout the concentration range studied (WO_3/OsO_4/2.5 mg: from 0.76% to 0.66%, WO_3/OsO_4/10 mg: from 0.4% to 0.37%). It can also be noticed that, for H_2 detection, the two doped sensors show a higher response than the pristine sensor (Fig. S5a†). The response of the sensors towards EtOH is shown in Fig. S5b†. The sensor with the lowest load of osmium behaves similarly to the pristine sensor. The sensor with higher loadings of osmium shows the lowest response. For the three sensors, the measurement uncertainty decreases as the gas concentration increases (WO_3: from 3.1% to 1.2%, WO_3/OsO_4/2.5 mg: from 7.2% to 2.1%, WO_3/OsO_4/10 mg: from 5.6% to 2.1%). When analyzing the response of the sensors towards NO_2, it is worth noticing that the sensor with the higher loading level of osmium shows the highest sensitivity (*i.e.*, slope of the calibration curve). The measurement uncertainty associated to the detection of NO_2 is also higher (Fig. S5c and Table S1 in the ESI†). Considering these results, the tungsten oxide sensors loaded with osmium hold promise for the detection of hydrogen and nitrogen dioxide.

The effect of loading tungsten oxide on the detection mechanism is as follows. As the amount of osmium loading is increased, the nanowires show an increased number of clusters of tungsten oxide along their body, thus becoming more defective. As a result, the number of available sites where oxygen can be adsorbed is enhanced with osmium oxide loading. The defects present on the material surface act as highly active sites compared to the pristine regions of tungsten oxide. These active sites break the uniform atomic lattice of the nanowire smooth body (see Fig. 3), creating areas with unsaturated bonds, unpaired electrons, or localized charge variations. We postulate that the number of such defects increase with the amount of osmium loaded, acting as adsorption sites for oxygen molecules, which subsequently react with the target gas. The defects act as electron donors or acceptors, depending on their, nature helping to reduce the activation energy required for adsorption and subsequent reaction steps. When oxygen adsorbs at these defect sites, it captures electrons. These reactive oxygen species are chemically active and are ready to interact with the target gas molecules, facilitating the chemical reactions that are responsible for the sensing response.

3.3. Data analysis

Given the fact that the different sensors studied show overlapping selectivity, a multivariate analysis was performed in the next sections to assess whether or not the discrimination of the chemical species considered and their quantification could be achieved. A 3-element sensor array, which comprised pristine, low osmium loaded and high osmium loaded tungsten oxide sensors was considered for this analysis.

Fig. 9a–c show the Biplot of a principal component analysis performed using the electrical resistance values of the three sensors. A PCA analysis was performed for every operating temperature tested. Results denote that the different gases can be discriminated, no matter the operating temperature, through a simple visual inspection. This indicates that, even though individual sensors show cross-responsiveness to the different chemical species considered, a simple, linear pattern recognition algorithm such as PCA that processes the responses of the three sensors together, achieves good discrimination performance.

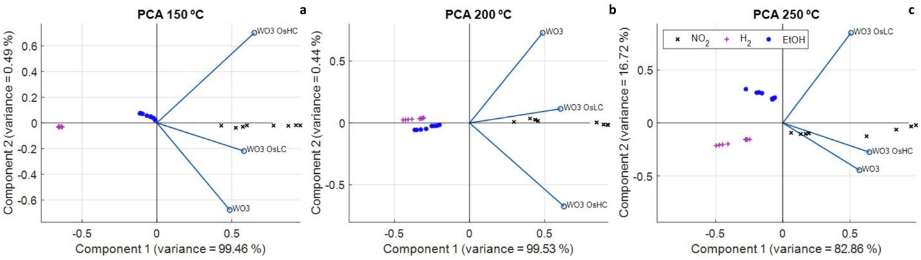

Fig. 9 PCA at (a) 150 °C, (b) 200 °C, and (c) 250 °C.

Likewise, MLPs were trained using the whole dataset of measurements divided into the three temperatures. To discriminate the gases, the output labels of the models were separated into air, ethanol, hydrogen, and nitrogen dioxide. Table S2 in the ESI† shows the performance of the trained classification algorithms. At 250 °C, the classification model with the highest accuracy consists of one hidden layer with 10 neurons and utilizes Tanh as the activation function. The total accuracy obtained during training was approximately 91.6%, while during the test with the observations left out for this purpose, the total accuracy was 93.18%. The confusion matrix for the test data is shown in Fig. 10a. The classification accuracy was greater than 94% when supplying dry air to the sensors, 90.1% for ethanol, 86.9% for hydrogen, and 95.2% for nitrogen dioxide. It is worth mentioning that classification errors occur mostly between target gases and air (ex: when supplying ethanol, the algorithm misclassifies 9.5% of ethanol samples as air and only 0.4% as hydrogen). There is almost no confusion among the target gases. Similarly, models were trained to quantify the gases. Tables S3–S5 in the ESI† compare the results according to RMSE and R^2 for NO_2, EtOH, and H_2, respectively. For NO_2 at 250 °C, the best model comprised three hidden layers, 10 neurons per layer, and ReLU as the activation function. This model results in an RMSE of 0.08 ppb and R^2 of 0.94 for the samples left out for testing. Fig. 10b shows the predicted *vs.* true values at 250 °C for the test data. For the quantification of hydrogen at 250 °C, the best model used one hidden layer, 100 neurons per layer, and ReLU as the activation function. The RMSE increases to 85.57 ppm but is still a good result, since the measured concentration range for H_2 is up to 1000 ppm. The R^2 value is 0.94, see Fig. 10c. In the case of ethanol, the best model had three hidden layers, 10 neurons per layer, and Tanh as the activation function. For test data, RMSE was 1.64 ppm and R^2 was 0.94, see Fig. 10d.

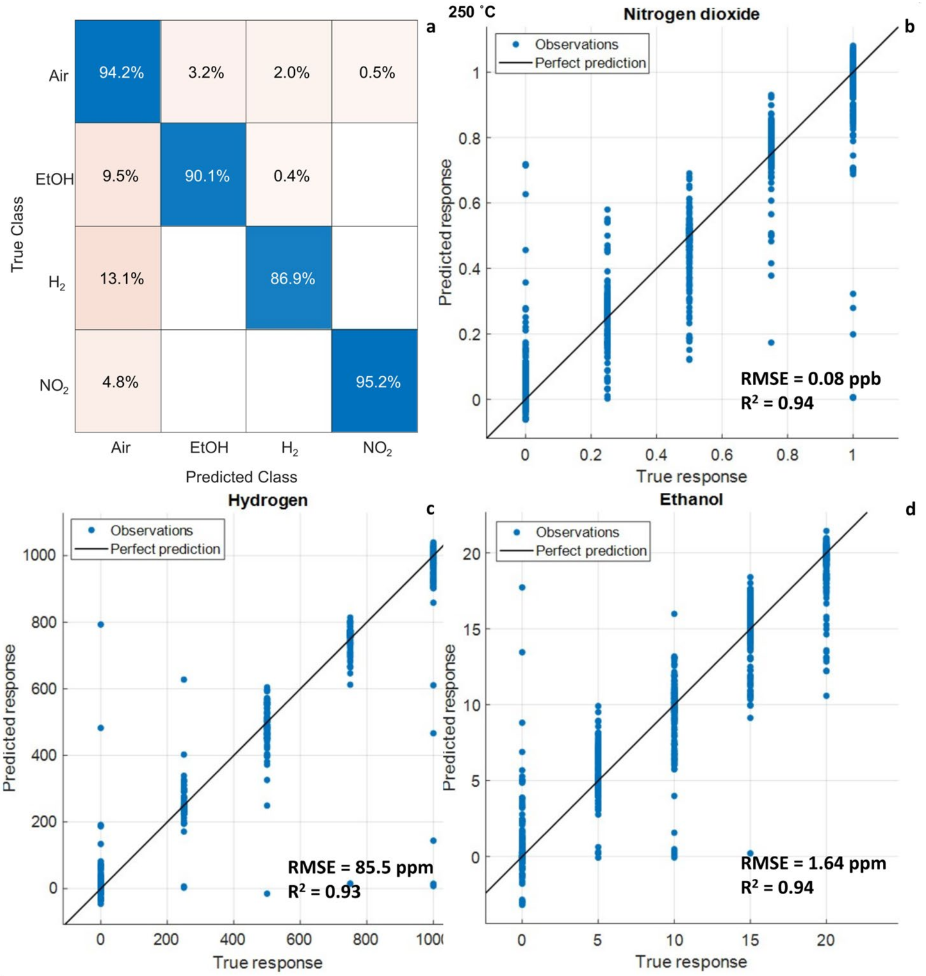

Fig. 10 Results of the classification (a) and quantification models NO_2, (b) H_2, (c) and EtOH (d). Input data is from the three-sensor array. Sensors were operated at 250 °C.

At 200 °C, the classification accuracy was greater than 92% when classifying air, 89.4% for ethanol, 82.2% for hydrogen, and 96.1% for nitrogen dioxide, see Fig. S6a†. The best quantification model for NO_2 had one hidden layer, 100 neurons per layer, and ReLU as the activation function. It gave as a result an RMSE of 0.11 ppb and R^2 of 0.89 for test data. Fig. S6b† shows the predicted *vs.* true values at 200 °C for the test data. For the quantification of hydrogen at 200 °C, the best model also had one hidden layer, 100 neurons per layer, and ReLU as the activation function. Fig. S6c† shows the result for test data, RMSE of 107.92 ppm and the R^2 0.90. Fig. S6d† shows the test results of the best model for ethanol quantification. The model comprised three hidden layers, 10 neurons per layer, and Sigmoid as the activation function. RMSE was 1.27 ppm and R^2 was 0.96 for test data. Results at 150 °C are displayed in Fig. S7†. Classification accuracy of 97.4% for air, 81.4% for ethanol, hydrogen 73.5%, and 96% for NO_2 was achieved, see Fig. S7a†. The best prediction model for ethanol comprised one hidden layer, 100 neurons per layer, and Tanh as the activation function. For predicting nitrogen dioxide, the best model comprised three hidden layers, 10 neurons per layer, and Tanh as the activation function. For hydrogen, the quantification model comprised one hidden layer, 100 neurons per layer, and ReLU as the activation function. The results of test data are presented in Fig. S7 in the ESI†.

The operating temperature of the sensors impacts the performance achieved by the discrimination and the quantification models. If the sensor operating temperature decreases, accuracy decreases when classifying reducing gases. On the other hand, when classifying an oxidizing gas like NO_2, the classification accuracy barely changes when the working temperature of the sensors is decreased within the temperature range studied. This is summarized in Table S6 in the ESI†. This behavior could be used to reduce power consumption when classifying NO_2. Moreover, quantification results show that the best performance is reached at higher operating temperatures. Table S7† summarizes the best model for quantifying each target gas at different working temperatures.

The metrics (accuracy, *R*-squared, and RMSE) of the models built to discriminate and quantify the target gases are comparable or even better than those of the state of the art [52]. Additionally, Table S8† enables the comparison of the results achieved with some recent results from the literature.

4. Conclusion

The AACVD technique has been employed in a two-step process to successfully grow tungsten oxide nanowires pure and loaded with two amounts of osmium oxide nanoparticles. FESEM and HR-TEM analysis has verified that the synthesized materials were crystalline, and the loading of osmium impacted the layer morphology. Despite being unable to determine the presence of osmium nanoparticles through microanalysis (EDX), the ToF-SIMS analysis confirms the presence of osmium on loaded samples, yet at trace levels. The gas-sensing properties of the obtained nanomaterials have been successfully studied under the presence of nitrogen dioxide, hydrogen, and ethanol at ppb and ppm levels. It was found that osmium loaded sensors hold promise for the detection of H_2 and NO_2.

Additionally, the response data from the three sensors was processed using two different multivariate techniques such as PCA and MLP. These results show that a 3-element sensor array, made of cross-responsive sensors, is able to discriminate and quantify the target gases with good accuracy. Particularly, the processing of the sensor array data using artificial neural network models allowed for reaching a high discrimination ability (H_2: > 86%, EtOH > 90%, and NO_2: > 96%) and a good quantification ability ($R^2 \sim 0.94$) on validation data that had not been used for training.

Despite our results show that the multivariate data analysis approach enhances the selectivity and quantification ability of the cross-responsive, pure and osmium loaded tungsten oxide sensors, further research is needed. For instance, the optimization of the amount of osmium in the loading process of each sensor should help enhancing sensor performance. This will require a careful optimization of the AACVD process, which has resulted in low loading levels. Also, performing new measurements for a longer period than the 2 months measurement period reported here would help understanding how the sensors age, and evaluating their long-term stability.

References

1. Monitoring air pollution levels is key to adopting and implementing WHO's Global Air Quality Guidelines, https://www.who.int/news/item/10-10-2023-monitoring-air-pollution-levels-is-key-to-adopting-and-implementing-who-s-global-air-quality-guidelines, (accessed 2 May 2024).
2. M. L. Grilli *Metals*, 2020, **10**, 820.
3. R. J. Rath, S. Farajikhah, F. Oveissi, F. Dehghani and S. Naficy, *Adv. Eng. Mater.*, 2023, **25**, 2200830.
4. J. Chen, C. Burger, C. V. Krishnan and B. Chu, *J. Am. Chem. Soc.*, 2005, **127**, 14140 —14141.
5. A. Umar, A. A. Ibrahim, R. Kumar, H. Algadi, H. Albargi, M. A. M. Alhamami, U. T. Nakate and S. Baskoutas, *Sci. Adv. Mater.*, 2021, **13**, 724 —733.
6. A. Umar, J. Singh, A. A. Ibrahim, R. Kumar, P. Rai, A. K. Rai, H. Algadi, M. A. M. Alhamami and M. M. E. Elsddig, *Sci. Adv. Mater.*, 2021, **13**, 2358 —2363.
7. X. C. Song, Y. F. Zheng, E. Yang and Y. Wang, *Mater. Lett.*, 2007, **61**, 3904 —3908.
8. X. Gao, X. Su, C. Yang, F. Xiao, J. Wang, X. Cao, S. Wang and L. Zhang, *Sens. Actuators, B*, 2013, **181**, 537 —543.
9. H. Zheng, J. Z. Ou, M. S. Strano, R. B. Kaner, A. Mitchell and K. Kalantar-zadeh, *Adv. Funct. Mater.*, 2011, **21**, 2175 —2196.
10. S. Vallejos, P. Umek, T. Stoycheva, F. Annanouch, E. Llobet, X. Correig, P. De Marco, C. Bittencourt and C. Blackman, *Adv. Funct. Mater.*, 2013, **23**, 1313 —1322.

11. Y.-T. Hsieh, L.-W. Chang, C.-C. Chang and H. C. Shih, *Electrochem. Solid-State Lett.*, 2011, **14**, K40.

12. E. Rossinyol, J. Arbiol, F. Peiró, A. Cornet, J. R. Morante, B. Tian, T. Bo and D. Zhao, *Sens. Actuators, B*, 2005, **109**, 57 —63.

13. B. Tian, X. Liu, L. A. Solovyov, Z. Liu, H. Yang, Z. Zhang, S. Xie, F. Zhang, B. Tu, C. Yu, O. Terasaki and D. Zhao, *J. Am. Chem. Soc.*, 2004, **126**, 865 —875.

14. A. Rumplecker, F. Kleitz, E.-L. Salabas and F. Schüth, *Chem. Mater.*, 2007, **19**, 485 —496.

15. M. Hafeez, A. Siddique Saleemi, S. Ur Rehman, M. Adrees, S. Mehmood, I. A. Mir and L. Zhu, *Appl. Surf. Sci.*, 2021, **536**, 147713.

16. W. B. Carter, G. W. Book, T. A. Polley, D. W. Stollberg and J. M. Hampikian, *Thin Solid Films*, 1999, **347**, 25 —30.

17. G. Carta, N. El Habra, L. Crociani, G. Rossetto, P. Zanella, A. Zanella, G. Paolucci, D. Barreca and E. Tondello, *Chem. Vap. Deposition*, 2007, **13**, 185 —189.

18. D. Barreca, G. Carraro, E. Fois, A. Gasparotto, F. Gri, R. Seraglia, M. Wilken, A. Venzo, A. Devi, G. Tabacchi and C. Maccato, *J. Phys. Chem. C*, 2018, **122**, 1367 —1375.

19. S. Blittersdorf, N. Bahlawane, K. Kohse-Höinghaus, B. Atakan and J. Müller, *Chem. Vap. Deposition*, 2003, **9**, 194 —198.

20. M. Lugo-Ruelas, P. Amézaga-Madrid, O. Esquivel-Pereyra, W. Antúnez-Flores, P. Pizá-Ruiz, C. Ornelas-Gutiérrez and M. Miki-Yoshida, *J. Alloys Compd.*, 2015, **643**, S46 —S50.

21. D. Barreca, G. Carraro, A. Gasparotto, C. Maccato, R. Seraglia and G. Tabacchi, *Inorg. Chim. Acta*, 2012, **380**, 161 —166.

22. H. Meixner and U. Lampe, *Sens. Actuators, B*, 1996, **33**, 198 —202.

23. C. Zhang, Y. Luo, J. Xu and M. Debliquy, *Sens. Actuators, A*, 2019, **289**, 118 —133.

24. F. E. Annanouch, Z. Haddi, S. Vallejos, P. Umek, P. Guttmann, C. Bittencourt and E. Llobet, *ACS Appl. Mater. Interfaces*, 2015, **7**, 6842—6851.

25. F. E. Annanouch, Z. Haddi, M. Ling, F. Di Maggio, S. Vallejos, T. Vilic, Y. Zhu, T. Shujah, P. Umek, C. Bittencourt, C. Blackman and E. Llobet, *ACS Appl. Mater. Interfaces*, 2016, **8**, 10413—10421.

26. E. Navarrete, C. Bittencourt, P. Umek, D. Cossement, F. Güell and E. Llobet, *J. Alloys Compd.*, 2020, **812**, 152156.

27. È. Navarrete, C. Bittencourt, X. Noirfalise, P. Umek, E. González, F. Güell and E. Llobet, *Sens. Actuators, B*, 2019, **298**, 126868.

28. E. Navarrete, C. Bittencourt, P. Umek and E. Llobet, *J. Mater. Chem. C*, 2018, **6**, 5181 —5192.

29. P. Velusamy, R. Xing, R. R. Babu, E. Elangovan, J. Viegas, S. Liu and M. Sridharan, *Sens. Actuators, B*, 2019, **297**, 126718.

30. P. Velusamy, R. Ramesh Babu, M. Sathiya, A. Ahmad, A. A. Alothman, M. Sheikh Saleh Mushab, E. Elamurugu, M. Senthil Pandian and P. Ramasamy, *New J. Chem.*, 2022, **46**, 22469 —22485.

31. V. Periyasamy, R. R. Babu, A. Ahmad, M. D. Albaqami, R. G. Alotabi and E. Elamurugu, *ACS Omega*, 2022, **7**, 35191 —35203.

32. V. P, X. Liu, R. Ramesh Babu, M. Sathiya, N. Salem Alsaiari, F. Mohammed Alzahrani, M. Tariq Nazir, E. Elamurugu and F. Zhang, *Chemosphere*, 2023, **329**, 138535.

33. S. B. Malik, E. Llobet and F. E. Annanouch, *Eurosensors 2023*, MDPI, Basel Switzerland, 2024, vol. 97, p. 133.

34. S. B. Malik, K. V. Mejia-Centeno, P. R. Martínez-Alanis, A. Cabot, F. Güell, F. E. Annanouch and E. Llobet, *Sens. Actuators, B*, 2024, **400**, 134879.

35. S. B. Malik, F. E. Annanouch and E. Llobet, *2023 IEEE Sensors, IEEE*, 2023, pp. 1–4.

36. S. B. Malik, F. E. Annanouch and E. Llobet, *Chemosensors*, 2023, **11**, 550.

37. S. Agarwal, P. Rai, E. N. Gatell, E. Llobet, F. Güell, M. Kumar and K. Awasthi, *Sens. Actuators, B*, 2019, **292**, 24 —31.

38. C. Wang, L. Yin, L. Zhang, D. Xiang and R. Gao, *Sensors*, 2010, **10**, 2088 —2106.

39. V. B. Kamble and A. M. Umarji, *RSC Adv.*, 2015, **5**, 27509 —27516.

40. S. Yang, G. Lei, H. Xu, Z. Lan, Z. Wang and H. Gu, *Nanomaterials*, 2021, **11**, 1026.

41. D. Y. Nadargi, A. Umar, J. D. Nadargi, S. A. Lokare, S. Akbar, I. S. Mulla, S. S. Suryavanshi, N. L. Bhandari and M. G. Chaskar, *J. Mater. Sci.*, 2023, **58**, 559 —582.

42. F. Quaranta, R. Rella, P. Siciliano, S. Capone, M. Epifani, L. Vasanelli, A. Licciulli and A. Zocco, *Sens. Actuators, B*, 1999, **58**, 350 —355.

43. S. Capone, M. Epifani, F. Quaranta, P. Siciliano and L. Vasanelli, *Thin Solid Films*, 2001, **391**, 314 —319.

44. J. Pan, A. Yang, D. Wang, J. Chu, F. Lei, X. Wang and M. Rong, *IEEE Trans. Instrum. Meas.*, 2022, **71**, 1 —8.

45. L. Zhao, F. Tian, J. Qian, H. Li and Z. Wu, *IEEE Trans. Instrum. Meas.*, 2023, **72**, 1 —9.

46. Z. Ye, Y. Liu and Q. Li, *Sensors*, 2021, **21**, 7620.

47. H. Chen, D. Huo and J. Zhang, *IEEE Trans. Biomed. Circuits Syst.*, 2022, **16**, 169 —184.

48. N. Ha, K. Xu, G. Ren, A. Mitchell and J. Z. Ou, *Advanced Intelligent Systems*, 2020, **2**, 2000063.

49. I. T. Jolliffe and J. Cadima, *Philos. Trans. R. Soc., A*, 2016, **374**, 20150202.

50. K. Zhou and Y. Liu, *Sensors*, 2021, **21**, 4826.

51. S. H. Wang, T. I. Chou, S. W. Chiu and K. T. Tang, *IEEE Sens. J.*, 2021, **21**, 6401 —6407.

52. Md. S. I. Sagar, N. R. Allison, H. M. Jalajamony, R. E. Fernandez and P. K. Sekhar, *J. Electrochem. Soc.*, 2022, **169**, 127512.

Chapter 3

Integration of chemoresistor sensors with hardware, software, and statistical data analysis

The following chapter presents the integration of chemoresistor sensors with a hardware and software design, including data analysis. The hardware and software bridge the chemical reaction (between the sensitive layer of the sensors with the target analyte), to a final visual user interface. Also, implementing statistical methods on the software improves the accuracy and metrics of the discrimination and quantification process for the final system.

This integration is presented in Section 3.1, through a published paper named "IoT Platform Enhanced with Neural Network for Air Pollutant Monitoring".

Section 3.1

IoT Platform Enhanced with Neural Network for Air Pollutant Monitoring

Alejandro Santos-Betancourt, José Carlos Santos-Ceballos, Foad Salehnia, Mohamed Ayoub Alouani, Alfonso Romero, José Luis Ramírez, and Xavier Vilanova

IEEE Transactions on Instrumentation and Measurement,
Vol: 73, 2024, ASN: 2534511,

DOI: 10.1109/TIM.2024.3481592

Abstract

This work presents the design and setup of an IoT platform at level four of the technology readiness level (TRL-4) to detect, classify, and quantify pollutant gases. This study combines concepts such as wireless sensor networks (WSNs), arrays of sensors, and multivariate data analysis to interface different nanostructured chemoresistor gas sensors. The IoT platform consists of several gas sensor nodes (GSNs) with Wi-Fi capability to send data from a sensor array to a server and its user interface (UI). Each GSN interfaces one sensor array (up to four chemoresistor gas sensors and one temperature and humidity sensor). The server channels the data from the GSNs to the UI. The platform was set up following a two-stage methodology. First (training stage), sensor data were received, stored, and used to train different multilayer perceptrons (MLPs) artificial neural networks (ANNs). Second (recognition stage), models were implemented in the UI to classify and quantify the presence of pollutants. The platform was tested in laboratory conditions under exposure to nitrogen dioxide and ammonia at a different %RH. As a result, the platform improves the classification and quantification times compared with the single-sensor approach. In addition, the system was evaluated using a gas mixture of both gases, showing a classification accuracy exceeding 99%. Likewise, the training and recognition stages can be repeated to add new chemoresistor gas sensors in the node, add new nodes to the platform, and deploy the nodes in different scenarios.

Index Terms

Air pollution monitoring, ammonia, gas sensor, IoT, laboratory-made sensors, mixture of gases, multilayer perceptron (MLP), multivariate analysis, nitrogen dioxide.

I. INTRODUCTION

Gas sensors and their read-out instrumentation systems are essential components in various industry applications due to their crucial role in ensuring safety, enhancing efficiency, and maintaining environmental standards. In different industries such as petrochemical [1] and energy [2], measurement systems interfacing with gas sensors provide reliable data that can prevent dangerous situations such as explosions, toxic exposures, and asphyxiation risks [3], [4]. Likewise, these measurement systems contribute significantly to air quality monitoring by detecting pollutants, enabling industries to comply with environmental regulations and minimize their ecological impact. Similarly, they play a fundamental role in air quality control systems, helping to reduce exposure to harmful substances such as carbon monoxide, nitrogen dioxide, ammonia, and volatile organic compounds in the environment [5].

In past decades, many research efforts have focused on developing reliable gas sensors for detecting pollutant gases. Nowadays, continuous and active research is directed at discovering new materials to increase the response and the selectivity of new sensors [6], [7]. Different gas sensor fabrication techniques such as those based on field effect transistors [8], optical gas sensors [9], and electrochemical sensors [10] have high sensitivity, high selectivity, and fast response time. They also have some downsides such as long-term stability issues. Moreover, their complex designs, fabrication processes, and read-out systems increase the deployment and maintenance costs. On the other hand, chemoresistor gas sensors have emerged as a promising option, as they gather many of the requirements needed in the next generation of low-cost gas sensors. Chemoresistor gas sensors usually show high sensitivity to gases and fast response and recovery times [11], [12]. However, some drawbacks are still challenging, such as the lack of selectivity to specific target gases, temperature and humidity interferences, long-term drift, and high working temperatures [13]. Nontarget gases with similar chemical characteristics can interfere with the gas sensor, especially when detecting mixtures of gases. In addition, sensor drift is a substantial issue, mainly in outdoor settings when detecting low-concentration levels of analytes. Likewise, the accuracy of chemoresistor gas sensors is directly impacted by environmental variables, as sensor adsorption abilities might vary under the variation of these conditions [14].

A promising area of research to partially solve these issues is the use of chemoresistor sensors such as MOX-based sensors doped or decorated with other materials such as graphene [15], [16] or conductive polymers [17]. Combining this approach with the use of arrays of sensors and multivariate analysis [18], [19] allows the compensation of the interferences that a single sensor might have. The multivariate analysis uses different statistics techniques and machine learning (ML) algorithms [20], [21]. Plenty of methods for the classification and quantification of pollutant gases have been reported, comprising principal component analysis (PCA), linear discriminant analysis (LDA), partial least-squares (PLSs) regression, principal component regression (PCR), decision tree (DT), support vector machine (SVM), *k*-nearest neighbor (KNN), and artificial neural networks (ANNs) [22], [23], [24].

ML methods have also been used to detect a mixture of gases. Chu et al. [25] identify a mixture of NO_2 and CO in a wide range of concentrations using a sensor array and PCA, BPNN, and CNN. They also evaluate the effect of %RH and compensate for it. Kim et al. [26] used PCA and ANN to recognize a mixture of CO and NH_3 under the presence of NO_2 and recognize NO_2 in the presence of CO and NH_3. Similarly, Zhang et al. [27] used LDA, PCA, and BP-ANN methods to classify CO and CH_4 and their mixture. Also, the authors repeated the experiment by adding interfering species such as H_2 and formaldehyde. All these works and others that can be found in the literature focused on improving feature extraction and data analysis to enhance the classification and quantification output of sensors. They are the groundwork for integrating ML techniques into gas sensing systems. On the other hand, gas sensors have also been integrated into wireless sensor networks (WSNs), estimating the location of gas sources [28], using cutting-edge IoT wireless technologies [29], or being part of distributed devices for air quality monitoring [30], for instance.

We strongly believe that most of these cited features should be integrated into future gas-sensing instrumentation systems to solve the abovementioned issues. This work combines several of these characteristics and applies them to a chemoresistor sensor array developed in our research group. It presents a reconfigurable and adaptative design of an IoT platform at level 4 of the technology readiness level (TRL-4) to detect, classify, and quantify pollutant gases. Details are cited about the fabrication processes of the chemoresistor gas sensors, based on previous experience of our research group, using techniques such as airbrushing [31], [32], laser-induced graphene [33], [34], and aerosol-assisted chemical vapor deposition (AA-CVD) [35], [36]. Also, a full explanation is given about the design of the gas sensor nodes (GSNs), highlighting their versatility as they can interface with all kinds of chemoresistor gas sensors developed in our research group.

In addition, to properly set up the platform, one of the nodes was exposed to different concentrations of ammonia and nitrogen dioxide. Likewise, the percentage of relative humidity was varied, and a mixture of these two pollutants was also sourced to the node. These two gases were chosen due to their crucial role in atmospheric chemistry and the formation of secondary pollutants. On one side, ammonia is largely emitted from agricultural activities [37], including the use of fertilizers [38] and livestock [39]. Nitrogen dioxide, on the other hand, is generally produced from combustion processes, such as vehicle emissions [40] and industrial activities [41]. However, both can be present in places such as agricultural regions near urban or industrial areas. Also, high levels of nitrogen dioxide can often be found inside big cities due to traffic emissions, and ammonia can also be present in urban atmospheres, sourced from waste systems, pets, and some small industrial processes [42], [43]. These emissions are dangerous to human health; exposure to high levels of nitrogen dioxide can irritate the airways in the human respiratory system and aggravate respiratory diseases, such as asthma, increasing episodes of gasping and coughing [44], [45]. Ammonia, while less toxic than nitrogen dioxide, can also irritate the eyes, nose, throat, and respiratory tract upon high exposure levels [46].

A two-stage methodology was established as part of the platform setup process. In stage 1 (training stage), different multilayer perceptron (MLP) ANNs were trained using MATLAB Statistics and ML Toolbox (academic-available license). Then, in the second stage (recognition stage), the obtained MLPs were implemented on the user interface (UI). Repeating this methodology guarantees the reusability of the GSNs with new sensors, the addition of new GSNs to the platform, and the deployment of the platform in different scenarios.

A compilation of systems that use an array of laboratory-made (noncommercial) sensors and support wireless technology found in the literature is summarized in Table I. As shown in Table I, Song et al. [47] perform an indoor deployment of the system but do not consider environmental variables to feed the models. On the other hand, Nath et al. [48] performed an outdoor deployment but did not include ML models in the study. Moreover, Seol et al. [49] incorporated environmental variables but did not add ML models to their results. It is worth noting that this work classifies the type of gas in the atmosphere and quantifies its concentration using ML techniques (in dynamic operation), under a mixture of the target gases, at different percentages of relative humidities; integrating into a platform the aforementioned solutions enhances the output of current gas sensors developed in our research group.

TABLE I:
COMPARISON BETWEEN AVAILABLE SYSTEMS AND THIS WORK

Gas	**Mix of gases**	**Hum & Temp**	**Wireless tech**	**Classif. algorithm**	**Quantif. algorithm**	**Ref**
*	2	-	BT	PCA/ SVM	3	60
**	-	-	Wi-Fi	-	-	61
NH_3	4	-	Wi-Fi	-	-	62
H_2S, CO	-	-	BLE/ Wi-Fi	PCA	-	63
EtOH	-	Yes	BLE	-	-	64
NO_2, NH_3	Yes	Yes	Wi-Fi	ANNs	ANNs	This work

* H_2, formaldehyde, toluene, acetone,

** CH_4, H_2, N_2,

[2] indoor deployment,

[3] fitting power-law function,

[4] outdoor deployment

II. MATERIALS AND METHODS

A. Design and Development of the IoT Platform

The general overview of the platform is depicted in Fig. 1. The platform has three main parts: a server running a Message Queuing Telemetry Transport (MQTT) broker, a UI, and the GSNs interfacing with an array of sensors. A Raspberry Pi was used as a server. Free Eclipse Mosquitto broker was used as the MQTT broker, bridging the raw data from the GSNs to the UI. MQTT is a public-subscribe protocol that allows the integration of as many GSNs as needed into the platform, facilitating the visualization of the data and multiuser combination. Therefore, new devices could be added to the platform by being subscribed to specific new topics.

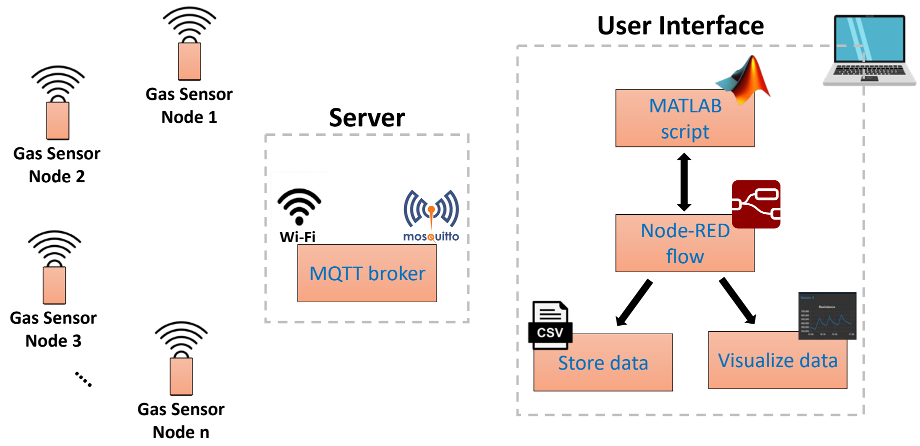

Fig. 1. Block diagram of the IoT platform

The design of the UI was divided into two steps. First, the open-source programming tool Node-RED was used to receive, visualize, and store the data from one of the GSNs. Then, the entire dataset was used to train MLPs (training stage). The second step consisted of creating a new version of the program on Node-RED that uses the previously trained MLPs (recognition stage). To do so, Node-RED communicates with a MATLAB script that preprocesses the sent data from the GSNs and executes the MLPs to quantify and classify the target gas. The GSNs send the raw data from sensors through the MQTT protocol in JSON format (see Fig. S1 in Supplementary Materials). The array of sensors included in the GSNs is formed by a commercially available BME680 sensor (Bosch Sensortec GmbH, Germany) to acquire the humidity and temperature, and four chemoresistor gas sensors (two based on tungsten trioxide, fabricated using AA-CVD technique, and two based on graphene, fabricated by airbrushing and laser-induced graphene techniques). The fabrication process and the characterization of these sensors were previously reported by our research group [31], [32], [33], [34], [35], [36]. Furthermore, Figs. S2–S4 in the Supplementary Materials summarize the fabrication details.

Finally, the GSNs were fully designed in this work. They are wirelessly connected using Wi-Fi technology with the idea of reusing the extensive coverage of this wireless technology in urban and industrial places. Their main blocks are shown in Fig. 2(a). Key components on the board are the microcontroller, the sensors, the analog acquisition channel, the temperature control circuit, and the power source. The fabricated version of the nodes is shown in Fig. 2(b). It can be noticed that the nodes have a modular design, and an Arm1 Cortex 1-M0 32-bit SAMD21 microcontroller (Arduino MKR 1000 Wi-Fi) is connected to the rest of the electronic (green board) through a pin heather connector. This gives the possibility of replacing the MKR 1000 with any pin-compatible MKR-family board to change the type of wireless connectivity according to the final application (e.g., MKR WAN 1300 for LoRa and MKR NB 1500 for narrowband).

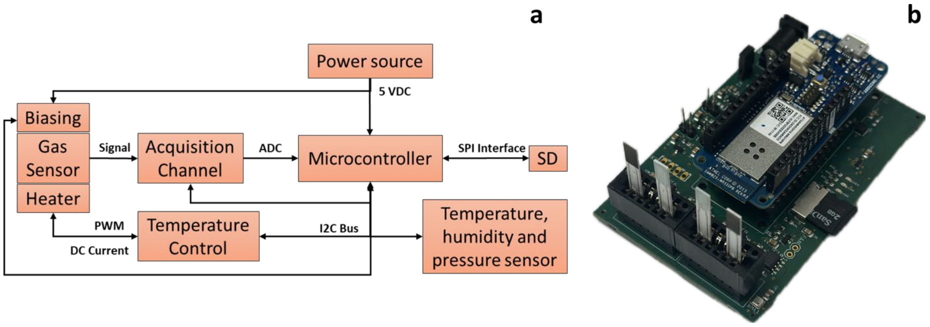

Fig. 2. (a) Block diagram of the GSNs. (b) Final design of the GSNs.

The software was also designed in different layers, separating the functionalities related to wireless communication from the other functionalities. Fig. S5 in the Supplementary Materials shows a general flow diagram of the software running in the microcontroller. After loading the start-up configuration, the software performs different control algorithms to guarantee the operation of the sensors connected to the node. The first control algorithm supervises a suitable bias for the sensors in every measurement task. To do so, the biasing circuit continuously checks the value of each sensor and adjusts the bias value using a digital potentiometer (AD5241 I^{2}C-Compatible 256-Position). This feature compensates for the wide range of baseline resistance values (typically of hundreds of kΩ) that a chemoresistor gas sensor might have and covers up to 1 MΩ. The second control algorithm checks the voltage saturation in the input of the analog-to-digital converter, modifying the gain (if needed) of the measurement channel by changing the feedback resistance of an operational amplifier (using a second digital potentiometer).

Another widely known characteristic of this type of sensor is that most of them require high temperatures to operate [13], [14]. Therefore, the third control algorithm dynamically sets the desired working temperature of the sensor. This is done by repeatedly reading the current through the heater of the sensors using an INA219 Zerø-Drift, Bidirectional Current/Power Monitor with I^{2}C Interface. This current value is the input of the PID control algorithm. Its output is an increase/decrease of the duty cycle of a pulse width modulation (PWM) signal connected to the gate of a p-type MOSFET transistor (NX2301P). The current through the heater can be varied up to 500 mA, covering a wide range of working temperatures. It is worth mentioning that the GSNs support up to four chemoresistor gas sensors independently controlled.

The last control algorithm manages the data after a failure/recovery wireless connection. The data would be stored in a μSD memory card if the wireless connection is not established. Once the connection is recovered, the collected data will be sent to the server while simultaneously continuing the data acquisition process. Furthermore, the µSD memory card stores all the start-up and dynamic configurations of the board. Consequently, it is ensured that all the configuration parameters will be unaltered even in the event of a power outage. Finally, the software executes the mentioned algorithms in periodically set tasks such as Read data from sensors and Send data to the server. Sensors are read at a 1-Hz rate, and every 10 s, the average of these values is sent to the server.

B. Gas Characterization Room

The proper working of the platform was tested using one node. The array of sensors in the node was formed by one sensor made of graphene decorated with zinc oxide (Graphene@ZnO) [31], [32], another sensor made of laser-induced graphene decorated with polypyrrole (LIG@Ppy) [33], [34], and the other two sensors were based on pristine tungsten trioxide at two levels of temperatures [35], [36]. The graphene-based sensors were kept at room temperature, while tungsten trioxide sensors were set at 300 °C and 250 °C. It is known in the literature that graphene sensors can work at room temperature, and metal oxide sensors perform better at high temperatures [52], [53]. The node was exposed to different target gases using the system in the gas characterization room illustrated in Fig. 3. The gas measurement system consists of gas bottles with calibrated gas concentrations balanced in dry air, a carrier gas with zero-grade dry air, and an acrylic chamber with an inner volume of 5000 cm^3. The gases were delivered into the chamber through a computer-controlled mass-flow system to ensure a constant low flow of 200 mL/min. The mass flows are controlled by software named Flow Plot v3.34, running on a Windows-based computer. The node was placed inside the chamber and left under dry synthetic air for 3 h to have a stable baseline resistance of the sensors. The data from the four gas sensors and the temperature and humidity sensor were received in Node-RED.

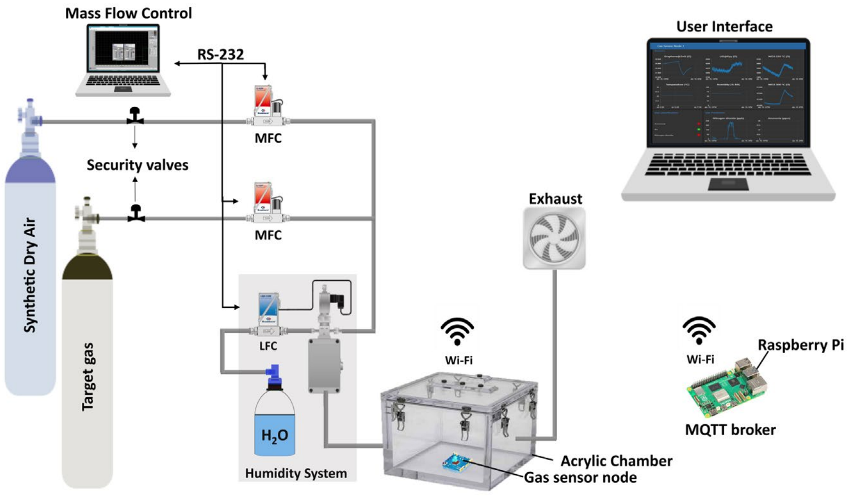

Fig. 3. Schematic of the gas characterization room.

The first set of measurements was established as pulses of nitrogen dioxide, which were injected into the chamber with different concentrations ranging from 100 to 500 ppb incremented by 100 ppb. The second type of measurement targeted ammonia, ranging in concentrations from 10 to 50 ppm incremented by 10 ppm. In both cases, dry air was supplied between the gas pulses to recover the baseline keeping the constant flow. The gas exposure time was 45 min, and the recovery dry airtime was 180 min for each pulse. The cycle of pulses was repeated three times. The humidity level was set by humidifying the gas stream through a controller evaporator mixer from Bronkhorst (Bronkhorst High-Tech, Ruurlo, The Netherlands), and all the described measurements were performed two times under a high humidity level around 65% RH and a low humidity level around 25% RH. Measurements under dry air conditions were not performed because this work focuses on a practical application. Afterward, both gases were injected into the chamber at the same time, exposing the system to a mixture of gases. In this case, the pulses of gases were distributed as follows: five pulses of 25 ppm of ammonia for 90 min and recovery of 3 h and then from 45 to 90 min of each pulse of ammonia; a stream of pulses of nitrogen dioxide was injected as done before 100, 200, 300, 400, and 500 ppb. This cycle was repeated three times. Subsequently, the same procedure was done increasing the ammonia to 50 ppm.

C. *Methodology: Training Stage*

The following methodology (training stage) was employed to preprocess, train, and test MLPs to classify and quantify the target gases. Fig. S6 in the Supplementary Materials shows the general structure of the MLPs. The electrical resistance of the four gas sensors, along with the data from the temperature and humidity sensor, serves as the input features (input layer) for the training process. First, the array of sensor raw data was filtered using an asymmetric windowed filter with a left-right length of 12 and 0 samples, respectively. Afterward, to transform the values of the features into a common scale (0–1), a min/max normalization technique was used. The normalization process for temperature and humidity sensors was done from 0 °C to 50 °C and from 0% RH to 100% RH. In the case of the gas sensors, the selected range varied according to the resistance values of each baseline. For training, 80% of observations were used, and the remaining 20% were reserved for testing the MLPs, selected randomly for these purposes. A fivefold cross-validation scheme was used to avoid overfitting during the training process. The tuning process compares different types of architecture (hidden layers), varying the number of layers (1, 2, 3) and neurons per layer (10, 25, 100). The MLP with superior performance was selected based on root mean squared error (RMSE) and coefficient of determination (R^2) for quantification and accuracy for classification. Once the architecture of the MLP was fixed, the activation function was varied between ReLU, $f(x) = \max(0, x)$, Sigmoid: $f(x) = \frac{1}{1+ e^{-x}}$, and Tanh: $f(x) = \frac{2}{1+ e^{-2x}} - 1$, to decide the best option.

III. RESULTS

A. *Gas Sensing Results*

The output of the node under nitrogen dioxide exposure is depicted in Fig. 4(a)–(f). Similarly, Fig. 4(g)–(l) shows the output under ammonia exposure.

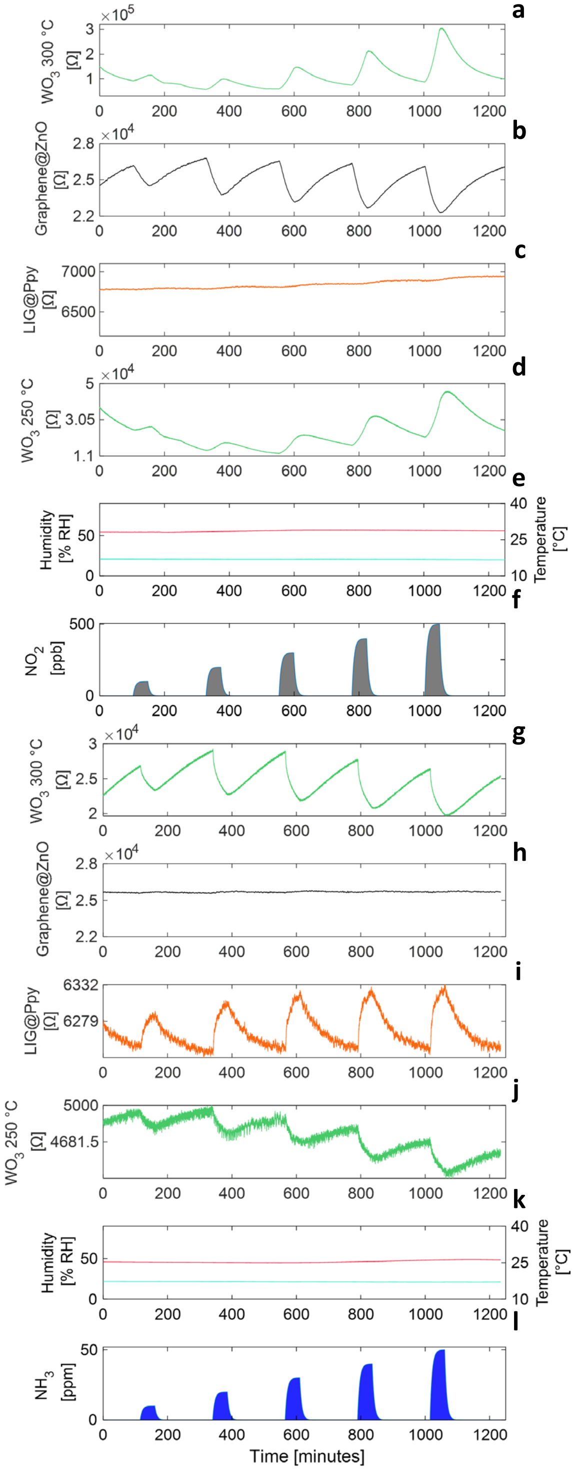

Fig. 4.

Temporary response of the sensors to nitrogen dioxide.

(a) Tungsten trioxide at 300 °C.
(b) Graphene@ZnO.
(c) LIG@Ppy.

(d) Tungsten trioxide at 250 °C.
(e) Temperature and humidity.
(f) Nitrogen dioxide pulses: 100, 200, 300, 400, and 500 ppb.

Temporary response of the sensors to ammonia.
(g) Tungsten trioxide at 300 °C.
(h) Graphene@ZnO.
(i) LIG@Ppy.

(j) Tungsten trioxide at 250 °C.
(k) Temperature and humidity.
(l) Ammonia pulses: 10, 20, 30, 40, and 50 ppm.

As noticed in Fig. 4(a), the tungsten trioxide sensor at 300 °C increases its electrical resistance when reacting to nitrogen dioxide. Also, the sensor decreases the electrical resistance of the sensing layer when reacting to ammonia [see Fig. 4(g)]. As expected, the sensor based on Graphene@ZnO decreases its electrical resistance when exposed to nitrogen dioxide [see Fig. 4(b)]. However, there is no change in the electrical resistance when exposed to ammonia [see Fig. 4(h)] [31], [32].

On the other hand, the sensor fabricated using LIG@Ppy presents no variation when exposed to nitrogen dioxide [see Fig. 4(c)] and increases its electrical resistance when exposed to ammonia [see Fig. 4(i)] [33], [34]. Moreover, Fig. 4(d) and (j) depicts the tungsten trioxide sensor at 250 °C. This sensor shows the same behavior as the tungsten trioxide sensor at 300 °C but with lower amplitude variation. It is also noticed that a small drift attributed to the sensor is not fully recovered after the gas exposure due to the lower working temperature. Fig. 4(e) and (k) displays the variation of % RH and temperature in nitrogen dioxide and ammonia scenarios, respectively. Finally, Fig. 4(f) and (l) shows a simulation of the increasing gas concentration inside the chamber, from 10 to 50 ppm (ammonia) and 100–500 ppb (nitrogen dioxide). Note S1 in the Supplementary Materials presents the details of the chosen simulated model [54], [55], [56].

Fig. 5 shows the node output under the exposure of a mixture of ammonia and nitrogen dioxide. The temporary responses of the sensors are depicted in Fig. 5(a)–(e). Fig. 5(f) shows the stream of mixed pulses directed to the sensors, going into the chamber: first 25 ppm of ammonia and then a pulse of increased concentration of nitrogen dioxide. In this manner, a mixture of both gases was ensured in the atmosphere.

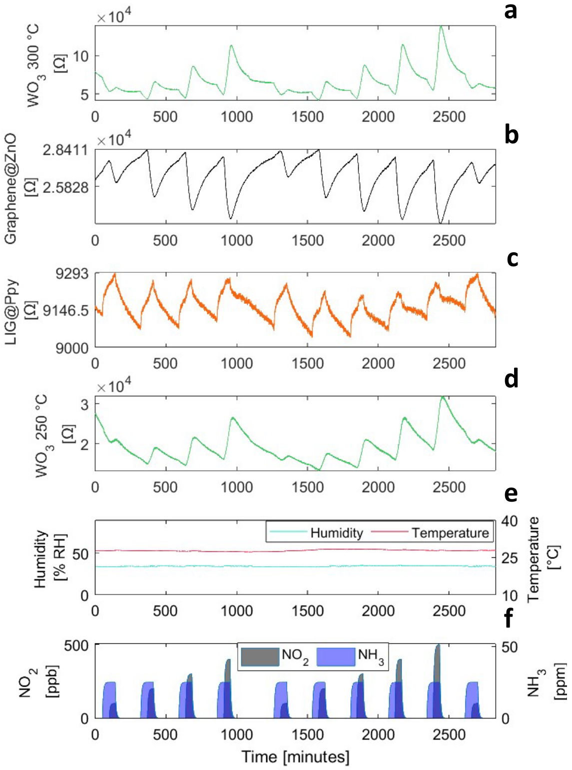

Fig. 5. Temporary response of the sensors under a mixture of ammonia and nitrogen dioxide exposure. (a) Tungsten trioxide at 300 °C. (b) Graphene@ZnO. (c) LIG@Ppy. (d) Tungsten trioxide at 250 °C. (e) Temperature and humidity. (f) Ammonia: 25 ppm mixed with pulses of nitrogen dioxide: 100, 200, 300, 400, and 500 ppb.

A detailed explanation of the waveform variation of the tungsten trioxide sensor at 300 °C is shown in Fig. 6(a). It is noticed that the electrical resistance decreases when the target gas is ammonia (red label number 1). Ammonia is still in the atmosphere when nitrogen dioxide goes into the chamber. The electrical resistance starts increasing (red label number 2). After the pulse stops, the sensor begins recovering, decreasing the electrical resistance (red label number 3). Likewise, Fig. 6(b) shows the response of the graphene-based sensors when both gases go in. First, ammonia goes into the chamber, and LIG@Ppy (plot line in orange color) increases the electrical resistance (red label number 1), while the Graphene@ZnO (plot line in black color) is still recovering from the previous pulse. After the nitrogen oxide goes into the chamber, Graphene@ZnO starts reacting (red label number 2), but the LIG@Ppy continues increasing its electrical resistance even under nitrogen dioxide. Finally, both gases go out from the chamber (red label number 3), and both sensors start recovering their baseline. The same measurements were performed by incrementing the ammonia pulses to 50 ppm, and similar results were obtained.

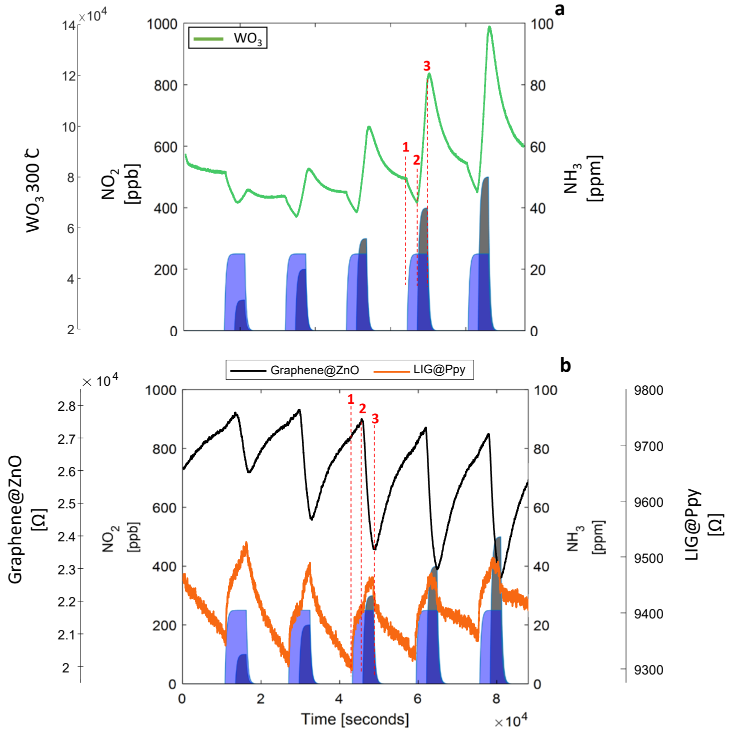

Fig. 6. Temporary response of the sensors under a mixture of ammonia and nitrogen dioxide exposure. (a) Zoomed-in view of the waveform of the tungsten trioxide sensor. (b) Zoomed-in view of the waveform of the graphene-based sensors.

B. Methodology: Training Stage Results

The MLP employed for gas classification has the output layer of three classification labels: air, ammonia, and nitrogen dioxide. Table S1 in the Supplementary Materials shows the performance of the classification MLPs. The model exhibiting the highest accuracy consists of a single hidden layer with 100 neurons and utilizes Tanh as the activation function. The total accuracy obtained during training (using only the samples of the training dataset) is approximately 98.6%, while, during the test with the observations reserved for this purpose and not used in the training, the total accuracy is 98.7%. Fig. 7(a) and (b) shows the corresponding confusion matrixes. It can be highlighted that the MLP never makes incorrect classifications between target gases. Most of the confusions were observed in the transient response of the sensors between target gas and air. The classification accuracy was greater than 99% when supplying air, 97.9% for nitrogen dioxide, and 91.5% for ammonia. The reason why the classification MLP might have lower accuracy for ammonia is presumed to be due to tungsten trioxide sensors having a higher response to nitrogen dioxide than ammonia.

To understand the influence of temperature and humidity, a classification MLP was trained using only the electrical resistance values of the four gas sensors as input features. In this scenario, the total accuracy of the MLP decreased to 97.6% (train) and 97.4% (test). Notably, in the confusion matrix shown in Fig. S7 in the Supplementary Material, the accuracy of the ammonia classification falls below 90%. This underscores the significance of integrating ambient temperature and humidity as input features into classification MLPs. On the other hand, an MLP was obtained by excluding the gas sensors with more selectivity to ammonia, LIG@Ppy, and nitrogen dioxide, Graphene@ZnO, resulting in a decrease in accuracy to 95.9% (train) and 96.2% (test). Specifically, ammonia classification dropped considerably to 72%, while nitrogen dioxide classification remained consistent at around 97% (see Fig. S8 in the Supplementary Material). This behavior can be attributed to the good response of tungsten trioxide sensors to nitrogen dioxide, indicating that the absence of the Graphene@ZnO has less influence on the classification of this gas, but is suitable for double-checking the presence of nitrogen dioxide in the atmosphere and avoids mismatches.

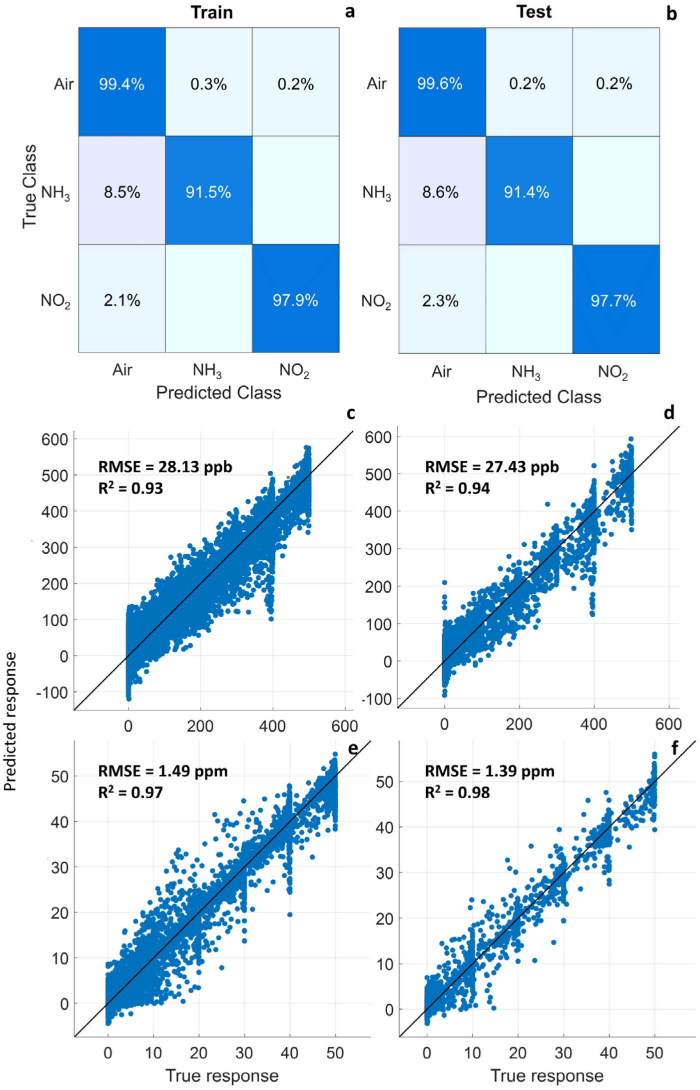

Fig. 7. Confusion matrix for the classification MLP: (a) train data and (b) test data. Results of the best MLP for nitrogen dioxide quantification: (c) train data and (d) test data. Results of the best MLP for ammonia quantification: (e) train data and (f) test data.

Ten quantification MLPs were obtained to quantify the concentration of nitrogen dioxide. Their output layer corresponds to parts per billion (ppb). Table S2 in the Supplementary Materials shows the results. The best MLP was a single hidden layer of 100 neurons, with the ReLU activation function. Fig. 7(c) illustrates the results. In the training process, an R^2 of 0.93 and an RMSE of 28.13 ppb were achieved. In testing, the R^2 score improved slightly to 0.94, with an RMSE of 27.43 ppb [see Fig. 7(d)]. Fig. S9 in the Supplementary Materials demonstrates the impact of temperature and humidity on nitrogen dioxide quantification. Not incorporating these environmental measurements as input features into the quantification model results in R^2 values falling below 0.81 and RMSE values increasing the error above 50 ppb. On the other hand, if LIG@Ppy and Graphene@ZnO are excluded from the quantification MLP, as described in Fig. S10 in the Supplementary Materials, there is an increase in the dispersion of the predicted concentrations compared to the real values. This can be seen in a decrease in the R^2 values, dropping to 0.85, and increases in RMSE more than 45 ppb.

For the prediction of ammonia concentration, quantification algorithms were developed similar to the one used for nitrogen dioxide (see Table S3 in the Supplementary Materials). In these MLPs, the output layer corresponds to the ammonia concentration in parts per million (ppm). Following the mentioned methodology, the best quantification MLP consisted of a hidden layer with 100 neurons and a sigmoid activation function. The results revealed R^2 values of 0.97 (train) and 0.98 (test) [see Fig. 7(e) and (f)] with RMSE values of 1.49 (train) and 1.39 ppm (test). As shown in Fig. S11 in the Supplementary Materials, the quantification MLP trained exclusively with the gas sensors exhibited a minor decrease in the R^2 of 0.96 and an increase in the RMSE of 1.86 ppm. Excluding LIG@Ppy and Graphene@ZnO (see Fig. S12 in the Supplementary Materials) leads to the worst performance of the MLP. R^2 values decrease below 0.90, while RMSE values exceed 3 ppm.

The same methodology was employed to obtain MLPs to classify and quantify the concentrations for a mixture of ammonia and nitrogen dioxide. In the classification process, four distinct labels were defined: air, ammonia, nitrogen dioxide, and mix (indicating the presence of both gases). Table S4 in the Supplementary Materials shows the obtained classification MLPs. The result of the top-performing classification MLP is depicted in Fig. 8(a) and (b), having an accuracy of around 99% for training and testing in most cases. Except when classifying nitrogen dioxide, the MLP was misclassified at 1.9% (train) and 3% (test) with air.

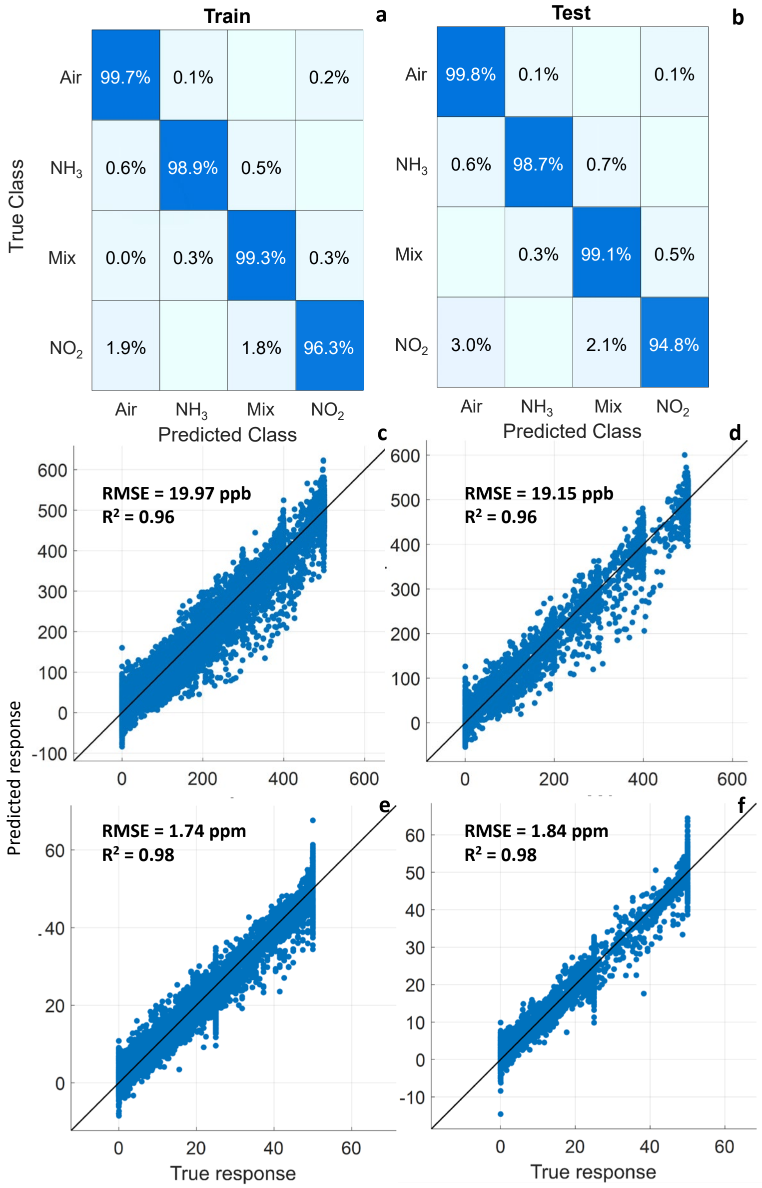

Train (a)

True Class \ Predicted Class	Air	NH_3	Mix	NO_2
Air	99.7%	0.1%		0.2%
NH_3	0.6%	98.9%	0.5%	
Mix	0.0%	0.3%	99.3%	0.3%
NO_2	1.9%		1.8%	96.3%

Test (b)

True Class \ Predicted Class	Air	NH_3	Mix	NO_2
Air	99.8%	0.1%		0.1%
NH_3	0.6%	98.7%	0.7%	
Mix		0.3%	99.1%	0.5%
NO_2	3.0%		2.1%	94.8%

Fig. 8. Confusion matrix of the classification MLP under a mixture: (a) train data and (b) test data. Results of the best MLP for nitrogen dioxide quantification under a mixture: (c) train data and (d) test data. Results of the best MLP for ammonia quantification under a mixture: (e) train data and (f) test data.

The prediction of the concentration of nitrogen dioxide during a mixture with ammonia exhibited R^2 and RMSE values of 0.96 and 19.97 ppb, respectively [see Fig. 8(c)]. Finally, for quantifying ammonia, the chosen quantification MLP demonstrates favorable performance. The R^2 coefficients stand at 0.98, while the RMSE remains below 1.74 ppm [see Fig. 8(e)]. Tables S5 and S6 in the Supplementary Materials summarize the MLPs of both gases. Fig. 8(d) and (f) shows the test results for nitrogen dioxide and ammonia, respectively.

A summary of the best-obtained classification and quantification models is displayed in Tables II and III, respectively. As noticed, the resultant architectures of the MLPs in both scenarios were the same for the classification and quantification (single layer and 100 neurons per layer). The variation occurred in the selection of the activation function. For classification was selected Tanh (see Table II), for quantifying ammonia, sigmoid, and ReLU for quantifying nitrogen dioxide (see Table III). These results are interesting since ReLU is the most popular activation function for the hidden layers and the first-to-go choice in most neural networks [57]. However, it was only the best in nitrogen dioxide quantification.

TABLE II:
SUMMARY OF CLASSIFICATION MLP

HL	**N/L**	**AF**	**Accuracy train [%]**	**Accuracy test [%]**	**Scenario**
1	100	Tanh	98.6	98.7	Low and high % RH
1	100	Tanh	99.3	99.2	Mixture of NH_3 and NO_2

TABLE III:
SUMMARY OF QUANTIFICATION MLP

Gas	**HL**	**N/L**	**AF**	**RMSE train**	**R^2 train**	**RMSE test**	**R^2 test**	**Scenario**
NO_2	1	100	ReLU	28.13 ppb	0.93	27.43 ppb	0.94	Low and high % RH
NH_3	1	100	Sigmoid	1.49 ppb	0.97	1.39 ppb	0.98	
NO_2	1	100	ReLU	19.97 ppb	0.96	19.15 ppb	0.96	Mixture of NH_3 and NO_2
NH_3	1	100	Sigmoid	1.74 ppb	0.98	1.84 ppb	0.98	

HL: number of hidden layers
N/L: number of neurons per layer
AF: activation function

On the other hand, the accuracy, RMSE, and R^2 in both scenarios have similar results. Conversely, when comparing the RMSE on the quantification of nitrogen dioxide, around 1% of the error is incremented under the variation of % RH. This could be attributed to the Graphene@ZnO sensor being more influenced by the variation of % RH than LIG@Ppy.

C. *Methodology: Recognition Stage Results*

The obtained MLPs were implemented on the UI to test the operation of the IoT platform. While receiving the data from sensors, a MATLAB script is called from Node-RED to classify and quantify the target gases. First, the script receives one by one (as parameters), the raw data from the sensors in each sample period. Furthermore, a preprocessing phase consisted of a FIFO-type buffer, which accumulates 12 values of each sensor and implements an asymmetric left windowed filter [12 0]. Then, after normalizing the values, the classification algorithm is called. Next, it is called the corresponding quantification algorithm using the best MLPs described above. Fig. S13 in the Supplementary Materials shows a screenshot of the UI. The UI has six upper charts related to the raw signal from the four chemoresistor gas sensors and the humidity and temperature sensor. The tree charts at the bottom are the classification and quantification results. Fig. S13(a) presents a 200-ppb pulse of nitrogen dioxide. Likewise, Fig. S13(b) shows a 30-ppm pulse of ammonia, recovery time, and, finally, the beginning of a 40-ppm pulse of ammonia.

In these final measurements, the resultant accuracy was 84.59%, and RMSE and R^2 were 0.97 and 2.33 ppm for ammonia, respectively, and 0.89 and 31.28 ppb for nitrogen dioxide, respectively. These values are in the range of gas-sensing applications found in the literature [58], [59]. It is important to highlight that the implemented gas detection platform improves the quantification response time versus the response time of a single sensor separately. As demonstrated by Llobet et al. [60], [61] and Vilanova et al. [62], the transient response of chemoresistor gas sensors contains relevant information that ANN models can extract. Therefore, the MLPs classify and quantify the gases while acquiring the transient response of the sensors. The MLPs do not wait until the sensors reach the steady state to show a correct output. Fig. 9 shows the details.

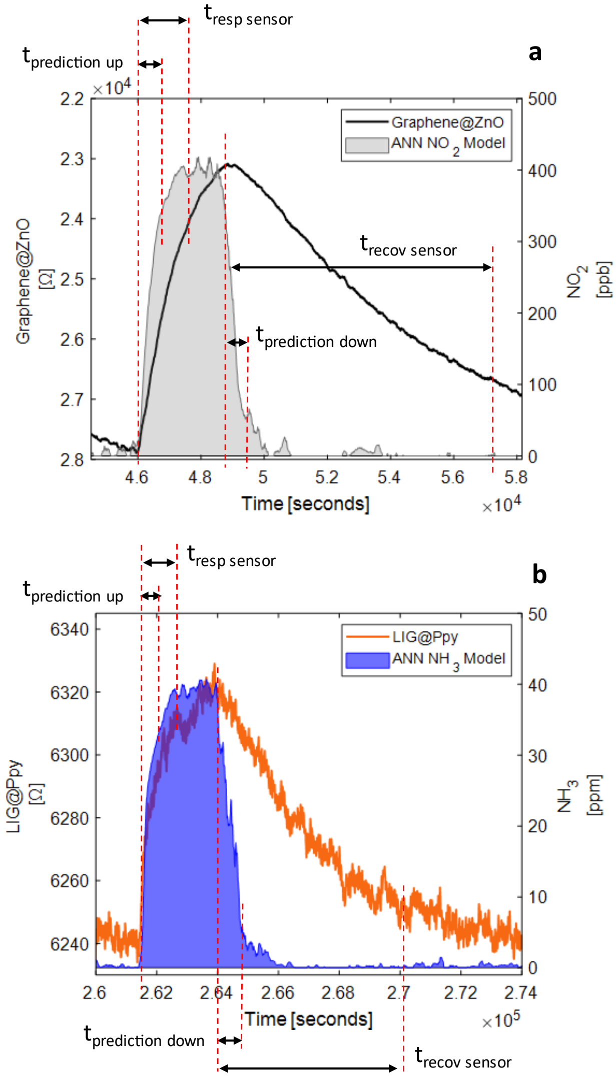

Fig. 9. Comparison of quantification response time between platform and sensor approach. (a) Nitrogen dioxide. (b) Ammonia.

The quantification response time depends on whether the sensors are reacting to the gas or recovering from the reaction. Therefore, from a single-sensor perspective, it is classified into response time ($t_{\_resp\ sensor}$) and recovery time ($t_{\_recov\ sensor}$). Similarly, from the platform perspective, it is classified into prediction-up time ($t_{\_prediciton\text{-}up}$) and prediction-down time ($t_{\_prediciton\text{-}down}$). The response time and prediction-up time are defined as the time taken to reach 90% of the full response after the exposure of the target gas. The recovery time and prediction-down time are defined as the time taken to reach 90% back of the variation between the steady-state value in the response and the baseline. Fig. 9(a) shows a qualitative comparison between the platform and single-sensor approaches. For nitrogen dioxide, $t_{\_resp\ sensor}$ is bigger than $t_{\_prediciton\text{-}up}$. Also, $t_{\_recov\ sensor}$ is bigger than $t_{\_prediciton\text{-}down}$. A similar result is found when analyzing Fig. 9(b), this time under ammonia exposure. In both cases, the comparison was performed using the selective sensor of each gas, and it was noticed that using the platform reduces the quantification and classification time by around 40% in both cases.

IV. CONCLUSION

The methodology presented in this work can be used to integrate new chemoresistor gas sensors into the GSNs, add new GSNs to the platform, and deploy the platform in different scenarios. Replacing the sensors for different ones is quickly achievable by repeating the training and recognition stages described during this work. The possibility of reusing low-cost laboratory-made chemoresistor gas sensors in application scenarios raises the versatility of this platform. Using selective sensors increases the probability of discriminating pollutants under a mixture. Furthermore, the platform reduces the classification and quantification time by around 40% (compared with the single-sensor approach). The inclusion of environmental sensors in the GSNs considerably improves the output of the classification and quantification models. As demonstrated in this work, ammonia and nitrogen dioxide were completely classified and quantified under a mixture and at different relative humidity percentages.

The platform has been successfully tested in laboratory conditions and is ready to be deployed in real-application scenarios to update and recalibrate the classification and quantification models (if required). Software and hardware were designed in layers; therefore, it is quite easy to replace the wireless physical layer to tune the platform according to the requirements of the final application. Since communication protocol is based on the MQTT, adding new nodes is as easy as configuring (by software) new topics on the new GSNs to be added. Therefore, deploying this IoT platform in a real-application scenario will be a suitable next step to continue this study.

REFERENCES

[1] P. Amoatey, H. Omidvarborna, M. S. Baawain, and A. Al-Mamun, "Emissions and exposure assessments of SOX, NOX, PM10/2.5 and trace metals from oil industries: A review study (2000–2018)," Process Safety and Environmental Protection, vol. 123, pp. 215–228, Mar. 2019, doi: 10.1016/j.psep.2019.01.014.

[2] F. M. Adebiyi, "Air quality and management in petroleum refining industry: A review," Environmental Chemistry and Ecotoxicology, vol. 4, pp. 89–96, Jan. 2022, doi: 10.1016/j.enceco.2022.02.001.

[3] I. Manisalidis, E. Stavropoulou, A. Stavropoulos, and E. Bezirtzoglou, "Environmental and Health Impacts of Air Pollution: A Review," Front Public Health, vol. 8, p. 505570, Feb. 2020, doi: 10.3389/fpubh.2020.00014.

[4] J. González-Martín, N. J. R. Kraakman, C. Pérez, R. Lebrero, and R. Muñoz, "A state–of–the-art review on indoor air pollution and strategies for indoor air pollution control," Chemosphere, vol. 262, p. 128376, Jan. 2021, doi: 10.1016/j.chemosphere.2020.128376.

[5] Z. Idrees and L. Zheng, "Low cost air pollution monitoring systems: A review of protocols and enabling technologies," J Ind Inf Integr, vol. 17, p. 100123, Mar. 2020, doi: 10.1016/j.jii.2019.100123.

[6] D. Kwak, Y. Lei, and R. Maric, "Ammonia gas sensors: A comprehensive review," Talanta, vol. 204, pp. 713–730, Nov. 2019, doi: 10.1016/J.TALANTA.2019.06.034.

[7] Z. Yunusa, M. N. Hamidon, A. Kaiser, and Z. Awang, "Gas Sensors- A Review," Journal of Environmental Nanotechnology, vol. 4, no. 4, pp. 01–14, Dec. 2015, doi: 10.13074/jent.2015.12.153163.

[8] S. Hong et al., "FET-type gas sensors: A review," Sens Actuators B Chem, vol. 330, p. 129240, Mar. 2021, doi: 10.1016/j.snb.2020.129240.

[9] J. Li, H. Yan, H. Dang, and F. Meng, "Structure design and application of hollow core microstructured optical fiber gas sensor: A review," Opt Laser Technol, vol. 135, p. 106658, Mar. 2021, doi: 10.1016/j.optlastec.2020.106658.

[10] D. E. Williams, "Electrochemical sensors for environmental gas analysis," Curr Opin Electrochem, vol. 22, pp. 145–153, Aug. 2020, doi: 10.1016/j.coelec.2020.06.006.

[11] M. L. Grilli, "Metal Oxides," Metals (Basel), vol. 10, no. 6, p. 820, Jun. 2020, doi: 10.3390/met10060820.

[12] R. J. Rath, S. Farajikhah, F. Oveissi, F. Dehghani, and S. Naficy, "Chemiresistive Sensor Arrays for Gas/Volatile Organic Compounds Monitoring: A Review," Adv Eng Mater, vol. 25, no. 3, p. 2200830, Feb. 2023, doi: 10.1002/adem.202200830.

[13] Y.-F. Sun et al., "Metal Oxide Nanostructures and Their Gas Sensing Properties: A Review," Sensors, vol. 12, no. 3, pp. 2610–2631, Feb. 2012, doi: 10.3390/s120302610.

[14] D. Sales-Lérida, A. J. Bello, A. Sánchez-Alzola, and P. M. Martínez-Jiménez, "An Approximation for Metal-Oxide Sensor Calibration for Air Quality Monitoring Using Multivariable Statistical Analysis," Sensors, vol. 21, no. 14, p. 4781, Jul. 2021, doi: 10.3390/s21144781.

[15] D. Sun, Y. Luo, M. Debliquy, and C. Zhang, "Graphene-enhanced metal oxide gas sensors at room temperature: a review," Beilstein Journal of Nanotechnology, vol. 9, no. 1, pp. 2832–2844, Nov. 2018, doi: 10.3762/bjnano.9.264.

[16] X. Tang, M. Debliquy, D. Lahem, Y. Yan, and J.-P. Raskin, “A Review on Functionalized Graphene Sensors for Detection of Ammonia,” Sensors, vol. 21, no. 4, p. 1443, Feb. 2021, doi: 10.3390/s21041443.

[17] Y. C. Wong, B. C. Ang, A. S. M. A. Haseeb, A. A. Baharuddin, and Y. H. Wong, “Review—Conducting Polymers as Chemiresistive Gas Sensing Materials: A Review,” J Electrochem Soc, vol. 167, no. 3, p. 037503, Sep. 2020, doi: 10.1149/2.0032003JES/XML.

[18] J. Pan et al., “Lightweight Neural Network for Gas Identification Based on Semiconductor Sensor,” IEEE Trans Instrum Meas, vol. 71, pp. 1–8, 2022, doi: 10.1109/TIM.2021.3135503.

[19] L. Zhao, F. Tian, J. Qian, H. Li, and Z. Wu, “Feature Ensemble Learning for Sensor Array Data Classification Under Low-Concentration Gas,” IEEE Trans Instrum Meas, vol. 72, pp. 1–9, 2023, doi: 10.1109/TIM.2023.3251416.

[20] U. Yaqoob and M. I. Younis, “Chemical Gas Sensors: Recent Developments, Challenges, and the Potential of Machine Learning—A Review,” Sensors, vol. 21, no. 8, p. 2877, Apr. 2021, doi: 10.3390/s21082877.

[21] M. A. H. Khan, B. Thomson, R. Debnath, A. Motayed, and M. V. Rao, “Nanowire-Based Sensor Array for Detection of Cross-Sensitive Gases Using PCA and Machine Learning Algorithms,” IEEE Sens J, vol. 20, no. 11, pp. 6020–6028, Jun. 2020, doi: 10.1109/JSEN.2020.2972542.

[22] Z. Ye, Y. Liu, and Q. Li, “Recent Progress in Smart Electronic Nose Technologies Enabled with Machine Learning Methods,” Sensors, vol. 21, no. 22, p. 7620, Nov. 2021, doi: 10.3390/s21227620.

[23] H. Chen, D. Huo, and J. Zhang, “Gas Recognition in E-Nose System: A Review,” IEEE Trans Biomed Circuits Syst, vol. 16, no. 2, pp. 169–184, Apr. 2022, doi: 10.1109/TBCAS.2022.3166530.

[24] N. Ha, K. Xu, G. Ren, A. Mitchell, and J. Z. Ou, "Machine Learning-Enabled Smart Sensor Systems," Advanced Intelligent Systems, vol. 2, no. 9, p. 2000063, Sep. 2020, doi: 10.1002/aisy.202000063.

[25] J. Chu et al., "Identification of gas mixtures via sensor array combining with neural networks," Sens Actuators B Chem, vol. 329, p. 129090, Feb. 2021, doi: 10.1016/j.snb.2020.129090.

[26] J.-Y. Kim, S. P. Bharath, A. Mirzaei, S. S. Kim, and H. W. Kim, "Identification of gas mixtures using gold-decorated metal oxide based sensor arrays and neural networks," Sens Actuators B Chem, vol. 386, p. 133767, Jul. 2023, doi: 10.1016/j.snb.2023.133767.

[27] J. Zhang et al., "A miniaturized electronic nose with artificial neural network for anti-interference detection of mixed indoor hazardous gases," Sens Actuators B Chem, vol. 326, p. 128822, Jan. 2021, doi: 10.1016/j.snb.2020.128822.

[28] M.-L. Cao, Q.-H. Meng, Y.-Q. Jing, J.-Y. Wang, and M. Zeng, "Distributed Sequential Location Estimation of a Gas Source via Convex Combination in WSNs," IEEE Trans Instrum Meas, vol. 65, no. 6, pp. 1484–1494, Jun. 2016, doi: 10.1109/TIM.2016.2518358.

[29] S. Ali, T. Glass, B. Parr, J. Potgieter, and F. Alam, "Low Cost Sensor With IoT LoRaWAN Connectivity and Machine Learning-Based Calibration for Air Pollution Monitoring," IEEE Trans Instrum Meas, vol. 70, pp. 1–11, 2021, doi: 10.1109/TIM.2020.3034109.

[30] S. C. Folea and G. D. Mois, "Lessons Learned From the Development of Wireless Environmental Sensors," IEEE Trans Instrum Meas, vol. 69, no. 6, pp. 3470–3480, Jun. 2020, doi: 10.1109/TIM.2019.2938137.

[31] M. A. Alouani et al., "ZnO-Loaded Graphene for NO_2 Gas Sensing," Sensors, vol. 23, no. 13, p. 6055, Jun. 2023, doi: 10.3390/s23136055.

[32] A. Santos-Betancourt et al., “ZnO Decorated Graphene-Based NFC Tag for Personal NO2 Exposure Monitoring during a Workday,” Sensors, vol. 24, no. 5, p. 1431, Feb. 2024, doi: 10.3390/s24051431.

[33] J. C. Santos-Ceballos, F. Salehnia, A. Romero, and X. Vilanova, “Flexible Sensor Utilizing Polypyrrole Laser-Induced Graphene Nanocomposite for Room Temperature Ammonia Detection,” in 2023 IEEE SENSORS, IEEE, Oct. 2023, pp. 01–04. doi: 10.1109/SENSORS56945.2023.10325068.

[34] J. C. Santos-Ceballos, F. Salehnia, A. Romero, X. Vilanova, and E. Llobet, “Low Cost, Flexible, Room Temperature Gas Sensor: Polypyrrole-Modified Laser-Induced Graphene for Ammonia Detection,” IEEE Sens J, vol. 24, no. 7, pp. 9366–9374, Apr. 2024, doi: 10.1109/JSEN.2024.3368658.

[35] E. Navarrete, C. Bittencourt, P. Umek, and E. Llobet, “AACVD and gas sensing properties of nickel oxide nanoparticle decorated tungsten oxide nanowires,” J Mater Chem C Mater, vol. 6, no. 19, pp. 5181–5192, May 2018, doi: 10.1039/C8TC00571K.

[36] È. Navarrete et al., “WO_3 nanowires loaded with cobalt oxide nanoparticles, deposited by a two-step AACVD for gas sensing applications,” Sens Actuators B Chem, vol. 298, p. 126868, Nov. 2019, doi: 10.1016/j.snb.2019.126868.

[37] N. Anderson, R. Strader, and C. Davidson, “Airborne reduced nitrogen: ammonia emissions from agriculture and other sources,” Environ Int, vol. 29, no. 2–3, pp. 277–286, Jun. 2003, doi: 10.1016/S0160-4120(02)00186-1.

[38] P. Xu et al., “An inventory of the emission of ammonia from agricultural fertilizer application in China for 2010 and its high-resolution spatial distribution,” Atmos Environ, vol. 115, pp. 141–148, Aug. 2015, doi: 10.1016/j.atmosenv.2015.05.020.

[39] C. Ti, L. Xia, S. X. Chang, and X. Yan, “Potential for mitigating global agricultural ammonia emission: A meta-analysis,”

Environmental Pollution, vol. 245, pp. 141–148, Feb. 2019, doi: 10.1016/j.envpol.2018.10.124.

[40] R. J. Wild et al., “On-road measurements of vehicle NO_2 /NOx emission ratios in Denver, Colorado, USA,” Atmos Environ, vol. 148, pp. 182–189, Jan. 2017, doi: 10.1016/j.atmosenv.2016.10.039.

[41] P. Castellanos and K. F. Boersma, “Reductions in nitrogen oxides over Europe driven by environmental policy and economic recession,” Sci Rep, vol. 2, no. 1, p. 265, Feb. 2012, doi: 10.1038/srep00265.

[42] S. N. Behera, M. Sharma, V. P. Aneja, and R. Balasubramanian, “Ammonia in the atmosphere: a review on emission sources, atmospheric chemistry and deposition on terrestrial bodies,” Environmental Science and Pollution Research, vol. 20, no. 11, pp. 8092–8131, Nov. 2013, doi: 10.1007/s11356-013-2051-9.

[43] J. N. Cape, Y. S. Tang, N. van Dijk, L. Love, M. A. Sutton, and S. C. F. Palmer, “Concentrations of ammonia and nitrogen dioxide at roadside verges, and their contribution to nitrogen deposition,” Environmental Pollution, vol. 132, no. 3, pp. 469–478, Dec. 2004, doi: 10.1016/j.envpol.2004.05.009.

[44] “Air quality, energy and health.” Accessed: Apr. 16, 2024. [Online]. Available: https://www.who.int/teams/environment-climate-change-and-health/air-quality-and-health/health-impacts/types-of-pollutants

[45] “Basic Information about NO_2 | US EPA.” Accessed: Apr. 16, 2024. [Online]. Available: https://www.epa.gov/no2-pollution/basic-information-about-no2

[46] K. E. Wyer, D. B. Kelleghan, V. Blanes-Vidal, G. Schauberger, and T. P. Curran, “Ammonia emissions from agriculture and their contribution to fine particulate matter: A review of implications for human health,” J Environ Manage, vol. 323, p. 116285, Dec. 2022, doi: 10.1016/j.jenvman.2022.116285.

[47] Z. Song et al., “Wireless Self-Powered High-Performance Integrated Nanostructured-Gas-Sensor Network for Future Smart Homes,” ACS Nano, vol. 15, no. 4, pp. 7659–7667, Apr. 2021, doi: 10.1021/acsnano.1c01256.

[48] S. Nath, A. Dey, P. Pachal, J. K. Sing, and S. K. Sarkar, “Performance analysis of gas sensing device and corresponding IoT framework in mines,” Microsystem Technologies, vol. 27, no. 11, pp. 3977–3985, Nov. 2021, doi: 10.1007/s00542-019-04621-x.

[49] C. Seok, M. M. Mahmud, M. Kumar, O. J. Adelegan, F. Y. Yamaner, and O. Oralkan, “A Low-Power Wireless Multichannel Gas Sensing System Based on a Capacitive Micromachined Ultrasonic Transducer (CMUT) Array,” IEEE Internet Things J, vol. 6, no. 1, pp. 831–843, Feb. 2019, doi: 10.1109/JIOT.2018.2861330.

[50] W. Dargie, J. Wen, L. A. Panes-Ruiz, L. Riemenschneider, B. Ibarlucea, and G. Cuniberti, “Monitoring Toxic Gases Using Nanotechnology and Wireless Sensor Networks,” IEEE Sens J, vol. 23, no. 11, pp. 12274–12283, Jun. 2023, doi: 10.1109/JSEN.2023.3269723.

[51] J.-H. Suh et al., “Fully integrated and portable semiconductor-type multi-gas sensing module for IoT applications,” Sens Actuators B Chem, vol. 265, pp. 660–667, Jul. 2018, doi: 10.1016/j.snb.2018.03.099.

[52] H. Meixner and U. Lampe, “Metal oxide sensors,” Sens Actuators B Chem, vol. 33, no. 1–3, pp. 198–202, Jul. 1996, doi: 10.1016/0925-4005(96)80098-0.

[53] J. Zhang, X. Liu, G. Neri, and N. Pinna, “Nanostructured Materials for Room-Temperature Gas Sensors,” Advanced Materials, vol. 28, no. 5, pp. 795–831, Feb. 2016, doi: 10.1002/adma.201503825.

[54] R. Inglés, J. Pallarés, J. L. Ramírez, “Improving sample flow in planar preconcentrator.” in International Conference on Computational and Mathematical Methods in Science and Engineering, Almería, Spain, Jun. 2010.

[55] K. Ogata, “Control Systems Analysis in State Space,” Modern Control Engineering, 2010.

[56] D. Laussmann and D. Helm, “Air Change Measurements Using Tracer Gases: Methods and Results. Significance of air change for indoor air quality,” in Chemistry, Emission Control, Radioactive Pollution and Indoor Air Quality, InTech, 2011. doi: 10.5772/18600.

[57] T. Szandała, “Review and comparison of commonly used activation functions for deep neural networks,” Studies in Computational Intelligence, vol. 903, pp. 203–224, 2021, doi: 10.1007/978-981-15-5495-7.

[58] Y. Zhao, H.-Y. Li, and J. Liu, “Review-Modern Data Analysis in Gas Sensors” 2022, doi: 10.1149/1945-7111/aca839.

[59] V. G. Nath, S. P. Bharath, A. Dsouza, and A. Subramanian, “Machine Learning Algorithms for Smart Gas Sensor Arrays,” Advanced Structured Materials, vol. 213, pp. 185–225, 2024, doi: 10.1007/978-981-97-1390-5_8.

[60] E. Llobet, J. Brezmes, X. Vilanova, J. E. Sueiras, and X. Correig, “Qualitative and quantitative analysis of volatile organic compounds using transient and steady-state responses of a thick-film tin oxide gas sensor array,” Sens Actuators B Chem, vol. 41, no. 1–3, pp. 13–21, Jun. 1997, doi: 10.1016/S0925-4005(97)80272-9.

[61] E. Llobet, X. Vilanova, J. Brezmes, J. E. Sueiras, and X. Correig, “Transient response of thick-film tin oxide gas-sensors to multicomponent gas mixtures,” Sens Actuators B Chem, vol. 47, no. 1–3, pp. 104–112, Apr. 1998, doi: 10.1016/S0925-4005(98)00009-4.

[62] X. Vilanova, E. Llobet, R. Alcubilla, J. E. Sueiras, and X. Correig, “Analysis of the conductance transient in thick-film tin oxide gas sensors,” Sens Actuators B Chem, vol. 31, no. 3, pp. 175–180, Mar. 1996, doi: 10.1016/0925-4005(96)80063-3.

Chapter 4

Design of a wearable device on low-cost flexible support for gas sensing applications

The following chapter presents the design of a wearable device on low-cost flexible support for gas sensing applications. It presents the fabrication of graphene-based sensors incorporating IDEs in the same flexible printed circuit board as the electronics. In this chapter, a cumulative near-field communication (NFC) wearable for NO_2 sensing applications is fabricated. The obtained wearable device can be easily attached to a working vest allowing simple integration in any working environment.

This design is presented in Section 4.1, through a published paper named "ZnO Decorated Graphene-Based NFC Tag for Personal NO_2 Exposure Monitoring during a Workday".

Section 4.1

ZnO Decorated Graphene-Based NFC Tag for Personal NO_2 Exposure Monitoring during a Workday

Alejandro Santos-Betancourt, José Carlos Santos-Ceballos, Mohamed Ayoub Alouani, Shuja Bashir Malik, Alfonso Romero, José Luis Ramírez, Xavier Vilanova, and Eduard Llobet

Sensors, February 2024, Vol. 24, Issue 5, 1431

DOI: https://doi.org/10.3390/s24051431

Abstract

This paper presents the integration of a sensing layer over interdigitated electrodes and an electronic circuit on the same flexible printed circuit board. This integration provides an effective technique to use this design as a wearable gas measuring system in a target application, exhibiting high performance, low power consumption, and being lightweight for on-site monitoring. The wearable system proves the concept of using an NFC tag combined with a chemoresistive gas sensor as a cumulative gas sensor, having the possibility of holding the data for a working day, and completely capturing the exposure of a person to NO_2 concentrations. Three different types of sensors were tested, depositing the sensing layers on gold electrodes over Kapton substrate: bare graphene, graphene decorated with 5 wt.% zinc oxide nanoflowers, or nanopillars. The deposited layers were characterized using FESEM, EDX, XRD, and Raman spectroscopy to determine their crystalline structure, morphological and chemical compositions. The gas sensing performance of the sensors was analyzed against NO_2 (dry and humid conditions) and other interfering species (dry conditions) to check their sensitivity and selectivity. The resultant-built wearable NFC tag system accumulates the data in a non-volatile memory every minute and has an average low power consumption of 24.9 μW in dynamic operation. Also, it can be easily attached to a work vest.

Keywords

wearable NFC tag system; NO_2 gas sensor; working-day; metal oxide; graphene.

1. Introduction

Nitrogen dioxide (NO_2) is a highly toxic gas that is found in outdoor air pollution but can also be found in indoor scenarios such as renovation or construction activities when using certain paints, adhesives or solvents, smoking areas, parking garages, and industrial facilities, among others [**1**]. NO_2 is known to harm the human respiratory system. This pollutant gas can irritate airways and provoke respiratory diseases such as asthma, pharyngitis, and bronchitis [**2**,**3**]. Particularly, a lot of work positions around the world have a risk of exposing workers to this toxic gas, and studies have been conducted on this topic. U. Carbone et al. [**4**] concluded that occupational exposure to NO_2 emissions in power plants is significantly associated with lung function abnormalities. N. Plato et al. [**5**] conducted a study to detect particles and NO_2 exposure in workers inside the underground train system in Stockholm and classified the workers according to the level of exposure. Salonen H. et al. [**6**] determined that workers in places like schools and indoor offices have a risk of exposure to NO_2, mostly in the winter season. Dahmann D. et al., and Kurnia J.C. et al., agreed that workers from underground mining and tunneling need to give special attention to the level of pollutants in the atmosphere, especially NO_2 [**7**,**8**]. According to the European Chemical Agency (ECHA), the Occupational Exposure Limits (OELs) in a Long-Term Period Limit (LTEL) are equal to 0.5 ppm, and the OELs in a Short-Term Period Limit (STEL) are equal to 1 ppm [**9**]. Additionally, this contaminant gas is also dangerous to the global ecosystem and the environment, since it has adverse effects on water, soil, and the atmosphere [**10**]. Therefore, monitoring NO_2 is a crucial issue for environmental and human well-being, and numerous types of sensors have emerged in recent years [**11**,**12**].

Chemoresistive sensors have become an attractive gas monitoring option due to their easy fabrication, miniaturization, and low production cost [**13**,**14**]. They consist of a sensitive layer placed between two electrodes, which enables measuring the variation in electrical conductivity when reacting to specific gases [**15**]. Some of the most widely known and used nanomaterials for the growth of the active layer are metal oxides (MOXs) [**16**]. MOXs have some advantages, like their small size, low manufacturing cost, simple read-out-chain design, and short response time when reacting to a chemical analyte [**17**,**18**]. But also, despite being useful and effective for a long period, they have several disadvantages, such as poor selectivity, baseline drift, high sensitivity to humidity, and high power consumption since they usually work at high temperatures [**19**,**20**]. In recent years, graphene-based materials have risen due to their excellent sensing properties [**21**,**22**]. The combination of graphene with different MOXs has also been studied to increase the selectivity, improve the baseline recovery, shorten the recovery time, and decrease the power consumption as they could work at room temperature [23,24]. Table S1 in the Supplementary Materials, presents a comparison of graphene-based gas sensors for NO_2 detection at room temperature. To prove the feasibility of the wearable NFC tag system developed during this work, graphene decorated with 5 wt.% zinc oxide (ZnO) was used due to the previous experience of our research group working with a combination of these materials [25]. The authors compared different wt.% ZnO loading on a graphene-based sensor and concluded that the 5 wt.% loading performs better than higher and lower loadings according to sensing capabilities toward NO_2 concentrations.

Since wearable devices must have specific features such as lightweight, wireless connectivity, and low power consumption, building a gas sensor as a wearable device is a substantial challenge [26,27,28]. Nonetheless, plenty of wearable gas sensors and healthcare wearable systems have been recently developed [29]. Chen et al., demonstrated a Bluetooth wearable NO_2 sensor based on zinc sulfide nanoparticles/nitrogen-doped reduced graphene oxide [30]. Also, a flexible gas early warning module was proposed and designed by Zhang et al., based on flexible electronic technology [31]. Likewise, a highly flexible epidermal design and clinical implementation of a novel ECG and heart-rate logging wearable sensor were presented by Lee et al. [32]. Moreover, Lin et al. [33] reported the integration of NFC functionality into textiles and demonstrated continuous physiological monitoring of the spinal posture. All these wearable devices use several wireless communication technologies to send the data from sensors to the final user interface or a database for further processing. These wireless technologies employ Bluetooth, Ultra-High Frequency Radio Frequency Identification (UHF RFID), and Near Field Communication (NFC). They have several advantages and disadvantages, regardless of power consumption, communication range, and price [34,35]. In recent years, the integration of NFC technology with low-cost electronics and sensors has facilitated a variety of new sensing applications [35]. A study of a wearable carbon dioxide sensor was reported by Escobedo et al. [36], describing the performance of a wearable NFC tag to be used for non-invasive gas determination. Zhang et al. [37] reported a flexible

NFC system based on an ammonia sensor using reduced graphene oxide decorated with silver nanoparticles, which sense low concentrations (5 ppm) at room temperature. Likewise, Escobedo et al. [**38**] presented a full-passive flexible multi-gas sensing tag for determining oxygen, carbon dioxide, ammonia, and relative humidity readable by a smartphone through NFC technology. Moreover, wireless, passive, flexible, and low-cost NFC tag sensors based on commercial NFC tags for biochemical sensing were demonstrated by Xu et al. [**39**]. Additionally, Salehnia F. et al. [**40**] discuss the development of a battery-free NFC sub-ppm gas sensor for distributed gas monitoring applications, using a laser-induced graphene (LIG) sensor for NO_2 detection. The use of NFC technology in the aforementioned studies has advantages, such as the fact that the systems can be used without batteries, harvesting energy from the NFC field. Nevertheless, this is also a disadvantage since the systems cannot acquire historical data from the sensor for a long period of time. They only obtain the specific value of the sensor data when the NFC tag is near the NFC reader or when they have sufficient energy in the harvest-storage element. **Table S2 in the Supplementary Materials**, presents a comparison of the wearable NFC gas sensors on a flexible substrate.

To overcome this challenge, we demonstrate for the first time in this paper the fabrication of a wearable cumulative battery-operated gas sensor based on bare graphene (BG) decorated with 5 wt.% ZnO nanoflowers (NF) and nanopillars (NP) for on-site NO_2 monitoring. The communication stage between the wearable system and the reader is conducted through NFC technology, and the cumulated data can be monitored on a smartphone (an NFC reader) using a custom-made test application. This wearable NFC tag system was built to prove the concept of being used in a target application in which human resources could be exposed to NO_2 concentrations during working hours. This small wearable system is easy to integrate into a working vest. Using it, a worker could easily read the data from sensors with a smartphone and obtain the gas exposure for a whole working-day period. It is worth mentioning that the scalability of this system could be as high as the software solution running on the smartphone. Moreover, since this procedure could also be used with different sensing materials, we believe these results will provide a new perspective on wearables for the on-site monitoring, recording, and analysis of threatening gases.

2. Experimental

2.1. Wearable NFC Tag System Preparation

Figure 1a presents a description of the fabrication process of the wearable NFC tag system. First, the synthesis of the nanoparticles was performed. A hydrothermal method was used to synthesize ZnO nanoparticles. A total of 70 mg of zinc acetate dihydrate ($Zn(CH_3COO)_2 \cdot 2H_2O$) (Sigma Aldrich, St. Louis, MO, USA, CAS: 5970-45-6) and 40 mg of citric acid ($C_6H_8O_7$) (Sigma Aldrich, CAS: 77-92-9) were dissolved in a mixture of deionized water (67 mL) and ethanol (13 mL) under vigorous stirring. A total of 10 M sodium hydroxide (NaOH) (Sigma Aldrich, CAS: 1310-73-2) was dropped into the stirring solution until the pH reached 11. The solution turns hazy white after the addition of NaOH. After 4 h of continuous stirring, the solution turns milky. The solution was then transferred to a 100 mL capacity autoclave with a Teflon liner. The autoclave was heated at 150 °C with a ramp-up temperature of 10 °C per minute for 20 h for NF synthesis and 17 h for NP synthesis. The autoclave was allowed to cool naturally to room temperature. The solution was centrifuged to obtain the white precipitate, thoroughly washed with deionized water and ethanol several times, and dried at 80 °C overnight. The nanomaterials were annealed at 500 °C for 2 h under a synthetic air environment in a muffle furnace (Carbolite CWF 1200, Carbolite Gero Ltd., Neuhausen, Germany) before mixing with graphene.

The next step was the preparation of the ZnO-graphene hybrid/composite using commercial graphene nanoplates (Strem Chemicals, Newburyport, MA, USA). The nanoplates were mixed with the previously prepared ZnO nanoparticles to make two different powders, one with 5 wt.% of NF and the second with 5 wt.% of NP. The mixing process was simple and low-cost, where the previously obtained powders were dissolved in ethanol (Scharlab, Sentmenat, Spain, CAS: 64-17-5) and put under magnetic stirring for 30 min. Later, the two different solutions were filtered using filter paper. Afterward, the mixed powders were treated under a microwave at a power of 1000 W for about 5 min. Solutions of 10 mL of Ethanol mixed with 1 mg of graphene powder (decorated or pristine) under magnetic stirring for half an hour were prepared to be airbrushed onto the gold electrodes.

Simultaneously, a third step was focused on the electronic design using a free license for non-commercial use and evaluation purposes of Autodesk Eagle version 9.6.2. Then, the final flexible printed circuit board (FPCB) was fabricated (JLCPCB, Shenzhen, China). Afterward, components were populated on the board, and the programming and debugging of the firmware were performed using the MCUXpresso Integrated Development Environment v11.7.1_9221 from NXP Semiconductor. Finally, the solutions were airbrushed on top of the interdigitated electrodes (IDEs) using a DISMOER airbrush tool. **Figure 1**b shows the obtained wearable NFC tag system.

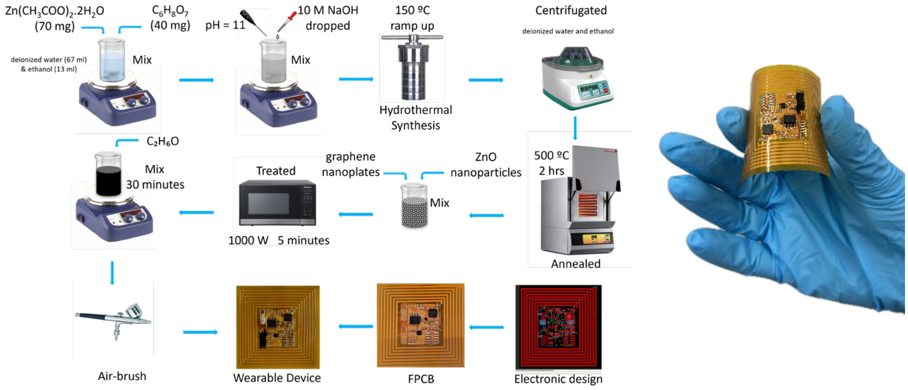

(**a**) (**b**)

Figure 1. (a) Schematic description of the synthesis of zinc oxide nanoflowers and nanopillars, preparation of graphene ZnO composite, electronics design/assembling process, and air-brush process. (b) Picture of the wearable NFC tag system.

2.2. Electronic and Firmware Design

The FPCB was designed in an area equal to 45 × 45 mm^2. It was divided into four main parts: First, an NFC-dedicated System on Chip (SoC) with an ARM Cortex-M0+ microcontroller controls the electronic board. Features such as an ultra-low-power Real Time Clock (RTC) and a 4 kB

EEPROM memory were suitable to swap the system between power modes and to store samples from a 12-bit successive-approximation charge-redistribution analog to digital converter (ADC).

Second, the rest of the electronics is integrated by a DC-DC converter, which aims for the proper stabilization of 3 V across the board, suppressing the voltage variation of the battery when current consumption changes. Additionally, the DC-DC converter has a shutdown feature permitting the possibility of hard-shutdowning the whole board. Also, the electronic is integrated into the analog front end with an operational amplifier and a resistor to bias the sensor.

The third main part is a pair of IDEs to be coated with gas-sensitive layers. The IDEs have 5 pairs of fingers; the width and gap distance between them are equal to 300 μm, and the length is equal to 1.90 mm. Fourth, the NFC antenna was designed following the recommendations of a series of application notes and using the online NFC Antenna Design Tool from NXP Semiconductors [**41**]. As a result, the antenna dimensions: length and width were set to 43 mm, and the number of turns was set to 7. The copper antenna conductor has a width of 1 mm, a spacing of 0.5 mm, and a thickness of 0.1 μm. The substrate thickness is 0.11 μm, and the relative electrical permittivity of Kapton is equal to 3.2. The resultant antenna has an inductance value of 2.62 μH at 13.56 MHz.

Figure 2a presents the schematic design of the board. The SoC NHS3152 from NXP Semiconductor runs custom-made software that controls the rest of the electronics. Once the board is powered on, the NHS makes sure that the DC-DC converter, NCP705, is turned off and goes to the Deep Power Down Mode (DPDM). This action ensures that all the hardware is off, except for the Power Management Unit (PMU) and the RTC. Also, all digital functional pins are tri-stated except for the reset pin. Before entering this mode, the wake-up sources of the SoC need to be correctly configured.

In this design, there are two possible ways; **Figure 2**b shows the details. The first one is related to acquiring the data from the sensor. Using the RTC, a scheduled wake-up task is performed every 60 s. The SoC is woken up, initializes the necessary peripherals, and enables the DC-DC converter to power the analog channel. The channel is based on an operational amplifier, TSZ122, in a voltage follower configuration to avoid the current leak of the sensor when biased. In this manner, placing the rightful value of the bias resistance ensured a voltage variation that covered the full range of the ADC (0 V–1.6 V). Afterward, an analog-to-digital conversion is conducted, a conditioning of the signal is performed using a windowed filter, and the data is stored inside a non-volatile memory, EEPROM. Then, after de-initializing all the peripherals and disabling the DC-DC converter, the system goes to DPDM again. This procedure takes less than 80 ms, and the peak power consumption during the acquisition is about 1.5 mW, as shown in **Figure 2**c. It is important to notice that this fast reading-sensor procedure can be achieved because the sensor does not need a warm-up time to be read.

The second way to wake up the board is related to NFC field detection. This event occurs every time an NFC reader reads the data. Subsequently, right after the initialization of the peripherals, the data is read from the EEPROM memory and retained in the NFC shared memory to be sent to the NFC reader. This time, the rest of the electronics are kept in off mode, so the average power consumption is lower (1.25 mW) than the wake-up process explained before but takes around 2 s.

Finally, when the reader is not nearby, the board goes to DPDM again, and then the power consumption of the whole hardware is the lowest, around 3 μW. The power consumption test was performed using the Keysight B2902A Precision Source/Measure Unit (**Figure S1 in the Supplementary Materials** shows the details). The wearable NFC tag system shows an average power consumption of 24.9 μW, which is suitable to be used with low-capacity coin cell batteries and, therefore, low weight. (Ex: using a battery CR2032 (Capacity: 210 mAh), the system would theoretically work for more than one year and weigh less than 5 g).

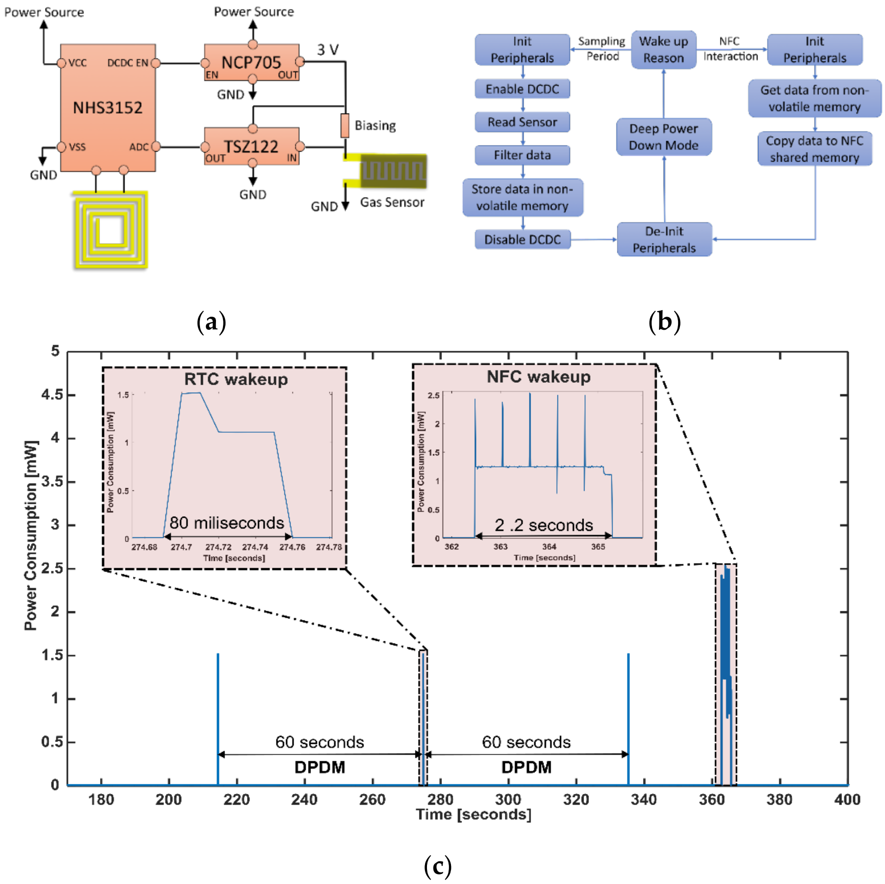

Figure 2. (**a**) Schematic design of the wearable NFC tag system. (**b**) Software interaction diagram. (**c**) Power consumption of the wearable NFC tag system during DPDM, wake-up process every 60 s to acquire the data from the sensor, and one NFC read interaction.

2.3. Active Layer Characterization

The X-ray diffraction (XRD) measurement was performed using a D8-Discovery LYNXEYE-XE-T diffractometer, configured in conventional analytical conditions. The angular 2θ diffraction ranged from 15 to 80 degrees. The collection of the data was performed with an angular step of 0.05 degrees at 0.5 s per step and sample rotation. CuKα radiation was obtained from a copper X-ray tube operated at 40 kV and 40 mA. Divergence slit 0.5 mm, anti-scatter slit 5.13, primary and secondary Soller 2.5 degrees, detector opening 2.94 degrees, air-scatter in automatic configuration, and default program settings. Also, a Field

Emission Scanning Electron Microscope (FESEM) Scios 2 DualBeam was used to study surface morphology and check the NP and NF distributions on the graphene layer. Sample characterization was performed at a high vacuum, and the electron acceleration voltage was established between 2 and 5 kV. The energy-dispersive X-ray (EDX) incorporated in the FESEM Scios was used to check the chemical composition of the active layer.

A Raman spectrometer (Renishaw, plc., Wotton-under-Edge, UK) utilizing a coupled confocal microscope (Leica DM2500 Microsystems, Leica Microsystems GmbH, Wetzlar, Germany) with a laser wavelength of 785 nm was used to check the structural fingerprint by vibrational modes of the molecules. To determine the surface area of the nanomaterials, the Brunauer–Emmett–Teller (BET) nitrogen adsorption–desorption isotherms of the ZnO nanostructures were measured from the Quantachrome Instrument: QuadraSorb Station 3 (Quantachrome Instrument, Boynton Beach, FL, USA). Samples were outgassed at 100 °C for 5 h, and the bath temperature was 77.3 K.

2.4. Gas Measurement System

The gas-sensing characteristics of the materials were determined using the system illustrated in **Figure 3**. The gas measurement system consists of different gas bottles with calibrated gas concentrations balanced in dry air, a carrier gas with zero-grade dry air, and an airtight Teflon® chamber with an inner volume of 25.85 cm^3. The gases were delivered into the chamber through a computer-controlled mass-flow system to ensure the reproducibility of the concentrations and a constant low flow of 100 mL/min. The mass-flows are controlled by software named Flow Plot v3.34, running on a Windows-based computer. To fix the sensors inside the chamber, the electrodes were separated from the rest of the electronics using a cutter.

Afterwards, the three different materials were air-brushed as explained in **Section 2.1** and carefully soldered using an SMD4300AX10 solder paste to a support that fits into the chamber connector. In that manner, the three gas sensors (one of each material: NP, NF, and BG) were put inside the chamber and left under dry synthetic air for a long period to have a stable baseline resistance. Pulses of NO_2 gas were injected into the chamber with different concentrations ranging from 50 ppb to 1 ppm, as follows: 50 ppb, 250 ppb, 500 ppb, 750 ppb, and 1 ppm; dry air was supplied in between the gas pulses to recover the baseline and keep the constant flow.

All the measurements were performed at room temperature, and the gas exposure time was 35 min and the recovery dry airtime was 70 min for each pulse. This cycle of pulses was repeated 4 times, with 2 h of recovery time between cycles. The sensor resistance was measured and stored employing an Agilent 34972A multimeter (Keysight, Santa Rosa, CA, USA) and software from Agilent Technologies Bench Link Datalogger 3 running on the same computer mentioned before.

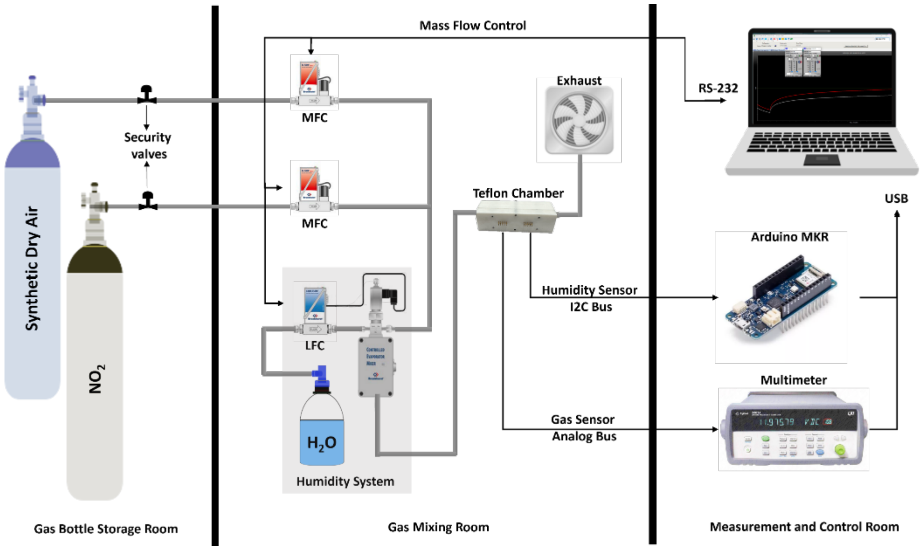

Figure 3. Schematic of the gas measurement system.

The humidity effect on the sensing performance was evaluated by humidifying (at room temperature) the gas stream through a controller evaporator mixer from Bronkhorst (Bronkhorst High-Tech, Ruurlo, The Netherlands). The percentage of humidity and the temperature during the measurements were checked using a digital sensor SENSIRION SHT85 (SENSIRION, Stäfa, Switzerland) placed inside the chamber. The accuracy of the SHT sensor is ±1.5% RH and 0.1 °C. An Arduino-based board was used to bridge the SHT sensor and the computer, interfacing the I^{2}C bus and USB.

Similarly, to check the selectivity, the sensors were exposed to benzene, toluene, carbon monoxide, ethanol, ammonia, and hydrogen. The exposures were performed using several pulses of the same level of concentration according to the STEL [**4**] of each gas or the maximum capacity of the available bottle in the storage room. For benzene was 1 ppm (STEL: 1 ppm), toluene was used the maximum capacity of the bottle 10 ppm (STEL: 50 ppm), carbon monoxide: 20 ppm (STEL: 20 ppm), ethanol was the maximum capacity of the bottle 20 ppm (STEL: 1000 ppm), ammonia was 50 ppm (STEL: 50 ppm) and hydrogen was the maximum capacity of the bottle 1000 ppm. In all cases, the sensing responses were calculated using Equation (1):

$$Response\ [\%] = \frac{(R_C - R_b)}{R_b}\ x\ 100\ \% \qquad (1)$$

Where R_c is the value of the resistance of the sensor before being exposed to a cycle of pulse train of the target gas and R_b corresponds to the value of the resistance after the target gas exposure in each pulse.

3. Results and Discussion

3.1. Active Layer Characterization

Figure 4a,b present the obtained FESEM images of NP and NF, respectively. A secondary electron detector was used to obtain images on a grayscale, with the nanoparticles as bright materials and a dark background representing the graphene layer. The images were taken on a 3 µm scale. **Figure 4**a shows the nanopillar structure of the ZnO with some porous formation (small dots) on the surface of the nanopillars, which increases the sensing performance of the active layer. These defects are incorporated into the material by microwave treatment. **Figure 4**b shows the morphology of the ZnO in a nanoflower shape, in the middle of the graphene layers. The FESEM image of BG is presented in **Figure S2 in the Supplementary Materials**.

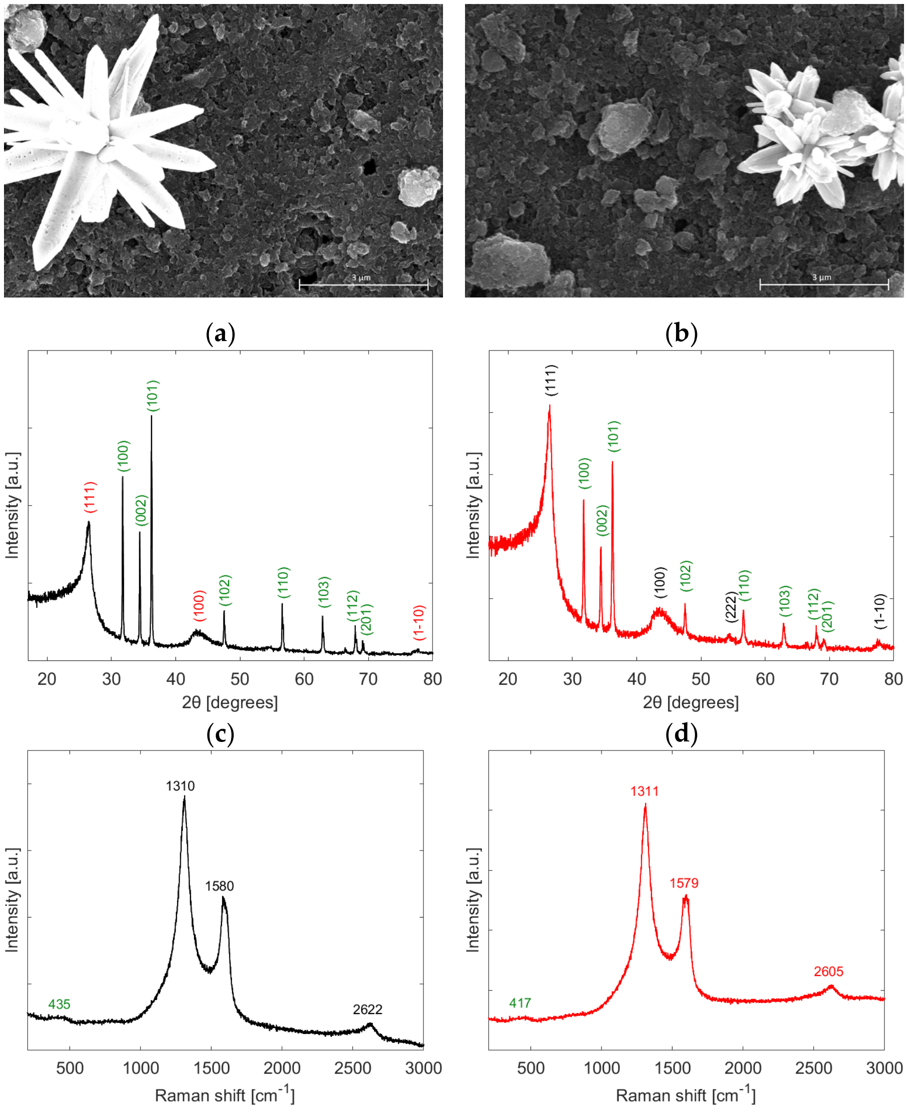

(**a**) (**b**)

(**c**) (**d**)

(**e**) (**f**)

Figure 4. FESEM images using Back-scattered electron detector of (**a**) NP, (**b**) NF; XRD diffractograms of (**c**) NP, (**d**) NF; Raman spectra of (**e**) NP, (**f**) NF.

The BET surface areas of the ZnO nanoparticles used for decorating the NP and NF sensors were measured by the nitrogen adsorption–desorption process. The surface area of the NF (2.499 m^2g^{-1}) was found to be smaller, yet close to the surface area of the NP (2.990 m^2g^{-1}).

A quantitative elemental analysis using EDX can be found in the Supplementary Materials, **Figure S3** for the NF. The spectrum shows different peaks such as oxygen, carbon, and zinc present on the surface. The strongest peak of zinc in the EDX spectrum is explained by the image being taken right on top of one of the nanoflowers on the surface. An equivalent spectrum can be found when analyzing the NP, Supplementary Materials Figures S4 and S5 for BG. **Figure 4**c,d show the XRD diffractograms for NP and NF materials, respectively. In this case, the samples were tested in powder form; therefore, a clear spectrum of the materials was obtained. It is noticed that the reflection peaks confirm the presence of carbon shown in the indices (111), (100), and (1–10) for the NP diffractogram. Also, for the NF diffractogram, it is noticed that there is an additional indicator of carbon with quite a low intensity (222). **Figure 4**e,f show the Raman spectra of the NP and NF samples, respectively. D-band is located at 1310 and 1311 cm^{-1} in each case, which indicates the presence of defects in the graphene lattice. The G-band located at 1580 and 1579 cm^{-1} reveals the stretching of C-C bonds in both sensors. Moreover, the 2D-band is located at 2622 and 2605 cm^{-1}, and its intensity could be an indicator of the number of graphene layers and is lower than the previous bands. Also, it is observed in both sensors a small peak at 435 and 417 cm^{-1}, which can be attributed to the presence of ZnO in the active layer, normally at 430 cm^{-1}. The Raman spectrum of BG is shown in Figure S6 in the Supplementary Materials.

3.2. Gas Sensing Results

Figure 5a shows the dynamic performance of the sensors under NO_2 exposure. The three materials have high baseline stability and good repeatability over the whole range of the measurements. It can be noticed that the electrical conductivity of the sensing layer increases due to the normal behavior of a p-type material such as graphene reacting to an oxidant gas such as NO_2. The signal-to-noise ratio is high since the sensors have a stable waveform variation of the resistance value during the sharp and fast waveform changes, right after the gas gets inside the chamber. Furthermore, it is noticed that the response of the sensor increases while the target gas concentration increases. **Figure 5**b shows the comparison between the calibration curves of the responses of the three sensors. Doped sensors have a bigger response than BG, and NF shows itself as the best sensor. For higher levels of nitrogen dioxide concentrations (1 ppm), the average ratio between the NF and BG responses is 1.45. For the lowest level of concentration (50 ppb), the average ratio increases to 3.58, which means that the response of NF is around 3.5 times higher than for BG. The same trend can be found when analyzing the ratio between NP and BG. In that manner, sensors doped with NP and NF were chosen to continue this study.

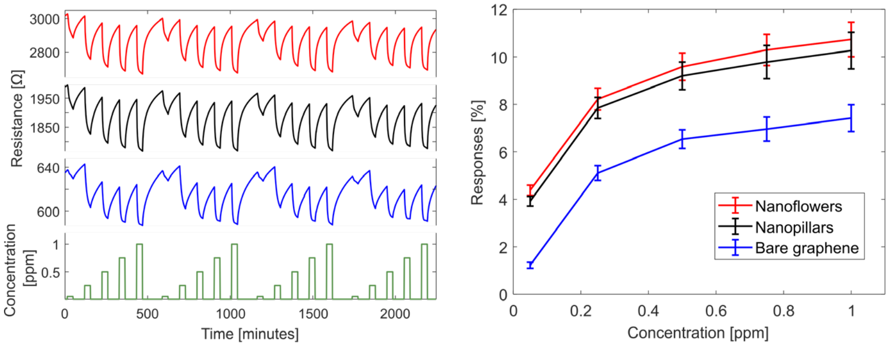

(**a**) (**b**)

Figure 5. (**a**) Repeatability of the measurement in dry air conditions, four cycles of pulses of 50, 250, 500, 750 ppb, and 1 ppm of NO_2 concentration (green color) and resistance variation of graphene-based sensors decorated to NF (red color), NP (black color) and BG (blue color). (**b**) Comparison between the calibration curves of NF, NP, and BG in dry air conditions.

An extended comparison was performed between NP and NF. **Figure 6**a,b show the fitted calibration curves in log scale using a power-law model for both sensors, which have an R^2 of 0.95 and 0.96 for NP and NF, respectively. As a result, the sensitivities of the two sensors at 1 ppm are equal to 3% ppm^{-1}. Likewise, the theoretical Limit of Detection (LoD) was calculated using Equation (2).

$$\mathrm{LoD} = \frac{3.3\sigma}{S} \tag{2}$$

where σ is the standard deviation of the baseline resistance during a long period of measurement and S is the Sensitivity of the sensors. In each case, the NP sample has a theoretical LoD of 18.7 ppb and the NF sample of 13.3 ppb.

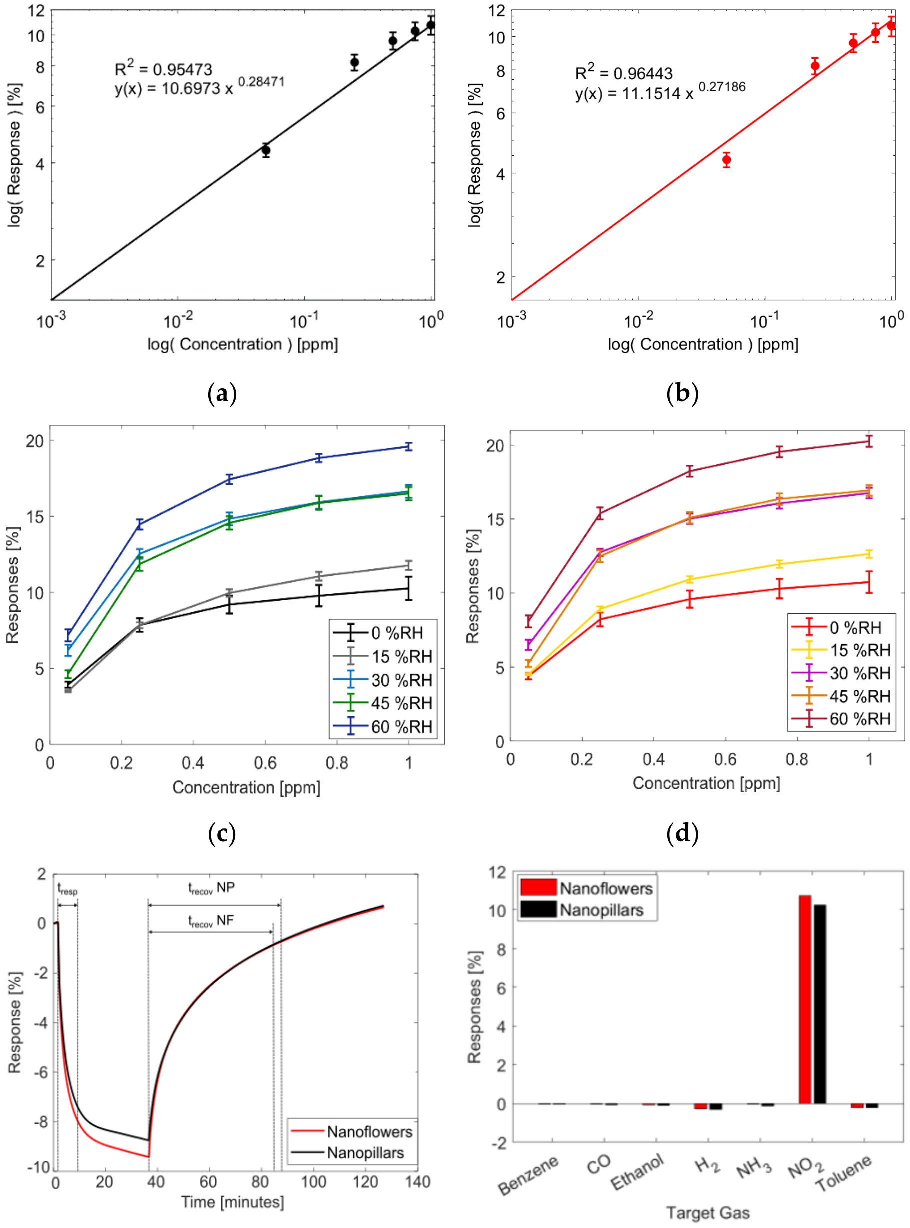

(**a**) (**b**)

(**c**) (**d**)

(**e**) (**f**)

Figure 6. Fitted calibration curves for (**a**) NP, (**b**) NF; Response under different levels of humidity: 0%, 15%, 30%, 45%, and 60% RH for (**c**) NP, (**d**) NF; (**e**) Comparison of response and recovery time between NP and NF; (**f**) Comparison between responses of the sensors when exposed to different gases/vapors.

Since it is extensively reported that humidity affects the response of graphene-based sensors [**42**,**43**,**44**,**45**], similar measurements and analyses were performed under different relative humidity levels. **Figure 6**c,d present a comparison of the calibration curves for NP and NF in dry air conditions: 15% RH, 30% RH, 45% RH, and 60% RH. It was noticed that the baseline of the sensors increased after each increase in % RH. Also, the response of the sensors increases while the % RH increases. The Sensor doped with NF almost doubled its response in the total range of humidity variation. Likewise, this response increase has a clear advantage for the final application of this work due to real measurements being under humidity conditions, but it also has a disadvantage, which is the dependability of the sensor response to the variation of % RH. This issue is easy to address by including a humidity sensor in the electronic design and performing a multivariate analysis in the software solution. These two final ideas are out of the scope of this paper.

Furthermore, the response and recovery times of the sensors were evaluated in dry air conditions. Under 1 ppm of NO_2 exposure, the sensors have a response/recovery time of around 10/47 and 10/49 min for NF and NP, respectively. **Figure 6**e shows the details of the comparison, and the response time is defined as the time taken to reach 90% of the full response after the introduction of the target gas. The recovery time is defined as the time taken to return to 90% of the baseline resistance after the flow of the target gas is stopped. They were calculated following Equations (3) and (4).

$$Response\_T\ [sec] = Time_{R\_90\%\_response} - Time_{R\_baseline} \tag{3}$$

$$Recovery_T[sec] = Time_{R_{90}\%_{baseline}} - Time_{R_{reacting}} \tag{4}$$

Where $Time_{R_{90}\%\_response}$ is the time when the resistance value reaches 90% of the response after reacting to the target gas. $Time_{R\_baseline}$ is the time before the sensor is exposed to the target gas. $Time_{R\_reacting}$ is the time before the sensor is exposed to dry air for a given recovery time and $Time_{R\_90\%\_baseline}$ is the time when the resistance value reaches the 90% of the previous baseline.

Finally, the sensors were exposed to different analytes to perform a selectivity comparison. To demonstrate that the wearable NFC tag system can be used in environments or industrial processes in which a combination of these analytes could be present in the atmosphere, the test was performed using VOC such as benzene, toluene, and ethanol [**4**,**46**,**47**,**48**], carbon monoxide [**7**,**8**,**49**], ammonia [**8**,**50**], and hydrogen [**49**]. **Figure 6**f presents a bar chart showing that the response of NP and NF to all these gases is less than 1% in dry air conditions. Therefore, the use of these two materials is suitable for sensing NO_2 concentrations, even in the presence of other compounds.

3.2. Sensing Mechanisms to NO_2

The behavior of the sensors described in previous sections, regardless of their good selectivity towards NO_2 concentrations and the increase in their responses as % RH increases, is consistent with the sensing mechanism of graphene-based sensors [**45**]. Graphene is a mild p-type nanomaterial that has a large surface area. This large area facilitates the adsorption of gas molecules, leading to rapid changes in the local carrier concentration and its conductivity. In the presence of oxidant gases, its conductivity is increased. Conversely, when detecting reducing gases, the conductivity decreases. Therefore, in the sensors used in this work, when reacting to NO_2, the resistance value decreases, and while reacting to other gases such as benzene or hydrogen, the resistance value of the sensor increases. Considering p-type graphene loaded with n-type ZnO nanoparticles, the probable outcome is the formation of a p-n junction on the contact surface. This formation creates a depletion layer at the interface, with electrons flowing from the ZnO conduction band to the graphene. As a result, NP and NF sensors exhibit a higher resistance baseline compared to the BG sensor due to the injection of electrons from the n-type ZnO to the graphene, reducing the concentration of majority carriers in the p-type graphene and lowering the conductivity of the sensing film. When NP and NF are exposed to dry air, they interact with oxygen molecules, capturing electrons from the valence band and causing them to be adsorbed into the sensor surface (Equation (5)). When NO_2 interacts with the sensor surface, two reactions may occur. First, NO_2 can be adsorbed onto the hybrid nanocomposite

(Equation (6)). Second, NO_2 may interact with adsorbed oxygen species, leading to changes in the resistivity of the active layer (Equation (7)). In both cases, NO_2 adsorption captures free electrons from the sensitive film, increasing the conductivity.

$$O_2(g)\ + 2e^- \rightarrow 2O_{2(ads.)^-} \tag{5}$$

$$NO_2(g)\ + e^- \rightarrow NO_{2(ads.)^-} \tag{6}$$

$$2NO_{2(ads.)}\ + O_{2-} + e^- \rightarrow\ 2NO_3^- \tag{7}$$

The p–n junction enhances the sensor sensitivity by expanding the depletion region when the film interacts with NO_2 molecules. NP and NF exhibit higher sensing performance than BG. Likewise, NF has a better response to NO_2 than NP, possibly because its contact area with the target gas is larger than that of NP. Finally, the presence of humidity enhances the sensitivity of graphene-based sensors. At room temperature, water molecules act as a mediated adsorption site for NO_2, and additional electrons are released in the conduction band of the metal oxide material, leading to an increased response to the target gas [45].

3.4. Gas Measurement Using NFC Tag System

Using the built-in wearable NFC tag system, a gas measurement test was performed. The system, with airbrushed graphene decorated with NF material, was placed inside a chamber. In this manner, the volume of the environment in which the system was placed increased. A new acrylic chamber was used with a volume of 5000 cm^3, and the system was powered using a coin cell battery, CR2032. Afterward, the system was left in synthetic dry air for one hour; in between, a stream of NO_2 concentration of 1 ppm was supplied to the chamber for 15 min (constant flow of 100 mL/min). **Figure S7a in the Supplementary Materials** shows a picture taken of the test bench for this test.

To recreate different possible scenarios of exposure to nitrogen dioxide, two additional tests were performed as follows. First, NO_2 at 1 ppm was supplied to the chamber for 10 min, followed by 10 min of dry air, and finally 500 ppb of NO_2 for another 10 min. After recovering the sensor in dry air, a second test comprised supplying the chamber with 500 ppb of NO_2 for 10 min, followed by a 10 min recovery in dry air, and ending with a 10 min exposure to 1 ppm of NO_2. Figure S7b,c in the Supplementary Materials shows a screenshot of a smartphone of the acquired data in each test, respectively. It is seen in both cases that the NFC tag system can successfully obtain the variation in the resistance value under different levels of concentration; hence, a data analysis to quantify the NO_2 concentrations in the software solution could be proposed using this system. It is also noticed in **Figure S7b,c** that the visualization time window in the App is one hour; therefore, even when the system can store more than 8 h, the data are visualized in 1 h segments for better visualization. This App is a custom-made Android application developed on the Android Studio platform, and it was developed for implementing these tests. The communication between the Android App and the system was conducted using a standard library that handles the Type 2 tag, MIFARE Ultralight protocol and initialization anticollision protocol activation, ISO 14443 A-3-2-1/ISO 18092, and NFC A tags [**51**].

4. Conclusion

This study demonstrates an effective technique to build a cumulative gas sensor using NFC technology. The integration of a sensing layer, the interdigitated electrodes, and the electronics on the same flexible printed circuit board gives a compact design, makes it easy to integrate with a working vest, and smooths the path to read out the sensor regardless of time and location. The synthesis of the zinc oxide nanoflowers and nanopillars mixed with graphene offered the possibility of obtaining sensors that work at room temperature. Also, it enabled obtaining sensors highly selective towards NO_2 concentrations, having a sensitivity of 3% ppm^{-1} in 1 ppm level for both sensors (nanopillars and nanoflowers), and a theoretical LoD of 18.7 ppb (nanopillars) and 13.3 ppb (nanoflowers), a response of 20.24% ± 0.38% (nanoflowers) and 19.59% ± 0.24% (nanopillars) under 1 ppm exposure at 60% RH. The use of the airbrush technique facilitates the assembly process of the system without interfering with the electronic design.

The wearable NFC tag system proofreads the concept of being used in a target application, in which human resources could be exposed to NO_2 concentrations during working hours. Nonetheless, a few improvements could be made to the final application. For instance, the inclusion of a visual or sonorous indicator when the target gas exposure increases would be suitable to alert the workers before reading the tag at the end of the working hours. Likewise, the inclusion of a humidity sensor would be suitable to address the effect of humidity on the sensor response with a multivariate analysis. Also, this system could be combined with standard alarm systems placed in the working area. Additionally, replacing the battery with a harvesting energy element would be an interesting approach to increasing the lifetime of this wearable NFC tag sensor.

It is important to notice that, to prove this concept, the selectivity toward NO_2 of these sensors has been tested toward interfering species such as benzene, toluene, carbon monoxide, ethanol, ammonia, and hydrogen. Anyhow, the analysis of other possible interfering gases, such as ozone, would be suitable for the subsequent version of this study. Furthermore, we strongly believe that this work could be used with different sensing materials, and these results will provide a new perspective for on-site monitoring, recording, and analysis of threatening gases in working environments. Therefore, the use of new materials that guarantee faster response and recovery time at room temperature would be a suitable research topic to continue this work and be integrated with an improved version of this wearable NFC tag system.

References

1. Nitrogen Dioxide|American Lung Association. Available online: https://www.lung.org/clean-air/outdoors/what-makes-air-unhealthy/nitrogen-dioxide (accessed on 3 October 2023).
2. Basic Information about NO2|US EPA. Available online: https://www.epa.gov/no2-pollution/basic-information-about-no2 (accessed on 27 September 2023).

3. Air Quality and Health. Available online: https://www.who.int/teams/environment-climate-change-and-health/air-quality-and-health/health-impacts/types-of-pollutants (accessed on 3 October 2023).

4. Carbone, U.; Montuori, P.; Novi, C.; Triassi, M. Respiratory Function in Power Plant Workers Exposed to Nitrogen Dioxide. *Occup. Med. (Chic Ill)* 2014, *64*, 644–646.

5. Plato, N.; Bigert, C.; Larsson, B.-M.; Alderling, M.; Svartengren, M.; Gustavsson, P. Exposure to Particles and Nitrogen Dioxide Among Workers in the Stockholm Underground Train System. *Saf. Health Work* 2019, *10*, 377–383.

6. Salonen, H.; Salthammer, T.; Morawska, L. Human Exposure to NO_2 in School and Office Indoor Environments. *Environ. Int.* 2019, *130*, 104887.

7. Dahmann, D.; Morfeld, P.; Monz, C.; Noll, B.; Gast, F. Exposure Assessment for Nitrogen Oxides and Carbon Monoxide in German Hard Coal Mining. *Int. Arch Occup. Environ. Health* 2009, *82*, 1267–1279.

8. Kurnia, J.C.; Sasmito, A.P.; Wong, W.Y.; Mujumdar, A.S. Prediction and Innovative Control Strategies for Oxygen and Hazardous Gases from Diesel Emission in Underground Mines. *Sci. Total Environ.* 2014, *481*, 317–334.

9. Homepage—ECHA. Available online: https://echa.europa.eu/ (accessed on 3 October 2023).

10. Park, N.-H.; Akamatsu, T.; Itoh, T.; Izu, N.; Shin, W. Calorimetric Thermoelectric Gas Sensor for the Detection of Hydrogen, Methane and Mixed Gases. *Sensors* 2014, *14*, 8350–8362.

11. Lee, S.W.; Lee, W.; Hong, Y.; Lee, G.; Yoon, D.S. Recent Advances in Carbon Material-Based NO_2 Gas Sensors. *Sens. Actuators B Chem* 2018, *255*, 1788–1804.

12. Agrawal, A.V.; Kumar, N.; Kumar, M. Strategy and Future Prospects to Develop Room-Temperature-Recoverable NO_2 Gas

Sensor Based on Two-Dimensional Molybdenum Disulfide. *Nanomicro Lett.* 2021, *13*, 38.

13. Zhang, J.; Liu, X.; Neri, G.; Pinna, N. Nanostructured Materials for Room-Temperature Gas Sensors. *Adv. Mater.* 2016, *28*, 795–831.

14. Shaik, M.; Rao, V.K.; Gupta, M.; Murthy, K.S.R.C.; Jain, R. Chemiresistive Gas Sensor for the Sensitive Detection of Nitrogen Dioxide Based on Nitrogen Doped Graphene Nanosheets. *RSC Adv.* 2016, *6*, 1527–1534.

15. Ibañez, F.J.; Zamborini, F.P. Chemiresistive Sensing with Chemically Modified Metal and Alloy Nanoparticles. *Small* 2012, *8*, 174–202.

16. Grilli, M.L. Metal Oxides. *Metals* 2020, *10*, 820.

17. Sun, Y.-F.; Liu, S.-B.; Meng, F.-L.; Liu, J.-Y.; Jin, Z.; Kong, L.-T.; Liu, J.-H. Metal Oxide Nanostructures and Their Gas Sensing Properties: A Review. *Sensors* 2012, *12*, 2610–2631.

18. Tomchenko, A.A.; Harmer, G.P.; Marquis, B.T.; Allen, J.W. Semiconducting Metal Oxide Sensor Array for the Selective Detection of Combustion Gases. *Sens. Actuators B Chem.* 2003, *93*, 126–134.

19. Meixner, H.; Lampe, U. Metal Oxide Sensors. *Sens. Actuators B Chem.* 1996, *33*, 198–202.

20. Zhang, C.; Luo, Y.; Xu, J.; Debliquy, M. Room Temperature Conductive Type Metal Oxide Semiconductor Gas Sensors for NO_2 Detection. *Sens. Actuators A Phys.* 2019, *289*, 118–133.

21. Drewniak, S.; Drewniak, Ł.; Pustelny, T. Mechanisms of NO_2 Detection in Hybrid Structures Containing Reduced Graphene Oxide: A Review. *Sensors* 2022, *22*, 5316.

22. Demon, S.Z.N.; Kamisan, A.I.; Abdullah, N.; Noor, S.A.M.; Khim, O.K.; Kasim, N.A.M.; Yahya, M.Z.A.; Manaf, N.A.A.; Azmi, A.F.M.; Halim, N.A. Graphene-Based Materials in Gas Sensor Applications: A Review. *Sens. Mater.* 2020, *32*, 759.

23. Sun, D.; Luo, Y.; Debliquy, M.; Zhang, C. Graphene-Enhanced Metal Oxide Gas Sensors at Room Temperature: A Review. *Beilstein J. Nanotechnol.* 2018, *9*, 2832–2844.

24. Xiao, Y.; Li, H.; Wang, C.; Pan, S.; He, J.; Liu, A.; Wang, J.; Sun, P.; Liu, F.; Lu, G. Room Temperature Wearable Gas Sensors for Fabrication and Applications. *Adv. Sens. Res.* 2023, 2300035.

25. Alouani, M.A.; Casanova-Cháfer, J.; Güell, F.; Peña-Martín, E.; Ruiz-Martínez-Alcocer, S.; de Bernardi-Martín, S.; García-Gómez, A.; Vilanova, X.; Llobet, E. ZnO-Loaded Graphene for NO_2 Gas Sensing. *Sensors* 2023, *23*, 6055.

26. Vaghasiya, J.V.; Mayorga-Martinez, C.C.; Pumera, M. Wearable Sensors for Telehealth Based on Emerging Materials and Nanoarchitectonics. *NPJ Flex. Electron.* 2023, *7*, 26.

27. Zhou, C.; Shi, N.; Jiang, X.; Chen, M.; Jiang, J.; Zheng, Y.; Wu, W.; Cui, D.; Haick, H.; Tang, N. Techniques for Wearable Gas Sensors Fabrication. *Sens. Actuators B Chem.* 2022, *353*, 131133.

28. Alrammouz, R.; Podlecki, J.; Abboud, P.; Sorli, B.; Habchi, R. A Review on Flexible Gas Sensors: From Materials to Devices. *Sens. Actuators A Phys.* 2018, *284*, 209–231.

29. Smith, A.A.; Li, R.; Tse, Z.T.H. Reshaping Healthcare with Wearable Biosensors. *Sci. Rep.* 2023, *13*, 4998.

30. Chen, X.; Wang, T.; Han, Y.; Lv, W.; Li, B.; Su, C.; Zeng, M.; Yang, J.; Hu, N.; Su, Y.; et al. Wearable NO_2 Sensing and Wireless Application Based on ZnS Nanoparticles/Nitrogen-Doped Reduced Graphene Oxide. *Sens. Actuators B Chem.* 2021, *345*, 130423.

31. Zhang, F.; Lin, Q.; Han, F.; Wang, Z.; Tian, B.; Zhao, L.; Dong, T.; Jiang, Z. A Flexible and Wearable NO_2 Gas Detection and Early Warning Device Based on a Spraying Process and an Interdigital Electrode at Room Temperature. *Microsyst. Nanoeng.* 2022, *8*, 40.

32. Lee, S.P.; Ha, G.; Wright, D.E.; Ma, Y.; Sen-Gupta, E.; Haubrich, N.R.; Branche, P.C.; Li, W.; Huppert, G.L.; Johnson, M.; et al. Highly

Flexible, Wearable, and Disposable Cardiac Biosensors for Remote and Ambulatory Monitoring. *NPJ Digit. Med.* 2018, *1*, 2.

33. Lin, R.; Kim, H.-J.; Achavananthadith, S.; Kurt, S.A.; Tan, S.C.C.; Yao, H.; Tee, B.C.K.; Lee, J.K.W.; Ho, J.S. Wireless Battery-Free Body Sensor Networks Using near-Field-Enabled Clothing. *Nat. Commun.* 2020, *11*, 444.

34. Cao, Z.; Chen, P.; Ma, Z.; Li, S.; Gao, X.; Wu, R.; Pan, L.; Shi, Y. Near-Field Communication Sensors. *Sensors* 2019, *19*, 3947.

35. Olenik, S.; Lee, H.S.; Güder, F. The Future of Near-Field Communication-Based Wireless Sensing. *Nat. Rev. Mater* 2021, *6*, 286–288.

36. Escobedo, P.; Fernández-Ramos, M.D.; López-Ruiz, N.; Moyano-Rodríguez, O.; Martínez-Olmos, A.; Pérez de Vargas-Sansalvador, I.M.; Carvajal, M.A.; Capitán-Vallvey, L.F.; Palma, A.J. Smart Facemask for Wireless CO_2 Monitoring. *Nat. Commun.* 2022, *13*, 72.

37. Zhang, L.; Tan, Q.; Kou, H.; Wu, D.; Zhang, W.; Xiong, J. Highly Sensitive NH_3 Wireless Sensor Based on Ag-RGO Composite Operated at Room-Temperature. *Sci. Rep.* 2019, *9*, 9942.

38. Escobedo, P.; Erenas, M.M.; López-Ruiz, N.; Carvajal, M.A.; Gonzalez-Chocano, S.; de Orbe-Payá, I.; Capitán-Valley, L.F.; Palma, A.J.; Martínez-Olmos, A. Flexible Passive near Field Communication Tag for Multigas Sensing. *Anal. Chem.* 2017, *89*, 1697–1703.

39. Xu, G.; Zhang, Q.; Lu, Y.; Liu, L.; Ji, D.; Li, S.; Liu, Q. Passive and Wireless near Field Communication Tag Sensors for Biochemical Sensing with Smartphone. *Sens. Actuators B Chem.* 2017, *246*, 748–755.

40. Salehnia, F.; Lazaro, A.; Villarino, R.; Lazaro, M.; Canyellas, N.; Vilanova, X.; Llobet, E.; Girbau, D. Battery-Free NFC Sub-ppm Gas Sensor for Distributed Gas Monitoring Applications at Room Temperature. *IEEE J. Radio Freq. Identif.* 2023, *7*, 630–643.

41. NXP Semiconductors NFC Antenna Design Tool | Antenna Design Hub | NXP Semiconductors. Available online: https://www.nxp.com/products/rfid-nfc/nfc-hf/nfc-readers/nfc-antenna-design-hub:NFC-ANTENNA-DESIGN-TOOL (accessed on 30 November 2023).

42. Lv, C.; Hu, C.; Luo, J.; Liu, S.; Qiao, Y.; Zhang, Z.; Song, J.; Shi, Y.; Cai, J.; Watanabe, A. Recent Advances in Graphene-Based Humidity Sensors. *Nanomaterials* 2019, *9*, 422.

43. Alfano, B.; Massera, E.; Polichetti, T.; Miglietta, M.L.; Di Francia, G. Effect of Humidity on the Hydrogen Sensing in Graphene Based Devices. In *Lecture Notes in Electrical Engineering*; Springer: Berlin, Germany, 2019; Volume 539, pp. 11–16.

44. Smith, A.D.; Elgammal, K.; Fan, X.; Lemme, M.C.; Delin, A.; Råsander, M.; Bergqvist, L.; Schröder, S.; Fischer, A.C.; Niklaus, F.; et al. Graphene-Based CO_2 Sensing and Its Cross-Sensitivity with Humidity. *RSC Adv.* 2017, *7*, 22329–22339.

45. Roso, S.; Bittencourt, C.; Umek, P.; González, O.; Güell, F.; Urakawa, A.; Llobet, E. Synthesis of Single Crystalline In_2O_3 Octahedra for the Selective Detection of NO_2 and H_2 at Trace Levels. *J. Mater. Chem. C Mater.* 2016, *4*, 9418–9427.

46. Parra, M.; Elustondo, D.; Bermejo, R.; Santamaria, J. Ambient Air Levels of Volatile Organic Compounds (VOC) and Nitrogen Dioxide (NO_2) in a Medium Size City in Northern Spain. *Sci. Total Environ.* 2008, *407*, 999–1009.

47. Kountouriotis, A.; Aleiferis, P.G.; Charalambides, A.G. Numerical Investigation of VOC Levels in the Area of Petrol Stations. *Sci. Total Environ.* 2014, *470–471*, 1205–1224.

48. Kamal, M.S.; Razzak, S.A.; Hossain, M.M. Catalytic Oxidation of Volatile Organic Compounds (VOCs)—A Review. *Atmos. Environ.* 2016, *140*, 117–134.

49. Li, H.; Liu, S.; Liew, C.; Li, Y.; Wayne, S.; Clark, N. An Investigation on the Mechanism of the Increased NO_2 Emissions from H_2-Diesel Dual Fuel Engine. *Int. J. Hydrog. Energy* 2018, *43*, 3837–3844.

50. Heck, R.M. Catalytic Abatement of Nitrogen Oxides–Stationary Applications. *Catal. Today* 1999, *53*, 519–523.

51. *ISO/IEC 14443-3:2018*; Cards and Security Devices for Personal Identification—Contactless Proximity Objects—Part 3: Initialization and Anticollision. International Organization for Standardization: Geneva, Switzerland, 2018. Available online: https://www.iso.org/standard/73598.html (accessed on 18 February 2024).

52. Zhang, B.; Cheng, M.; Liu, G.; Gao, Y.; Zhao, L.; Li, S.; Wang, Y.; Liu, F.; Liang, X.; Zhang, T.; et al. Room Temperature NO_2 Gas Sensor Based on Porous Co_3O_4 Slices/Reduced Graphene Oxide Hybrid. *Sens. Actuators B Chem.* 2018, *263*, 387–399.

53. Li, W.; Chen, R.; Qi, W.; Cai, L.; Sun, Y.; Sun, M.; Li, C.; Yang, X.; Xiang, L.; Xie, D.; et al. Reduced Graphene Oxide/Mesoporous ZnO NSs Hybrid Fibers for Flexible, Stretchable, Twisted, and Wearable NO_2 E-Textile Gas Sensor. *ACS Sens.* 2019, *4*, 2809–2818.

54. Kim, Y.H.; Kim, S.J.; Kim, Y.-J.; Shim, Y.-S.; Kim, S.Y.; Hong, B.H.; Jang, H.W. Self-Activated Transparent All-Graphene Gas Sensor with Endurance to Humidity and Mechanical Bending. *ACS Nano* 2015, *9*, 10453–10460.

55. Luan, Y.; Zhang, S.; Nguyen, T.H.; Yang, W.; Noh, J.S. Polyurethane Sponges Decorated with Reduced Graphene Oxide and Silver Nanowires for Highly Stretchable Gas Sensors. *Sens. Actuators B Chem.* 2018, *265*, 609–616.

56. Huang, L.; Wang, Z.; Zhang, J.; Pu, J.; Lin, Y.; Xu, S.; Shen, L.; Chen, Q.; Shi, W. Fully Printed, Rapid-Response Sensors Based on Chemically Modified Graphene for Detecting NO_2 at Room Temperature. *ACS Appl. Mater. Interfaces* 2014, *6*, 7426–7433.

57. Deng, S.; Tjoa, V.; Fan, H.M.; Tan, H.R.; Sayle, D.C.; Olivo, M.; Mhaisalkar, S.; Wei, J.; Sow, C.H. Reduced Graphene Oxide Conjugated Cu_2O Nanowire Mesocrystals for High-Performance NO_2 Gas Sensor. *J. Am. Chem. Soc.* 2012, *134*, 4905–4917.

58. Wang, Z.; Gao, S.; Fei, T.; Liu, S.; Zhang, T. Construction of ZnO/SnO_2 Heterostructure on Reduced Graphene Oxide for Enhanced Nitrogen Dioxide Sensitive Performances at Room Temperature. *ACS Sens.* 2019, *4*, 2048–2057.

59. Liu, X.; Sun, J.; Zhang, X. Novel 3D Graphene Aerogel–ZnO Composites as Efficient Detection for NO_2 at Room Temperature. *Sens. Actuators B Chem.* 2015, *211*, 220–226.

60. Ugale, A.D.; Umarji, G.G.; Jung, S.H.; Deshpande, N.G.; Lee, W.; Cho, H.K.; Yoo, J.B. ZnO Decorated Flexible and Strong Graphene Fibers for Sensing NO_2 and H_2S at Room Temperature. *Sens. Actuators B Chem.* 2020, *308*, 127690.

61. Lin, C.S.; Hsieh, H.F.; Ding, C.F.; Li, K.M.; Young, H.T.; Hsiao, W.T. Laser Surface Modification on RGO/ZnO Composite Materials for NO_2 Gas Sensing. *Mater. Chem. Phys.* 2022, *290*, 126551.

62. Li, J.; Liu, X.; Sun, J. One Step Solvothermal Synthesis of Urchin-like ZnO Nanorods/Graphene Hollow Spheres and Their NO_2 Gas Sensing Properties. *Ceram. Int.* 2016, *42*, 2085–2090.

63. Zhu, R.; Azzarelli, J.M.; Swager, T.M. Wireless Hazard Badges to Detect Nerve-Agent Simulants. *Angew. Chem. Int. Ed.* 2016, *55*, 9662–9666.

64. Barandun, G.; Soprani, M.; Naficy, S.; Grell, M.; Kasimatis, M.; Chiu, K.L.; Ponzoni, A.; Güder, F. Cellulose Fibers Enable Near-Zero-Cost Electrical Sensing of Water-Soluble Gases. *ACS Sens.* 2019, *4*, 1662–1669.

65. Ma, Z.; Chen, P.; Cheng, W.; Yan, K.; Pan, L.; Shi, Y.; Yu, G. Highly Sensitive, Printable Nanostructured Conductive Polymer Wireless Sensor for Food Spoilage Detection. *Nano Lett.* 2018, *18*, 4570–4575.

66. Zhu, R.; Desroches, M.; Yoon, B.; Swager, T.M. Wireless Oxygen Sensors Enabled by Fe(II)-Polymer Wrapped Carbon Nanotubes. *ACS Sens.* 2017, *2*, 1044–1050.

67. Choi, J.; Visagie, I.; Chen, Y.; Abbel, R.; Parker, K. NFC-Enabled Dual-Channel Flexible Printed Sensor Tag. *Sensors* 2023, *23*, 6765.

Chapter 5

Conclusions and Future Perspectives

UNIVERSITAT ROVIRA I VIRGILI
Development of wearable electronic devices, on low-cost flexible support for gas sensing Applications
Alejandro Santos Betancourt

4.1 General Conclusions

This thesis involved different areas of knowledge essential to combining electronic devices with low-dimensional materials for gas sensing applications. These areas include subjects related to gas sensors (fabrication techniques, material characterization, and gas sensing properties knowledge), the design of the related instrumentation to extract the data from the sensors (hardware and software design), and data analysis for discrimination and quantification of the target analyte (ANNs).

Gas sensors: Two different fabrication techniques were used during the development of this thesis. First, AACVD was used to grow tungsten oxide nanowires. Second, the airbrush deposition technique was used to fabricate graphene-based sensors to be included in a wearable device. A sensitive layer based on graphene was selected because it can operate at room temperature, a suitable feature for integrating them into battery-powered devices. Also, it was found that airbrushing is a suitable deposition technique when sensors are integrated into the same board as their read-out instrumentation.

Materials characterization and gas sensing properties: The sensitive layers of the fabricated sensors (WO_3-based and graphene-based) were fully characterized. It served to understand chemoresistor gas sensors' features: their working principle, advantages, and disadvantages. It was understood how to read data from the chemoresistor sensors and the main characteristics of the read-out chain instrumentation to interface them. The structural properties, morphological characteristics, and chemical compositions were checked using techniques such as Field Emission Scanning Electron Microscopy (FESEM), Energy-Dispersive X-ray (EDX), X-ray Diffraction (XRD), Raman spectroscopy, High-Resolution Transmission Electron Microscopy (HR-TEM), and Time-of-Flight Secondary Ion Mass Spectrometry (ToF-SIMS). These techniques confirmed that all materials were successfully deposited on top of the IDEs and helped to understand the formation of sensitive layers and how they interact with target analytes. The sensors' responses were evaluated to oxidizing and reducing species such as nitrogen dioxide, hydrogen, ammonia, and others at ppb and ppm levels. The sensors used to build the wearable device, obtained a high selectivity towards NO_2 concentrations, having a sensitivity of 3% ppm^{-1} in 1 ppm level. Graphene sensors were loaded with nanopillars and nanoflowers of zinc oxide to enhance their response to NO_2. This resulted in responses of 20.24% ± 0.38% for nanoflowers and 19.59% ± 0.24% for nanopillars under 1 ppm exposure at 60% RH.

Hardware and software design: Two electronics were designed with embedded software and a test user interface. The first one (nodes on IoT platform) interfaces up to four chemoresistor WO_3-based sensors. Includes some control algorithms to manage the operation temperature of sensors, the correct bias of each sensor, the dynamic configuration of the analog channel, and failure/recovery data due to wireless connection. The design includes Wi-Fi technology and is part of an IoT platform based on the MQTT protocol. During the development of this platform, a reconfiguration methodology was established, being able to add new sensors or include more nodes to the platform and be deployed in several scenarios. It is worth mentioning that the platform has an environmental commercial sensor to be used in the data analysis stage for humidity and temperature compensation. The second hardware design (wearable) integrates interdigitated electrodes and the electronics on the same flexible printed circuit board. It was built on flexible support enhancing wearable requirements. The device has a compact design, making easy its placement on clothes like a working vest. The small electronic design smooths the path to a wireless read-out of the sensor since it is based on NFC technology. The obtained wearable is powered by a coin cell battery and has an average power consumption of 24.9 μW. It is also extremely lightweight, 5 grams, and has a theoretical working life of more than one year.

Data analysis: It was confirmed that using statistical analysis in gas sensing applications enhances the system's output. Cross-responsive

WO_3-based sensors were used as an array and their data was processed using two different multivariate techniques: PCA and MLP. It was obtained a high discrimination ability (H_2: > 86%, EtOH > 90%, and NO_2: > 96%) and a good quantification ability ($R^2 \sim 0.94$) on validation data that had not been used for training. On the other hand, the implementation of ANNs in the user interface of the IoT platform gave the possibility of discriminating and quantifying pollutants on-site. A discrimination accuracy was obtained under a mixture of gases and the variation of % RH, 99.2% and 98.7%, respectively. Similarly, the quantification of gas concentration was computed using ANNs. More than 0.93 R^2 was obtained in all cases. The inclusion of environmental sensors in the analysis considerably improves the output of the classification and quantification models.

4.2 Further steps

The next step for continuing this study should be testing new materials with an electronic design on the same flexible support. In parallel, reduce the electronics design size to be adapted to any type of application, the size of antennas for wireless communication, and the number of commercial components. Further, test other wireless technologies such as BLE when designing a wearable device, integrating other types of antennas that work at higher frequencies in flexible substrates.

Another step could be, to incorporate IoT protocols on the wearable device, increasing the interconnectivity and interoperability of the devices. Also, implementing Machine Learning algorithms inside low-cost and low-power microcontrollers could be an interesting approach. A power consumption comparison could be done between the scenarios in which data is continuously transmitted or ML algorithms are running inside the microcontroller without the need to transmit the data continuously for external processing.

Also, replacing the battery with an energy harvester element from temperature or movement could be an interesting path to continue this study. Therefore, finding materials that generate power from these sources is definitely a to-go choice. Likewise, the data of wearable devices could be combined with fixed devices such as the one created in Chapter 3. It would be interesting to deploy both systems to monitor pollutants at a target area of study.

Finally, it is worth mentioning that low dimensional materials that operate at room temperature, smart electronics with IoT and ANN capabilities, integrated in flexible support create a powerful team for next-generation air pollution monitoring wearable devices. Therefore, continuing this research should be a must for enriching these fields of knowledge.

Annex

Publications included in this thesis

- Alejandro Santos-Betancourt, Eric Navarrete, Damien Cossement, Carla Bittencourt, and Eduard Llobet. AACVD synthesized tungsten oxide-NWs loaded with osmium oxide as a gas sensor array: enhancing detection with PCA and ANNs. RSC Advances, Issue 47, 2024, 14, 34985-34995, November 1st, 2024. DOI: https://doi.org/10.1039/D4RA05346J.

- Alejandro Santos-Betancourt, José Carlos Santos-Ceballos, Foad Salehnia, Mohamed Ayoub Alouani, Alfonso Romero, José Luis Ramírez, and Xavier Vilanova. IoT Platform Enhanced with Neural Network for Air Pollutant Monitoring. IEEE Transactions on Instrumentation and Measurement, Vol: 73, 2024, ASN: 2534511, DOI: 10.1109/TIM.2024.3481592.

- Alejandro Santos-Betancourt, José Carlos Santos-Ceballos, Mohamed Ayoub Alouani, Shuja Bashir Malik, Alfonso Romero, José Luis Ramírez, Xavier Vilanova, and Eduard Llobet. ZnO Decorated Graphene-Based NFC Tag for Personal NO_2 Exposure Monitoring during a Workday. Sensors, February 2024, 24(5), 1431. DOI: https://doi.org/10.3390/s24051431.

Publications not included in this thesis

- Mohamed Ayoub Alouani, Juan Casanova-Chafer, Santiago de Bernardi-Martín, Alejandra García-Gómez, Foad Salehnia, José Carlos Santos-Ceballos, Alejandro Santos-Betancourt, Xavier Vilanova, Eduard Llobet. The effect of doping rGO with MnO_2 nanomaterial on its gas sensing properties. Sensors, Preprint versión. DOI: 10.20944/preprints202410.1611.v1

Oral presentations

- **TecnATox** annual Workshop, Reus, Tarragona, Spain, 2024. Oral presentation: ZnO decorated Graphene-based NFC tag for NO_2 monitoring.
- XI Franco-Spanish Workshop **IBERNAM-CMC2**, Zaragoza, Spain, 2023. Oral presentation: Development of a wireless sensor network for air quality monitoring.
- Demo Day **H2CAT**, Barcelona, Spain, 2023. Live demonstration: IoT system for gas sensing application.
- **ISOCS** Short Course Winter, Bormio, Lombardy, Italy, 2023. Oral presentation and live demonstration: Wireless gas sensor network.

Secondments associated with this thesis

- **InanoEnergy**, Porto, Portugal, 2023. Development of an electronic control system to interface energy harvesters from temperature.
- **CeNTI / CITEVE**, Vila Nova de Famalicão, Portugal, 2023. Development of flexible gas sensors based on graphene using screen-printing.
- **JLM Innovation GmbH**, Tubingen, Germany, 2022. Design an electronic board to sense MOX sensors and send the data using the MQTT protocol in an IoT Application.

Supplementary Material Chapter 2

AACVD Synthesized Tungsten Oxide-NWs loaded with Osmium oxide as Gas Sensor Array: Enhancing Detection with PCA and ANNs

Alejandro Santos-Betancourt [1,2,3], Èric Navarrete [1], Damien Cossement [4], Carla Bittencourt [5], and Eduard Llobet [1,2,3*]

[1] Universitat Rovira i Virgili, Microsystems Nanotechnologies for Chemical Analysis (MINOS), Departament d’Enginyeria Electrònica, Països Catalans, 26, 43007 Tarragona, Catalunya, Spain

[2] IU-RESCAT, Research Institute in Sustainability, Climatic Change and Energy Transition, Universitat Rovira i Virgili, Joanot Martorell 15, 43480 Vila-seca, Spain

[3] TecnATox - Centre for Environmental, Food and Toxicological Technology, Universitat Rovira i Virgili, Avda. Països Catalans 26, 43007 Tarragona, Spain

[4] Materia Nova Research Center, Parc Initialis, Avenue Copernic 3, 7000 Mons, Belgium

[5] Chimie des Interactions Plasma – Surface (ChIPS), Research Institute for Materials Science and Engineering, Université de Mons, Parc Initialis, Avenue Copernic 3, 7000 Mons, Belgium

[*] Corresponding author

Figure S1 shows (upper panel) an EDX analysis conducted on a sensor sample. The osmium loaded tungsten oxide film coats an alumina substrate. Peaks corresponding to the tungsten oxide film and the alumina substrate clearly appear. However, osmium is not detected. (lower panel) quantitative results of the microanalysis.

The experiment conditions were:

- Live Time: 40.0 sec
- Filter Fit Chi Squared:13.977 Errors: +/- 1 Sigma
- Correction Method: Proza (Phi-Rho-Z) Acc.Voltage: 20.0 kV
- Take Off Angle: 34.9 deg.

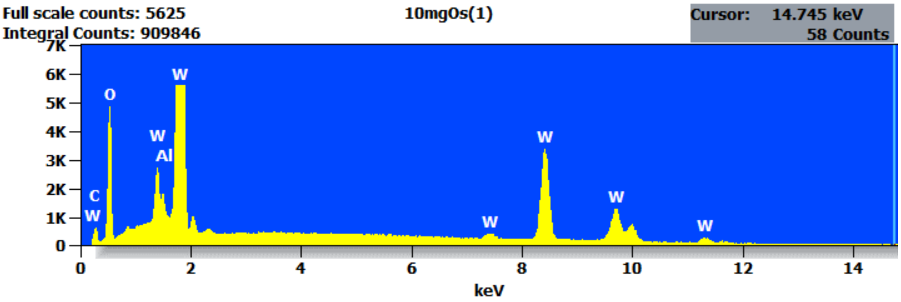

Element	*Weight %*	*Weight % Error*	*Norm. Wt.%*	*Atom %*	*Formula*
C	2.53	± 0.04	2.53	11.32	C
O	19.17	± 0.15	19.17	64.37	O
Al	0.84	± 0.04	0.84	1.68	Al
W	77.45	± 0.79	77.45	22.63	W
Total	100.00		100.00	100.00	

Figure S1: EDX performed to a WO_3 decorated with osmium.

Figure S2 shows the results of a different EDX analysis conducted on an osmium loaded tungsten oxide sample deposited on a TEM grid (lacey carbon film supported on nickel). Similarly to the previous EDX analysis performed on a sensor sample, this analysis is inconclusive for the presence of osmium in osmium-loaded samples.

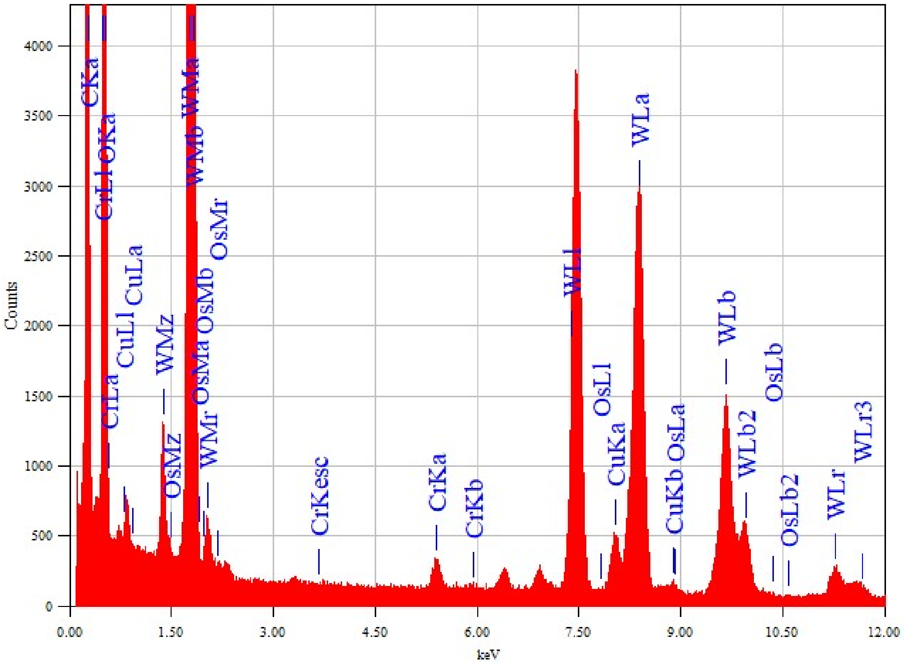

Figure S2: EDX analysis performed to an WO_3 decorated with osmium deposited on a TEM grid.

On the use of ToF-SIMS to confirm the presence of osmium oxide in the samples

An XPS analysis of the different samples was performed. However, the amount of Os that loaded the tungsten oxide was found to be under the sensitivity of the XPS technique and this for the two types of samples produced. The calculated detection limit of Osmium by XPS is 1.5 ppm. Therefore, to evaluate the presence of Osmium, the ToF-SIMS technique was employed, which is more sensitive technique than XPS, as it enables detecting the presence of chemical species at trace levels, down to ppb concentrations. However, unlike XPS, the ToF-SIMS is a qualitative technique, which has enabled confirming the presence of Os in the loaded tungsten oxide samples, but that does not allow for a proper quantitative analysis of this loading. Additionally, the TOF-SIMS analyses were performed in *spectrometry mode* (not in *imaging mode*), with a lateral resolution of roughly 1-2 μm. Therefore, it is not possible to determine the characteristic size and morphology of the Osmium clusters.

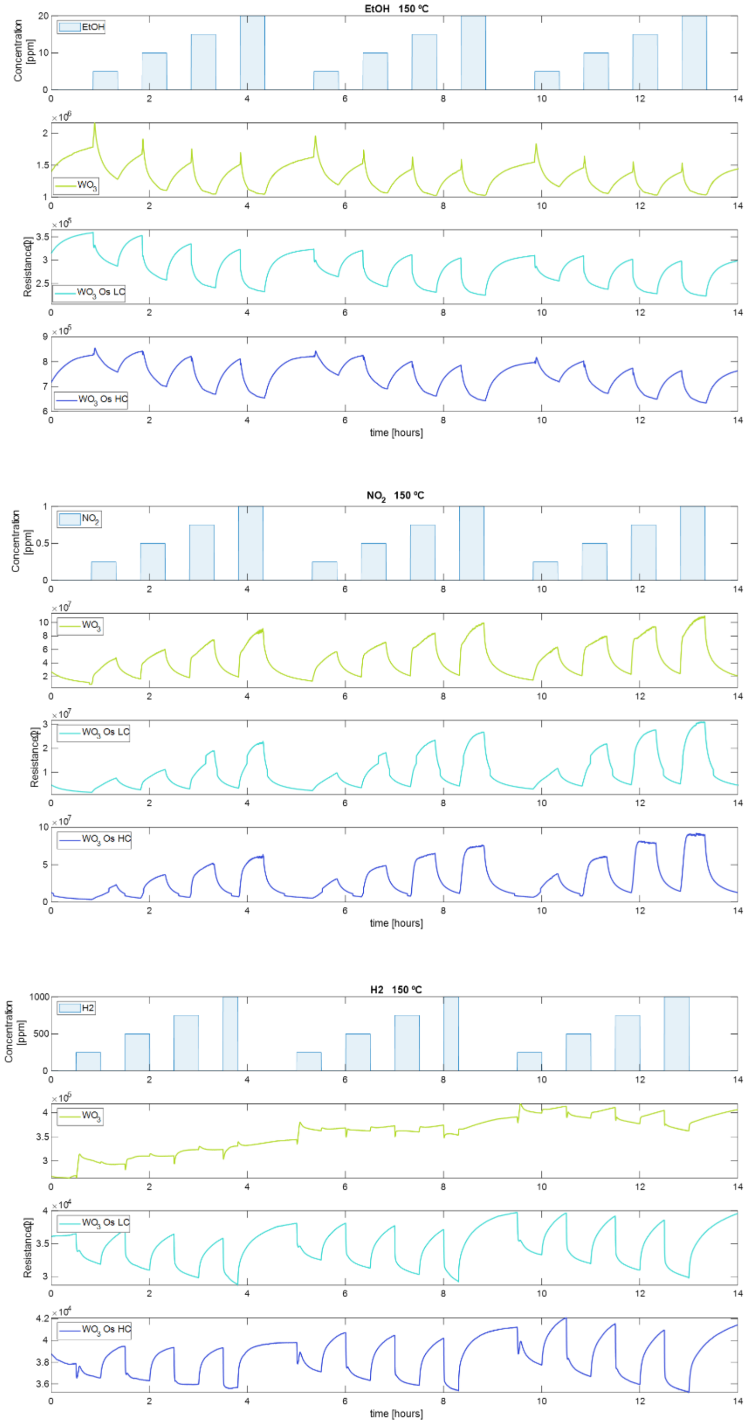

Figure S3: Measurements at 150 °C of (up) EtOH, (middle) NO_2, and (down) H_2.

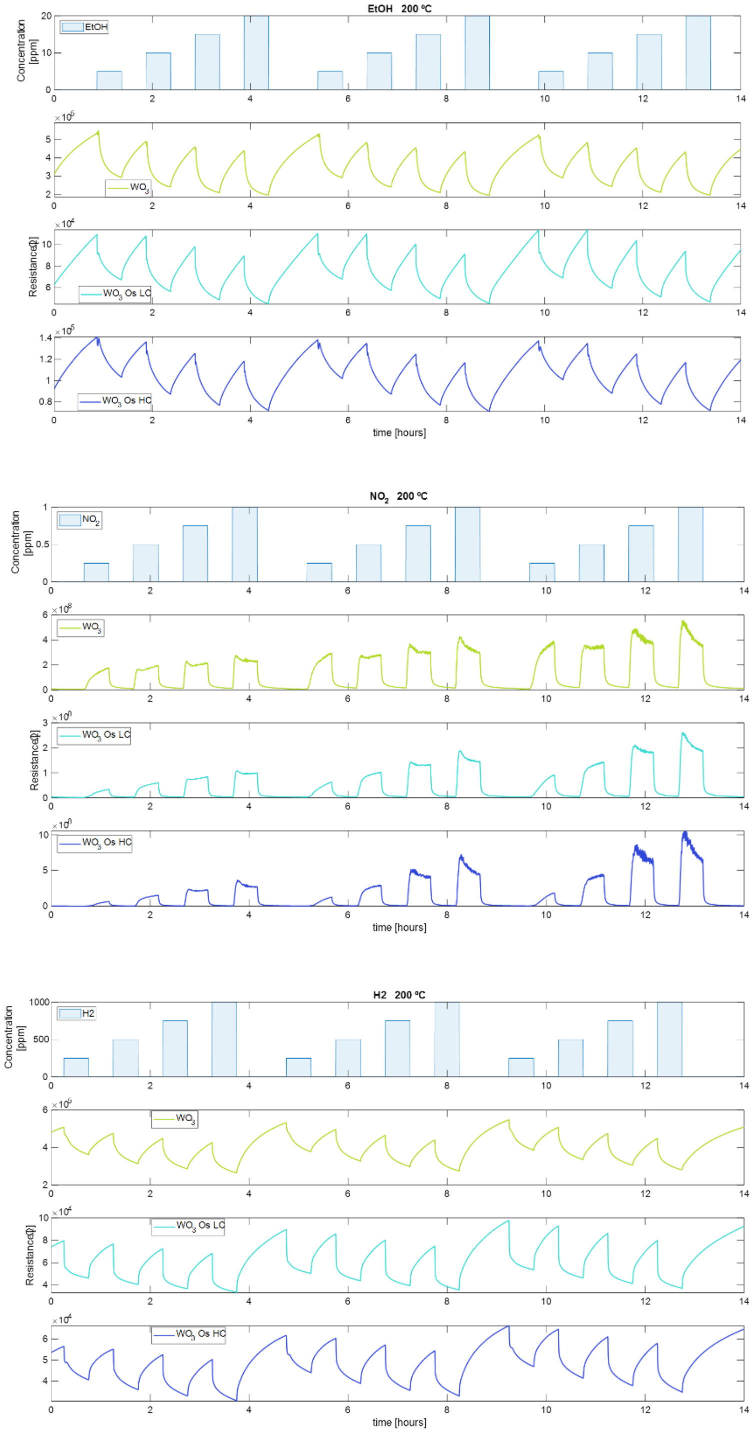

Figure S4: Measurements at 200 °C of (up) EtOH, (middle) NO_2, and (down) H_2.

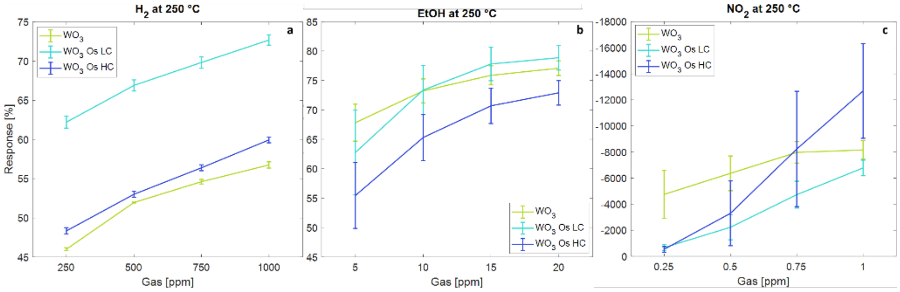

Figure S5: Calibration curves at 250 °C of (a) H_2, (b) EtOH, and (down) NO_2.

Table S1: Summary of the statistics of sensor measurements.

Sensor	Gas	Temp. [°C]	Concentration [ppm]	Resp. Mean [%]	Resp. Error [%]	Abs. Error [ppm]	Rel. Error [%]
pure	NO_2	250	0.25	-4749.6	1843.1	-0.24	-95.03
pure	NO_2	250	0.5	-6364.0	1336.0	-0.26	-52.24
pure	NO_2	250	0.75	-7970.8	825.4	-0.21	-27.45
pure	NO_2	250	1	-8160.0	710.0	-0.21	-21.05
pure	H_2	250	250	46.0	0.18	6.35	2.54
pure	H_2	250	500	52.0	0.06	3.65	0.73
pure	H_2	250	750	54.6	0.29	26.45	3.53
pure	H_2	250	1000	56.8	0.40	47.00	4.70
pure	EtOH	250	5	67.8	3.1	2.47	49.35
pure	EtOH	250	10	73.2	2.0	2.99	29.88
pure	EtOH	250	15	75.9	1.6	3.45	23.00
pure	EtOH	250	20	77.1	1.2	3.43	17.13
WO_3OsLC	NO_2	250	0.25	-667.4	239.8	-0.05	-19.16
WO_3OsLC	NO_2	250	0.5	-2227.7	964.5	-0.13	-26.37
WO_3OsLC	NO_2	250	0.75	-4728.7	1030.8	-0.11	-15.05
WO_3OsLC	NO_2	250	1	-6779.3	592.4	-0.06	-5.54
WO_3OsLC	H_2	250	250	62.2	0.76	27.71	11.09
WO_3OsLC	H_2	250	500	66.9	0.71	47.60	9.52
WO_3OsLC	H_2	250	750	69.8	0.71	68.86	9.18
WO_3OsLC	H_2	250	1000	72.7	0.66	82.51	8.25
WO_3OsLC	EtOH	250	5	62.8	7.2	3.41	68.12
WO_3OsLC	EtOH	250	10	73.4	4.2	3.50	35.04
WO_3OsLC	EtOH	250	15	77.8	2.8	3.34	22.29
WO_3OsLC	EtOH	250	20	78.9	2.1	3.16	15.81

WO_3OsHC	NO_2	250	0.25	-536.8	222.5	-0.03	-12.07
WO_3OsHC	NO_2	250	0.5	-3298.1	2481.5	-0.19	-37.38
WO_3OsHC	NO_2	250	0.75	-8228.1	4423.3	-0.24	-31.50
WO_3OsHC	NO_2	250	1	-12681.6	3635.6	-0.15	-15.21
WO_3OsHC	H_2	250	250	48.3	0.40	13.40	5.36
WO_3OsHC	H_2	250	500	53.0	0.38	23.26	4.65
WO_3OsHC	H_2	250	750	56.4	0.37	31.58	4.21
WO_3OsHC	H_2	250	1000	60.0	0.37	40.86	4.09
WO_3OsHC	EtOH	250	5	55.5	5.6	2.52	50.37
WO_3OsHC	EtOH	250	10	65.3	3.9	3.07	30.68
WO_3OsHC	EtOH	250	15	70.7	3.0	3.25	21.68
WO_3OsHC	EtOH	250	20	72.9	2.1	2.85	14.27

Table S2: Summary of the performance of the classification algorithms.

Number hidden layers	**Number of neurons per layer**	**Activation function**	**Accuracy training [%]**	**Accuracy test [%]**	**Working Temperature (°C)**
3	10	Tanh	93.58	93.82	150
3	10	Sigmoid	92.91	92.09	150
3	10	ReLU	91.02	86.56	150
1	10	ReLU	90.16	86.70	150
1	100	ReLU	90.06	86.78	150
1	25	ReLU	89.66	88.11	150
2	10	ReLU	89.61	91.59	150
3	10	None	81.89	81.71	150
1	100	Tanh	91.56	91.60	200
1	100	Sigmoid	91.28	91.47	200
3	10	ReLU	88.99	85.91	200
1	100	ReLU	88.99	88.61	200
1	25	ReLU	88.81	88.58	200
2	10	ReLU	88.63	88.26	200
1	10	ReLU	87.98	87.58	200
1	100	None	86.82	85.55	200
1	10	Tanh	91.61	93.18	250
1	10	ReLU	91.38	92.26	250
1	100	ReLU	91.76	92.20	250
1	25	ReLU	91.46	91.97	250
3	10	ReLU	90.23	91.45	250
1	10	Sigmoid	91.93	90.91	250
2	10	ReLU	90.29	90.82	250
1	10	None	89.69	89.45	250

Table S3: Summary of the performance of the quantification models for nitrogen dioxide.

Number hidden layers	Number of neurons per layer	Activation function	RMSE training [ppb]	R-squared training	RMSE test [ppb]	R-squared test	Working Temperature (°C)
3	10	Tanh	0.09	0.90	0.07	0.94	150
1	100	ReLU	0.10	0.88	0.09	0.90	150
3	10	ReLU	0.10	0.89	0.09	0.89	150
1	25	ReLU	0.11	0.86	0.11	0.86	150
2	10	ReLU	0.10	0.87	0.11	0.86	150
3	10	Sigmoid	0.11	0.86	0.11	0.85	150
1	10	ReLU	0.12	0.84	0.12	0.85	150
3	10	None	0.20	0.55	0.20	0.57	150
1	100	ReLU	0.12	0.87	0.11	0.89	200
3	10	ReLU	0.12	0.86	0.11	0.88	200
2	10	ReLU	0.12	0.86	0.12	0.87	200
1	25	ReLU	0.14	0.83	0.12	0.85	200
1	10	ReLU	0.15	0.81	0.13	0.84	200
1	100	Tanh	0.14	0.81	0.14	0.82	200
1	100	Sigmoid	0.16	0.78	0.15	0.80	200
1	100	None	0.20	0.66	0.19	0.67	200
3	10	ReLU	0.07	0.94	0.08	0.94	250
3	10	Tanh	0.08	0.94	0.08	0.94	250
1	100	ReLU	0.08	0.93	0.08	0.94	250
2	10	ReLU	0.08	0.93	0.08	0.94	250
1	25	ReLU	0.08	0.93	0.08	0.94	250
3	10	Sigmoid	0.09	0.92	0.08	0.93	250
1	10	ReLU	0.09	0.92	0.09	0.92	250
3	10	None	0.14	0.81	0.13	0.84	250

Table S4: Summary of the performance of the quantification models for ethanol.

Number hidden layers	Number of neurons per layer	Activation function	RMSE training [ppm]	R-squared training	RMSE test [ppm]	R-squared test	Working Temperature (°C)
1	100	Tanh	1.65	0.94	1.33	0.96	150
1	100	Sigmoid	1.67	0.94	1.58	0.94	150
1	100	ReLU	1.89	0.92	1.71	0.93	150
3	10	ReLU	1.97	0.91	1.80	0.92	150
1	25	ReLU	2.46	0.87	2.26	0.88	150
2	10	ReLU	2.03	0.91	2.28	0.88	150
1	10	ReLU	2.92	0.82	3.02	0.80	150
1	100	None	5.53	0.36	5.44	0.35	150
3	10	Sigmoid	2.01	0.92	1.27	0.96	200
3	10	ReLU	1.86	0.93	1.58	0.94	200
3	10	Tanh	2.03	0.91	1.71	0.94	200

1	100	ReLU	2.00	0.92	1.80	0.93	200
3	10	ReLU	2.00	0.92	1.85	0.93	200
1	25	ReLU	2.21	0.90	2.04	0.91	200
1	10	ReLU	2.42	0.88	2.11	0.91	200
3	10	None	5.24	0.46	5.04	0.49	200
3	10	Tanh	2.32	0.89	1.64	0.94	250
3	10	ReLU	2.48	0.88	2.04	0.91	250
1	100	ReLU	2.38	0.89	2.15	0.90	250
1	25	ReLU	2.51	0.88	2.27	0.89	250
2	10	ReLU	2.55	0.87	2.39	0.88	250
3	10	Sigmoid	2.51	0.88	2.59	0.87	250
1	10	ReLU	2.73	0.86	2.62	0.86	250
3	10	None	4.99	0.53	4.99	0.51	250

Table S5: Summary of the performance of the quantification models for hydrogen.

Number hidden layers	**Number of neurons per layer**	**Activation function**	**RMSE training [ppm]**	**R-squared training**	**RMSE test [ppm]**	**R-squared test**	**Working Temperature (°C)**
1	100	ReLU	104.33	0.90	95.81	0.91	150
2	10	ReLU	98.40	0.91	100.97	0.90	150
3	10	ReLU	97.64	0.91	105.70	0.89	150
1	25	ReLU	105.83	0.89	113.01	0.88	150
1	100	Tanh	123.15	0.86	128.10	0.84	150
1	100	Sigmoid	134.10	0.83	134.77	0.83	150
1	10	ReLU	138.01	0.82	140.21	0.81	150
1	100	None	253.72	0.41	250.01	0.42	150
1	100	ReLU	96.48	0.92	107.92	0.90	200
1	25	ReLU	108.21	0.90	112.29	0.89	200
2	10	ReLU	107.88	0.90	120.72	0.87	200
1	100	Sigmoid	104.76	0.90	120.72	0.87	200
3	10	ReLU	99.87	0.91	122.56	0.87	200
1	10	ReLU	115.44	0.88	130.57	0.85	200
1	100	Tanh	152.04	0.80	154.29	0.80	200
1	100	None	250.28	0.47	249.59	0.47	200
1	100	ReLU	76.19	0.94	85.57	0.93	250
1	100	Sigmoid	72.78	0.95	87.76	0.93	250
2	10	ReLU	74.55	0.95	91.84	0.92	250
1	25	ReLU	77.93	0.94	92.14	0.92	250
3	10	ReLU	74.79	0.95	94.41	0.92	250
1	100	Tanh	95.87	0.91	94.74	0.92	250
1	10	ReLU	79.49	0.94	95.32	0.92	250
1	100	None	255.43	0.42	259.19	0.42	250

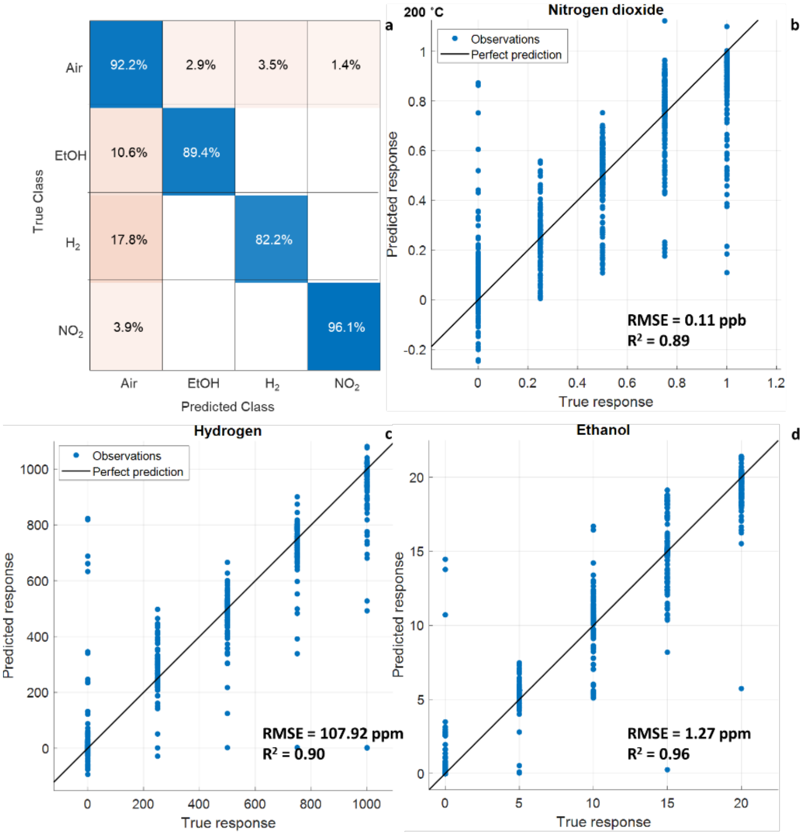

Figure S6: Results of classification and quantification models when using test dataset at 200 °C. (a) Classification. (b) NO_2 quantification. (c) H_2 quantification. (d) EtOH quantification.

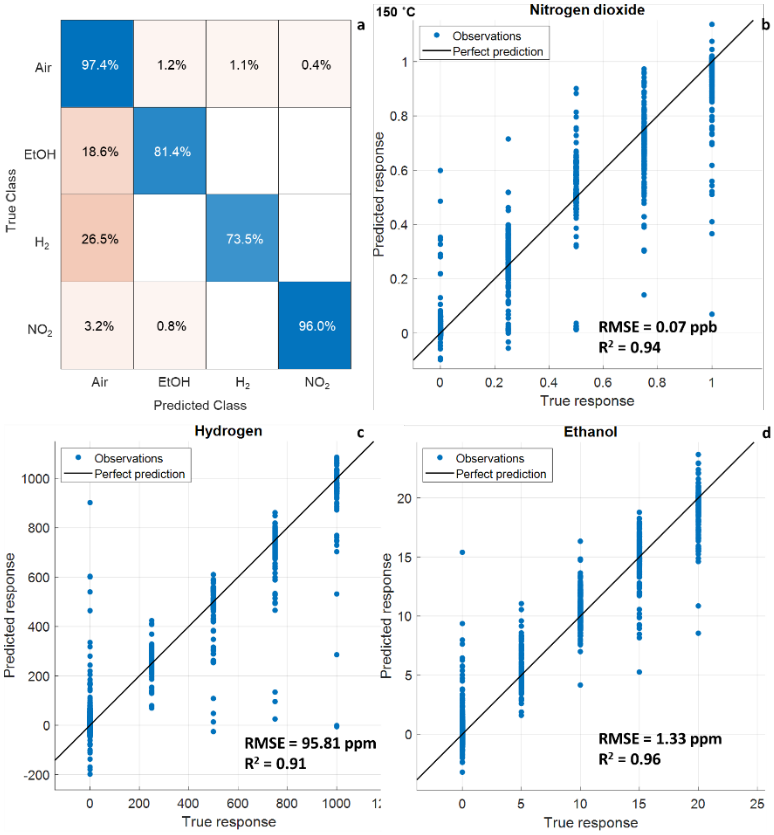

Figure S7: Results of classification and quantification models when using test dataset at 150 °C. (a) Classification. (b) NO_2 quantification. (c) H_2 quantification. (d) EtOH quantification.

Table S6: Relationship between classification accuracy and working temperature of the sensors.

Working Temperature (°C)	**Classifying NO_2 (%)**	**Classifying EtOH (%)**	**Classifying H_2 (%)**
150	96.0	81.4	73.5
200	96.1	89.4	82.2
250	95.2	90.1	86.9

Table S7: Summary of the best quantification models for EtOH, NO_2, and H_2 at three temperatures.

Gas	**Temperature [°C]**	**RMSE train [ppm]**	**R-squared train**	**RMSE test [ppm]**	**R-squared test**
EtOH	150	1.65	0.94	1.33	0.96
	200	2.01	0.92	1.27	0.96
	250	2.32	0.89	1.64	0.94
NO_2	150	0.09×10^{-3}	0.90	0.07×10^{-3}	0.94
	200	0.12×10^{-3}	0.87	0.11×10^{-3}	0.89
	250	0.07×10^{-3}	0.94	0.08×10^{-3}	0.94
H_2	150	104.33	0.90	95.81	0.91
	200	96.48	0.92	107.92	0.90
	250	76.19	0.94	85.57	0.93

Table S8: Comparative between gas-sensing application metrics found in the literature and metrics of this work [1].

Algorithm	**Application**	**Metrics**	Ref.
SVM	Drift compensation, Classification	Accuracy: 89.98 % – 96.62 %	[2,3]
ANN	Classification	Accuracy: 91.26%	[2]
XGBoost	Classification	Accuracy: 96.62 % Sensitivity: 95.60 %	[2,4]
KNN	Drift compensation	Accuracy: 80.74 % – 97.5 %	[2,5,6]
KNN-ANN	Drift suppressed classification	Accuracy: 96.51 %	[7]
PLS	Gas concentration prediction	RMSE: 7.34	[8,9]
ACNN	Drift compensation	Accuracy increased over 30% worst case	[10]
MLPNN	Gas concentration estimation	Error decreased 7 % – 19 % worst case	[11]
Deep CNN	Real-time classification	Accuracy: 98.1 %	[12]
CNN ensemble	Classification	Accuracy: 99.72 %	[13]
PCA and ANN	Discrimination and Quantification	Accuracy: 96.1 % * R-squared: 0.96 * RMSE: 0.07 ppb *	This work

*Best case

References

1. Md. S. I. Sagar, N. R. Allison, H. M. Jalajamony, R. E. Fernandez and P. K. Sekhar, J Electrochem Soc, 2022, 169, 127512.
2. T. Matthews, M. Iqbal and H. Gonzalez-Velez, in 2018 IEEE/ACM 5th International Conference on Big Data Computing Applications and Technologies (BDCAT), IEEE, 2018, pp. 61–70.
3. T. Liu, D. Li, J. Chen, M. Wu and Y. Chen, in 2018 5th International Conference on Systems and Informatics (ICSAI), IEEE, 2018, pp. 417–423.
4. K. Chen, L. Liu, B. Nie, B. Lu, L. Fu, Z. He, W. Li, X. Pi and H. Liu, Comput Biol Med, 2021, 131, 104294.
5. C. Deng, K. Lv, D. Shi, B. Yang, S. Yu, Z. He and J. Yan, Sensors, 2018, 18, 1909.
6. Z. Jiang, P. Xu, Y. Du, F. Yuan and K. Song, Sensors, 2021, 21, 3403.
7. M. Abbatangelo, E. Núñez-Carmona, V. Sberveglieri, E. Comini and G. Sberveglieri, Chemosensors, 2020, 8, 6.
8. L. Wozniak, P. Kalinowski, G. Jasinski and P. Jasinski, Microelectronics Reliability, 2018, 84, 163–169.
9. J. Burgués, M. D. Esclapez, S. Doñate and S. Marco, iScience, 2021, 24, 103371.
10. L. Feng, H. Dai, X. Song, J. Liu and X. Mei, Sens Actuators B Chem, 2022, 351, 130986.
11. J. Wang, S. Lian, B. Lei, B. Li and S. Lei, Sens Actuators A Phys, 2022, 335, 113392.
12. M. Kang, I. Cho, J. Park, J. Jeong, K. Lee, B. Lee, D. Del Orbe Henriquez, K. Yoon and I. Park, ACS Sens, 2022, 7, 430–440.
13. S. Chaudhri and N. Rajput, IEEE Sens Lett, 2022, 6, 1–4.

Supplementary Material Chapter 3

IoT platform enhanced with neural network for air pollutant monitoring

Alejandro Santos-Betancourt, José Carlos Santos-Ceballos, Foad Salehnia, Mohamed Ayoub Alouani, Alfonso Romero, José Luis Ramírez, and Xavier Vilanova

MINOS, DEEEA, Universitat Rovira i Virgili, Tarragona, Spain.

IU-RESCAT, Research Institute in Sustainability, Climatic Change and Energy Transition, Universitat Rovira i Virgili, Vilaseca, Spain.

Centre for Environmental, Food and Toxicological Technology (TecnATox), Universitat Rovira i Virgili, Tarragona, Spain.

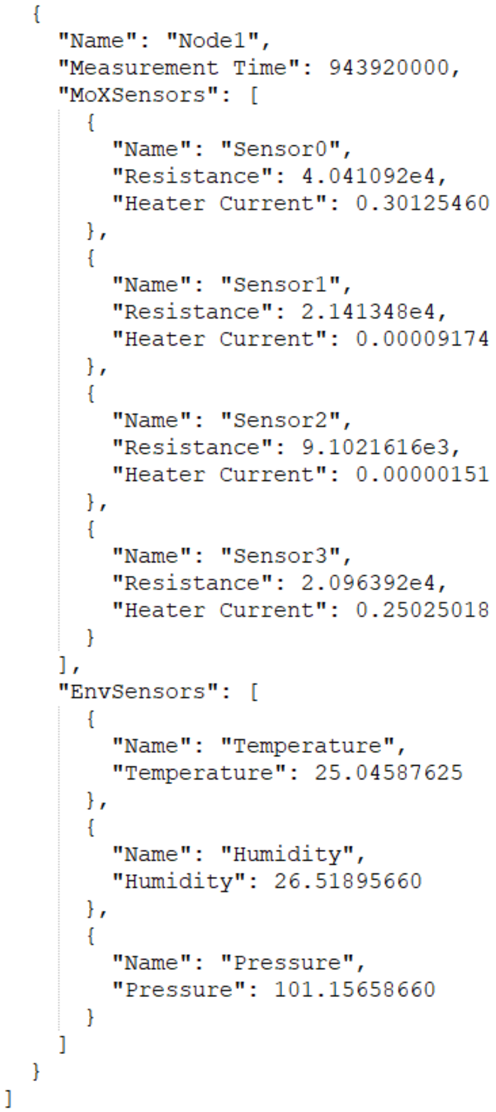

```
    {
      "Name": "Node1",
      "Measurement Time": 943920000,
      "MoXSensors": [
        {
          "Name": "Sensor0",
          "Resistance": 4.041092e4,
          "Heater Current": 0.30125460
        },
        {
          "Name": "Sensor1",
          "Resistance": 2.141348e4,
          "Heater Current": 0.00009174
        },
        {
          "Name": "Sensor2",
          "Resistance": 9.1021616e3,
          "Heater Current": 0.00000151
        },
        {
          "Name": "Sensor3",
          "Resistance": 2.096392e4,
          "Heater Current": 0.25025018
        }
      ],
      "EnvSensors": [
        {
          "Name": "Temperature",
          "Temperature": 25.04587625
        },
        {
          "Name": "Humidity",
          "Humidity": 26.51895660
        },
        {
          "Name": "Pressure",
          "Pressure": 101.15658660
        }
      ]
    }
  ]
```

Fig. S1: JSON format for the communication protocol between gas sensor nodes, the server, and the user interface.

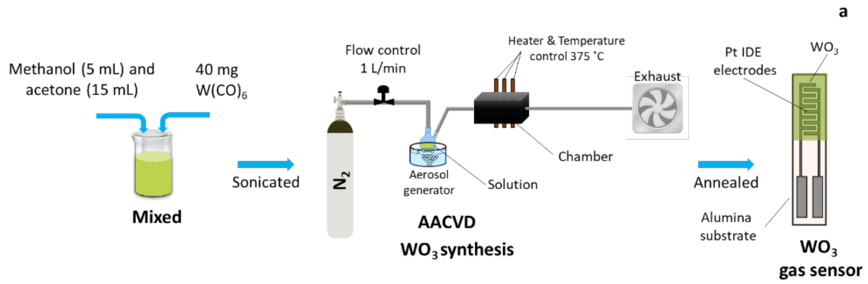

Fig. S2: Schematic of the fabrication process of chemoresistor gas sensors based on tungsten trioxide using aerosol-assisted chemical vapor deposition (AACVD).

Sensors of tungsten trioxide were fabricated using an aerosol-assisted chemical vapor deposition system (AA-CVD). The nanomaterial was grown on top of commercial alumina substrates. The substrate held interdigitated electrodes (300 μm gap) on the top side and an 8 Ω heating element on the bottom. The electrodes and the heater are made of platinum and screen-printed to an alumina substrate (CeramTec GmbH, Plochingen, Germany). The synthesis of pristine tungsten trioxide was done employing 40 mg of tungsten hexacarbonyl as a precursor. Such precursor was solubilized in a mixture of methanol and acetone with a 1:3 vol ratio (5 mL and 15 mL respectively). The solution was sonicated until all the precursor material was fully solved (around 15 minutes) and then, placed in an aerosol generator, which used a bath and ultrasonic waves to convert the solution into a micro-droplet spray that contained the precursor. This spray is given via a connecting pipe system using nitrogen as an inert carrier gas at a constant flow of 1 $\mathrm{Lmin^{-1}}$ towards a preheated CVD hot-wall reactor at 375 °C. The resulting tungsten trioxide layers fully coat the electrodes. Typically, some amorphous carbon residues are left by the organic precursor and solvents. To remove such impurities and enhance oxidation, an annealing process is performed right after the deposition, which is conducted in a muffle furnace (Carbolite CWF 1200, Carbolite Gero Ltd., Neuhausen, Germany) at 500 °C for 2 hours, with a temperature ramp of 5 $^{\circ}\mathrm{Cmin^{-1}}$, under pure dry air. Figure S2 describes the schematic of the process. A similar fabrication procedure was previously reported by our research group [1,2].

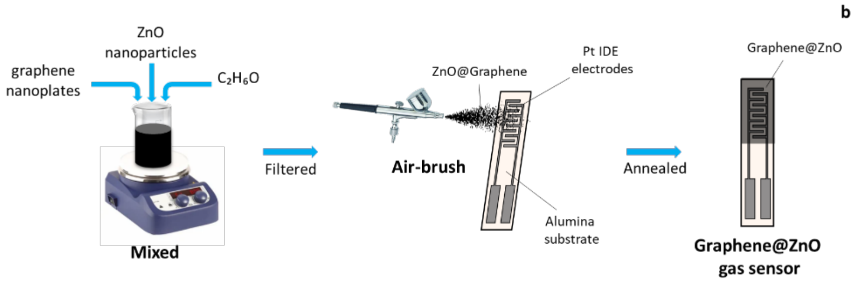

Fig. S3: Schematic of the fabrication process of chemoresistor gas sensors based on graphene decorated with zinc oxide using airbrush.

Graphene decorated with zinc oxide (Graphene@ZnO) sensors were fabricated using the airbrush technique. Figure S3 presents a general description of the fabrication process: graphene nanoplatelets and 5 wt.% zinc oxide nanoparticles were mixed under magnetic stirring for 30 min, using ethanol (Scharlab, Sentmenat, Spain, CAS: 64-17-5) as a solvent. Later, the solution was filtered using filter paper and treated under a microwave at a power of 1000 W for about 5 min. Extensive details of the synthesis of this hybrid/composite are given in our previous work [3]. The deposition was performed on the same alumina substrate used for the tungsten trioxide sensors mentioned above. Finally, a solution of 10 mL of ethanol mixed with 1 mg of powder under magnetic stirring for half an hour was prepared to be airbrushed onto the interdigitated electrodes (IDEs) using a DISMOER airbrush tool.

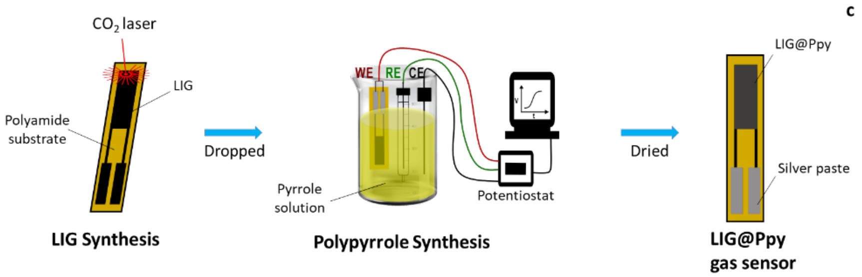

Fig. S4: Schematic of the fabrication process of chemoresistor gas sensors based on laser-induced graphene decorated with polypyrrole.

The second type of graphene-based sensors was fabricated using laser-induced graphene (LIG). The fabrication process of LIG decorated with polypyrrole (LIG@Ppy) sensors involves two main steps. First, the fabrication of the LIG electrode employing a commercially available polyimide film (50 µm thick) as a substrate, Figure S4 LIG was synthesized using a CO_2 laser system (SYNRARD 48–2) with a wavelength of 10.6 µm, a max power of 25 W, and a lens with a focal length of 74 mm. The laser beam scanned over the polyimide surface at a speed of 200 mm/s, frequency of 12 kHz, and 12 % laser power. The sensor has been designed with a sensing area of 18 mm^2. Silver ink was drop-casted on the electrodes to improve the connection of the sensor with the measurement system. In the second step, the electrochemical growth of Ppy on the LIG was carried out using a potentiostat (pocketSTAT2, IVIUM Technologies). A 3-electrode system involving of LIG electrode as a working electrode, a platinum wire auxiliary electrode, and an Ag/AgCl reference electrode with a salt bridge containing aqueous 3 M NaCl was used for experiments. The concentration of pyrrole in polymerization solutions was 0.25 mM, and the electrolyte for synthesis consisted of 0.5 mM tetrabutylammonium perchlorate in acetonitrile. The Ppy synthesis was prepared by chronoamperometry method using a constant potential of 1.2 V for 10 min. Details of the synthesis of this material are given in our previous work [4,5].

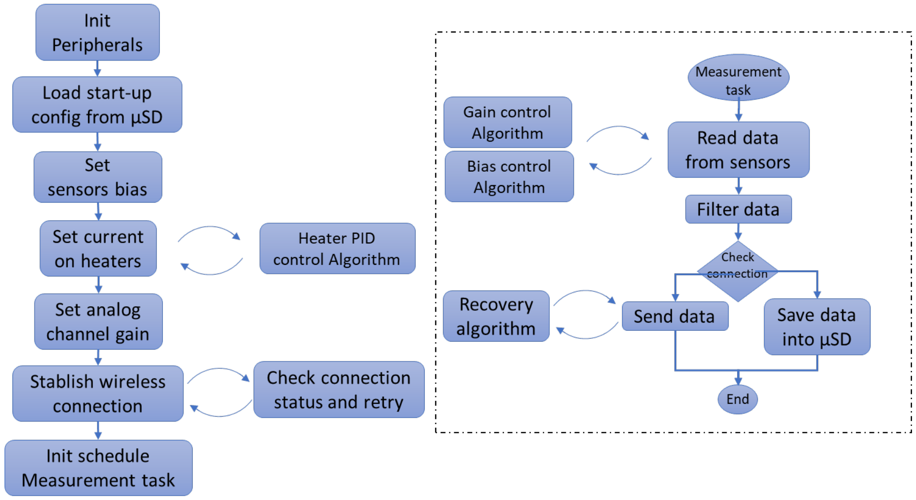

Figure S5: Flow diagram of the software.

Note S1: Model to simulate how the target gas goes into the chamber.

The mass balance equation was used to simulate how the concentration of the target gas increases inside the chamber.

First assumptions: at steady state, the gas inside the chamber is perfectly mixed; the gas outflow rate is constant and equal to the inflow rate; the concentration of the incoming gas is constant.

Mass balance equation [6]: $$\frac{dC(t)}{dt} + \frac{Fk}{V}C(t) = \frac{Fk}{V}C_{in}$$

where: V is the measured volume of the chamber. F is the inflow to the chamber. C_{in} is the ammonia concentration in the incoming gas. $C(t)$ is the ammonia concentration in the chamber at time t. *k is a constant that depends on restrictions such as the valve coefficient, pipe friction factor, etc.*

Laplace transform: $$L\left\{\frac{dC(t)}{dt}\right\} = L\left\{\frac{Fk}{V}(C_{in} - C(t))\right\}$$

$$sC(s) - C(0) = \frac{Fk}{V}\left(C_{in}\frac{1}{s} - C(s)\right)$$

Distribute, collect terms, and factor out on left hand-side:

$$C(s) = \frac{FkC_{in}}{Vs(s+\frac{Fk}{V})} + \frac{C(0)}{s+\frac{Fk}{V}}$$

where: C(0) is the initial concentration of the target gas inside the chamber.

Second assumptions: C(0) = 0 and the response of the system can be dominated by the slowest pole which is: $s + \frac{Fk}{V}$ [7]:

$$C(s) = \frac{1}{Ts+1}C_{in}$$

where: $T = \frac{V}{Fk}$

The output of this transfer function was used to simulate the gas concentration inside the chamber. Also, it was used as a Response signal (Y) for training the quantification models.

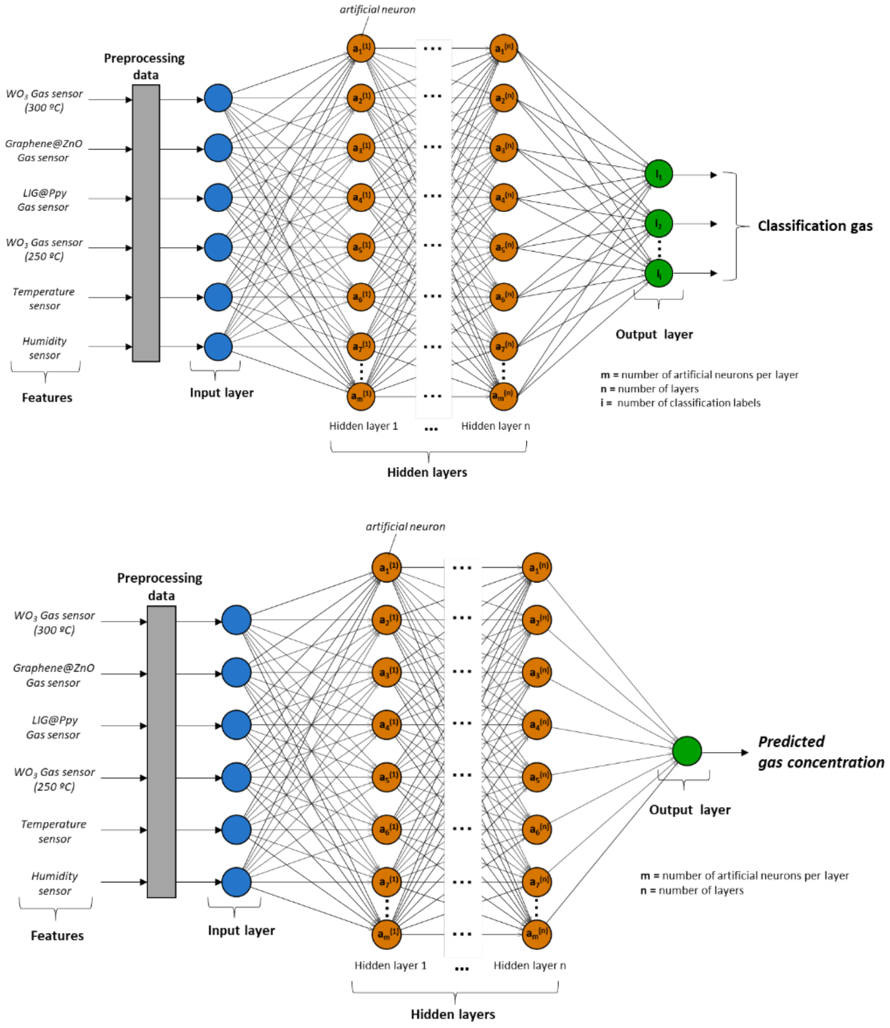

Fig. S6: Structure of the model using ANNs. (upper) Classification. (lower) Regression.

Table S1: Performance of the classification MLPs.

Number hidden layers	**Number of neurons per layer**	**Activation function**	**Removed features**	**Accuracy train [%]**	**Accuracy test [%]**
1	10	ReLU	-	94.1	94.3
1	25	ReLU	-	96.5	96.7
1	100	ReLU	-	98.0	98.0
2	10	ReLU	-	95.3	93.1
3	10	ReLU	-	95.1	95.6
1	100	Sigmoid	-	98.5	98.7
1	**100**	**Tanh**	**-**	**98.6**	**98.7**
1	100	Tanh	Temperature, Humidity	97.6	97.4
1	100	Tanh	LIG@Ppy, Graphene@ZnO	95.9	96.2

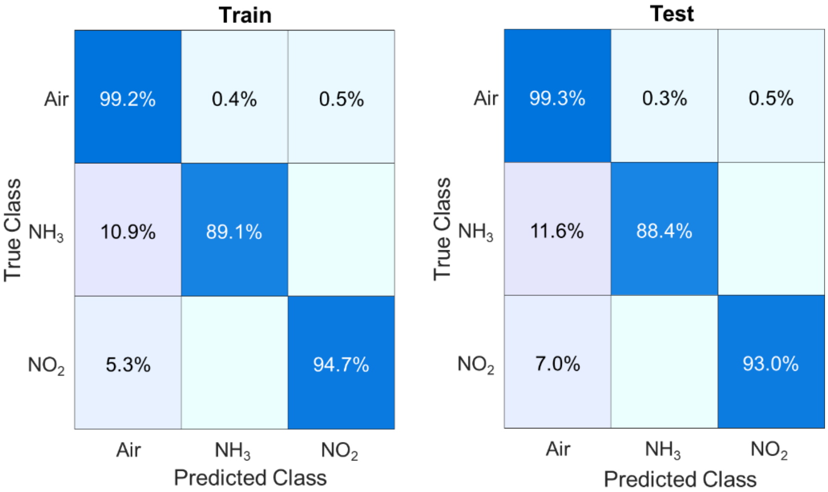

Fig. S7: Confusion matrix removing features related to humidity and temperature. (left) train data. (right) test data.

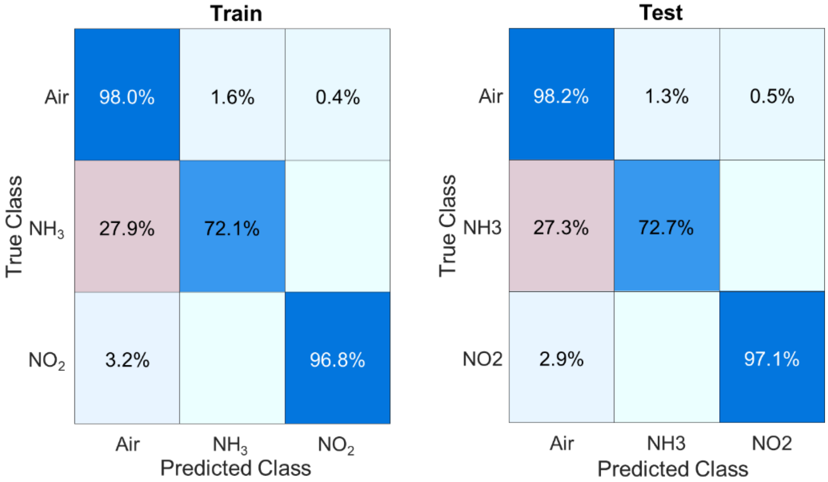

Fig. S8: Confusion matrix removing features related to graphene-based sensors. (left) train data. (right) test data.

Table S2: Performance of the quantification MLPs for nitrogen dioxide.

Number hidden layers	**Number of neurons per layer**	**Activation function**	**Removed features**	**RMSE train [ppb]**	**R2 train**	**RMSE test [ppb]**	**R2 test**
1	10	ReLU	-	70.80	0.61	60.79	0.72
1	25	ReLU	-	49.18	0.81	44.54	0.85
1	**100**	**ReLU**	**-**	**28.13**	**0.93**	**27.43**	**0.94**
2	10	ReLU	-	39.76	0.87	37.21	0.89
3	10	ReLU	-	37.70	0.89	36.59	0.90
1	100	Sigmoid	-	39.25	0.88	38.38	0.89
1	100	Tanh	-	47.99	0.82	56.01	0.76
1	100	ReLU	Temperature, Humidity	51.56	0.79	50.47	0.81
1	100	ReLU	LIG@Ppy, Graphene@ZnO	43.62	0.85	45.06	0.85

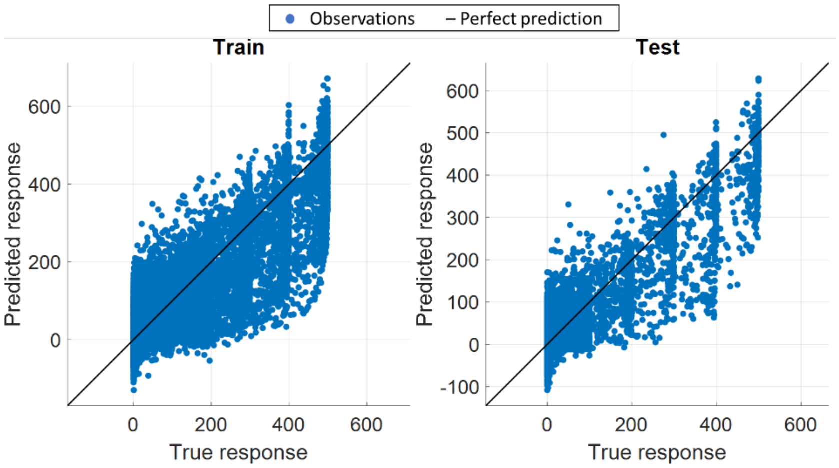

Fig. S9: Prediction chart of nitrogen dioxide removing features related to humidity and temperature. (left) train data: RMSE = 43.62 ppb, $R^2 = 0.85$. (right) test data: RMSE = 50.47 ppb, $R^2 = 0.81$.

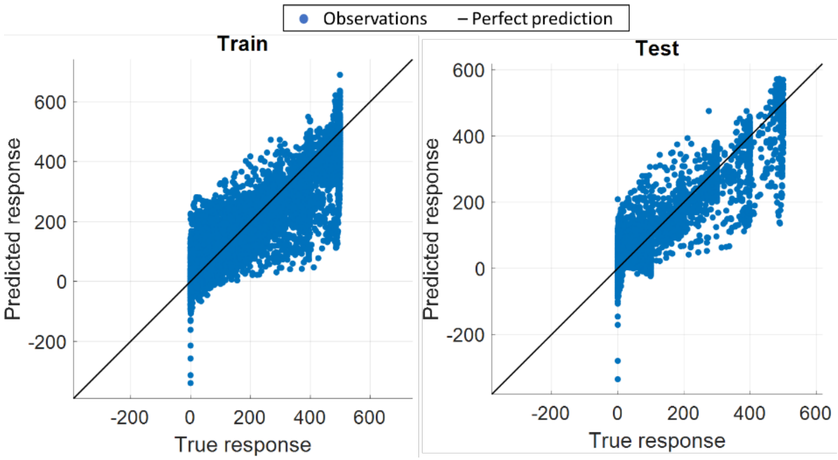

Fig. S10: Prediction chart of nitrogen dioxide removing features related to graphene-based sensors. (left) train data: RMSE = 51.76 ppb, $R^2 = 0.79$. (right) test data: RMSE = 45.06 ppb, $R^2 = 0.85$.

Table S3: Performance of the quantification MLPs for ammonia.

Number hidden layers	Number of neurons per layer	Activation function	Removed features	RMSE train [ppm]	R2 train	RMSE test [ppm]	R2 test
1	10	ReLU	-	2.49	0.93	2.35	0.94
1	25	ReLU	-	2.01	0.95	1.99	0.96
1	100	ReLU	-	1.78	0.96	1.59	0.97
2	10	ReLU	-	1.81	0.96	1.61	0.97
3	10	ReLU	-	1.69	0.96	1.69	0.97
1	**100**	**Sigmoid**	**-**	**1.49**	**0.97**	**1.39**	**0.98**
1	100	Tanh	-	1.65	0.97	1.39	0.98
1	100	Sigmoid	Temperature, Humidity	1.86	0.96	1.88	0.96
1	100	Sigmoid	LIG@Ppy, Graphene@ZnO	3.14	0.89	3.29	0.89

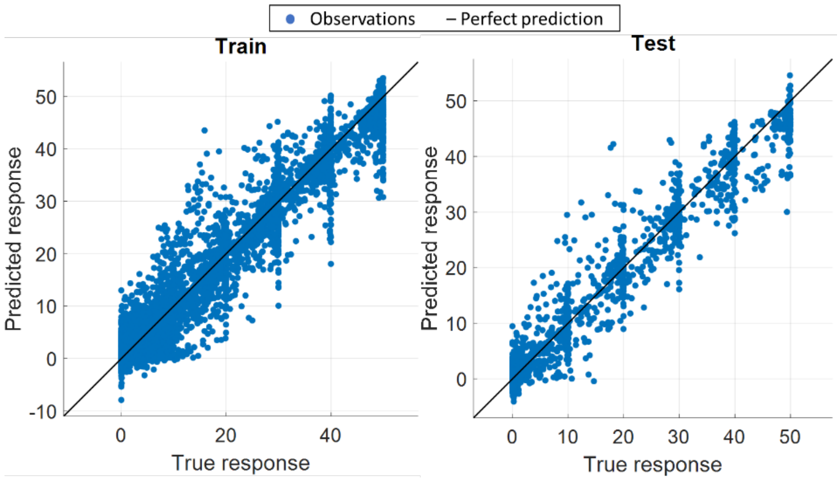

Fig. S11: Prediction chart of ammonia removing features related to humidity and temperature. (left) train data: RMSE = 1.86 ppm, $R^2 = 0.96$. (right) test data: RMSE = 1.88 ppm, $R^2 = 0.96$.

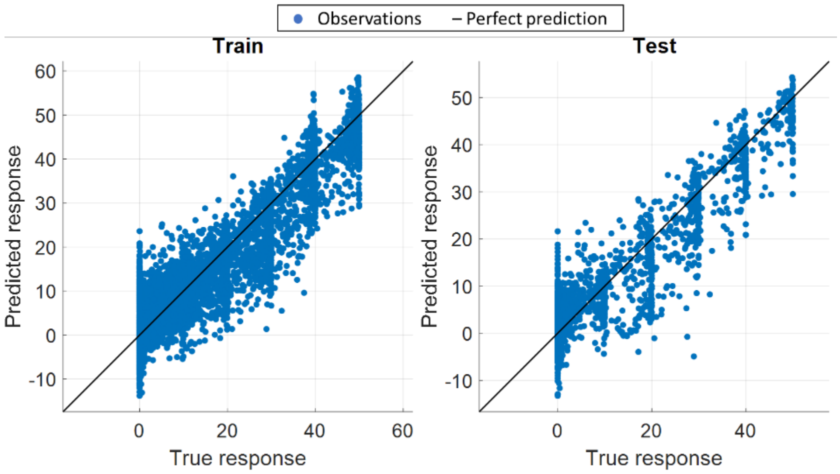

Fig. S12: Prediction chart of ammonia removing features related to graphene-based sensors. (left) train data: RMSE = 3.14 ppm, $R^2 = 0.89$. (right) test data: RMSE = 3.29 ppm, $R^2 = 0.89$.

Table S4: Performance of the classification MLPs under a mixture of gases.

Number hidden layers	**Number of neurons per layer**	**Activation function**	**Removed features**	**Accuracy train [%]**	**Accuracy test [%]**
1	10	ReLU	-	91.3	88.9
1	25	ReLU	-	97.6	97.5
1	100	ReLU	-	99.0	98.9
2	10	ReLU	-	95.9	94.6
3	10	ReLU	-	96.7	98.0
1	100	Sigmoid	-	99.3	99.3
1	**100**	**Tanh**	**-**	**99.3**	**99.2**
1	100	Tanh	Temperature, Humidity	98.3	98.0
1	100	Tanh	LIG@Ppy, Graphene@ZnO	97.9	98.1

Table S5: Performance of the quantification MLPs for nitrogen dioxide under a mixture.

Number hidden layers	**Number of neurons per layer**	**Activation function**	**Removed features**	**RMSE train [ppb]**	**R2 train**	**RMSE test [ppb]**	**R2 test**
1	10	ReLU	-	48.56	0.80	47.75	0.79
1	25	ReLU	-	36.48	0.88	37.36	0.877
1	**100**	**ReLU**	**-**	**19.97**	**0.96**	**19.15**	**0.96**
2	10	ReLU	-	36.54	0.88	29.66	0.92
3	10	ReLU	-	28.58	0.93	22.35	0.95
1	100	Sigmoid	-	27.83	0.93	25.94	0.94
1	100	Tanh	-	42.82	0.84	34.45	0.89
1	100	ReLU	Temperature, Humidity	49.94	0.79	46.62	0.80
1	100	ReLU	LIG@Ppy, Graphene@ZnO	63.60	0.66	57.33	0.71

Table S6: Performance of the quantification MLPs for ammonia under a mixture.

Number hidden layers	**Number of neurons per layer**	**Activation function**	**Removed features**	**RMSE train [ppm]**	**R2 train**	**RMSE test [ppm]**	**R2 test**
1	10	ReLU	-	6.95	0.82	7.23	0.80
1	25	ReLU	-	4.90	0.91	4.86	0.91
1	100	ReLU	-	2.47	0.97	2.54	0.97
2	10	ReLU	-	4.89	0.91	5.44	0.89
3	10	ReLU	-	3.77	0.94	3.40	0.95
1	**100**	**Sigmoid**	**-**	**1.74**	**0.98**	**1.84**	**0.98**
1	100	Tanh	-	2.33	0.98	1.99	0.98
1	100	Sigmoid	Temperature, Humidity	5.25	0.89	4.84	0.91
1	100	Sigmoid	LIG@Ppy, Graphene@ZnO	5.17	0.90	5.04	0.90

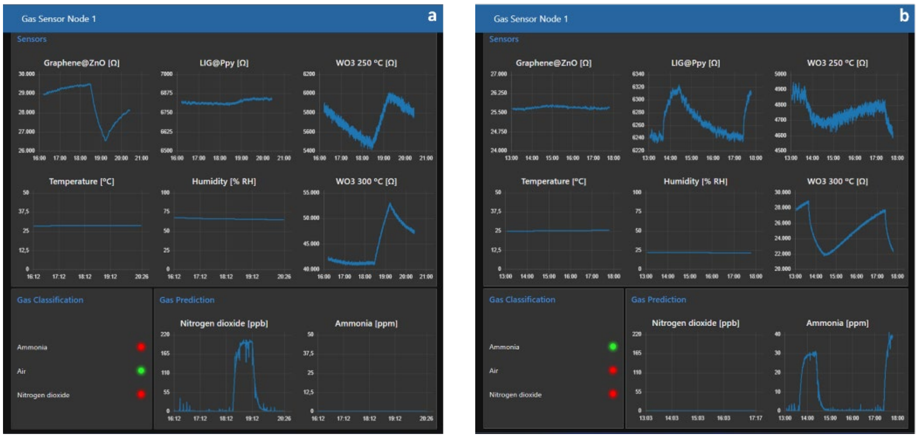

Fig. S13: Screenshot of the user interface. (a) 200 ppb pulse of nitrogen dioxide. (b) 40 ppm pulse of ammonia.

REFERENCES

1. Navarrete, E.; Bittencourt, C.; Umek, P.; Llobet, E. AACVD and Gas Sensing Properties of Nickel Oxide Nanoparticle Decorated Tungsten Oxide Nanowires. J Mater Chem C Mater 2018, 6, 5181–5192, doi:10.1039/C8TC00571K.

2. Navarrete, È.; Bittencourt, C.; Noirfalise, X.; Umek, P.; González, E.; Güell, F.; Llobet, E. WO3 Nanowires Loaded with Cobalt Oxide Nanoparticles, Deposited by a Two-Step AACVD for Gas Sensing Applications. Sens Actuators B Chem 2019, 298, 126868, doi:10.1016/j.snb.2019.126868.

3. Santos-Betancourt, A.; Santos-Ceballos, J.C.; Alouani, M.A.; Malik, S.B.; Romero, A.; Ramírez, J.L.; Vilanova, X.; Llobet, E. ZnO Decorated Graphene-Based NFC Tag for Personal NO2 Exposure Monitoring during a Workday. Sensors 2024, 24, 1431, doi:10.3390/s24051431.

4. Santos-Ceballos, J.C.; Salehnia, F.; Romero, A.; Vilanova, X.; Llobet, E. Low Cost, Flexible, Room Temperature Gas Sensor: Polypyrrole-Modified Laser-Induced Graphene for Ammonia Detection. IEEE Sens J 2024, 24, 9366–9374, doi:10.1109/JSEN.2024.3368658.

5. Santos-Ceballos, J.C.; Salehnia, F.; Romero, A.; Vilanova, X. Flexible Sensor Utilizing Polypyrrole Laser-Induced Graphene Nanocomposite for Room Temperature Ammonia Detection. In Proceedings of the 2023 IEEE SENSORS; IEEE, October 29 2023; pp. 01–04.

6. Laussmann, D.; Helm, D. Air Change Measurements Using Tracer Gases: Methods and Results. Significance of Air Change for Indoor Air Quality. In Chemistry, Emission Control, Radioactive Pollution and Indoor Air Quality; InTech, 2011.

7. Ogata, K. Control Systems Analysis in State Space. Modern Control Engineering 2010.

Supplementary Material Chapter 4

ZnO decorated Graphene-based NFC tag for personal NO_2 exposure monitoring during a workday

Alejandro Santos Betancourt [1], José C. Santos-Ceballos [1], Mohamed Ayoub Alouani [1], Shuja Bashir Malik [1], Alfonso J. Romero [1], José L. Ramírez [1], Xavier Vilanova [1]* and Eduard Llobet [1]

1- Universitat Rovira i Virgili, MINOS, Països Catalans, 26 Tarragona, Catalunya 43007, Spain;

* xavier.vilanova@urv.cat

Table S1: Comparison of graphene-based gas sensors for NO_2 detection at room temperature.

Material	Concentration (ppm)	Response %	Response Time (seconds)	Recovery Time (seconds)	Ref.
Co_3O_4-rGO	5	26.8	90	2400	[1]
rGO/ZnO-CT and ET	15	44	140	630	[2]
All graphene	5	12	328	1941	[3]
rGO/Ag nanowires	50	20	162	1200	[4]
Ag-S-RGO	50	75	12	20	[5]
RGO/Cu_2O	2	60	N/A	N/A	[6]
ZnS NPs/N-rGO	10	2.2	N/A	724	[7]
Graphene:ZnO	0.5	5.1	N/A	N/A	[8]
ZnO/SnO_2-rGO	5	141.0	32	92	[9]
ZnO/graphene aerogel	50	3.6	132	164	[10]
rGO/ZnO flowers and nanoparticles	1.5	1.4	394	807	[11]
rGO/ZnO laser modified	5	6.2	100	200	[12]
rGO/ZnO nanorods	100	17.4	780	1980	[13]
Graphene:ZnO NF	1	20.24	600	2820	This work
Graphene:ZnO NP	1	19.59	600	2940	This work

Table S2: Comparison of wearable NFC gas sensors on a flexible substrate.

Target gas	**Active material**	**Sensing range**	**Sensitivity**	**Average Power consumption**	**Chip**	**Battery**	**Substrate**	**Weight**	**Ref**
NH_3	Ag - rGO	5–100 ppm	1.25 %	N/A	no	no	PET	N/A	[14]
DCP	BMIMCl/ HFIPN/ SWCNT	0.028–2.4 ppm	N/A	N/A	no	no	PET	N/A	[15]
NH_3	Cellulose fiber	0.2–1000 ppm	N/A	N/A	yes	no	Cellulose paper	N/A	[16]
NH_3	PTS–PANi	5–200 ppm	45 % ppm^{-1}	N/A	no	no	PET	N/A	[17]
Cadaverine	PTS–PANi	5 – 40 ppm	4.25 % ppm^{-1}	N/A	no	no	PET	N/A	[17]
Putrescine	PTS–PANi	5 – 40 ppm	9.2 % ppm^{-1}	N/A	no	no	PET	N/A	[17]
O_2	P4VP–SWCNTs–FeII	2 – 21 %	N/A	N/A	no	no	PET	N/A	[18]
CO_2	La_2O_2S:Eu/ N/TMAOH/	up to 50,000 ppm	N/A	4.45 mW	yes	no	PET	N/A	[19]
Ethylene	SnO_2	100 – 500 ppm	N/A	N/A	yes	no	PET	N/A	[20]
O_2, CO_2; NH_3	*	0.05 – 2 %, < 60 %, tens of ppm	N/A	8.5 mW	yes	no	PEN	N/A	[21]
NO_2	Graphene: ZnO	Up to 1 ppm	3 % ppm^{-1}	24.9 µW	yes	yes	PI	0.706 grams **	This work

* See reference for details

** The weight of the battery should be added to this quantity. (Ex: using a CR2032 battery, the total weight is around 4.5 grams)

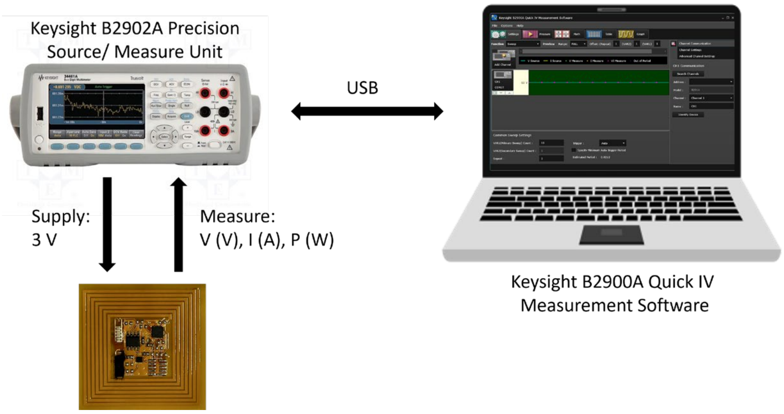

Figure S1: Test bench of the power consumption measurement.

The power consumption of the wearable NFC tag system was measured using Keysight B2902A Precision Source/ Measure Unit. The wearable was sourced with 3 V (according to the power source specification in the electronic design) and the level of voltage, current, and power were acquired using the Software Quick IV Measurement version 4.1.1821.368 from Keysight Technologies. Ten-minute tests were conducted several times observing the system commuting between power modes (Deep Power Down Mode and RTC Wake Up). Similarly, the tests were repeated but reading a few times the data from the wearable with a smartphone running the test Android application. The resultant data was exported to MATLAB R2022b, plotted, and analyzed. As a result, the average power consumption in each section was: around 1.5 mW when reading the sensors every 60 seconds, around 1.25 mW when the device interacts with the NFC field to send the data from the sensor to the NFC reader, and around 3 μW when the device is in DPDM. This ultra-low power consumption value is consistent with the values reported by the manufacturer of the SoC NHS3152 and the DC-DC NCP705 in off mode.

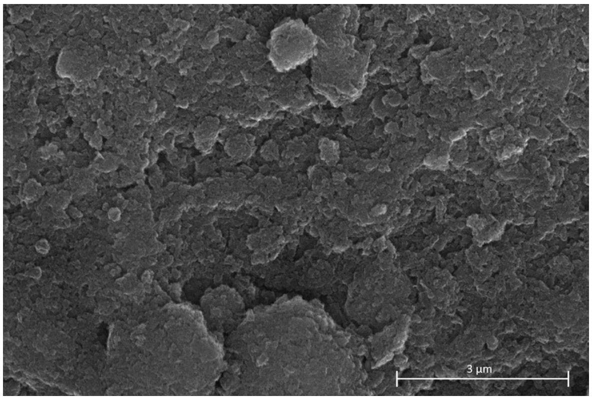

Figure S2: FESEM image using Back-scattered electron detector of bare graphene.

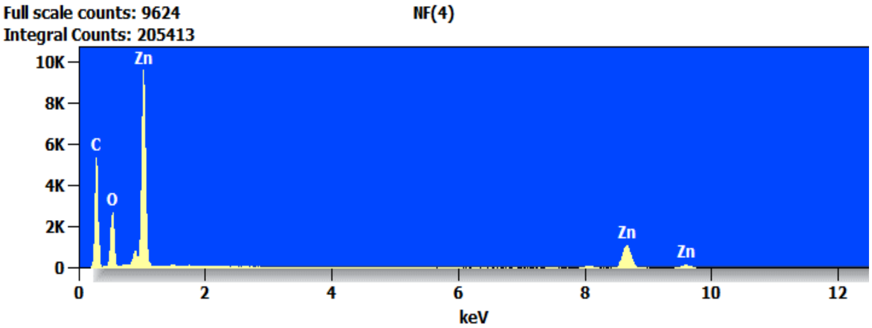

Figure S3: EDX of the nanoflowers sample

Live Time: 40.0 sec.

Wed Nov 29 14:35:01 2023

Filter Fit Chi Squared:22.666

Errors: +/- 1 Sigma

Correction Method: Proza (Phi-Rho-Z)

Acc.Voltage: 20.0 kV Take Off Angle: 35.0 deg.

Quantitative Results for: NF(4)

Element	*Weight %*	*Weight % Error*	*Norm. Wt.%*	*Atom %*	*Formula*
C	38.29	± 0.22	38.29	58.55	C
O	27.82	± 0.29	27.82	31.94	O
Zn	33.89	± 0.46	33.89	9.52	Zn
Total	100.00		100.00	100.00	

A higher amount of Zn can be seen because the EDX was performed on top of the nanoflower. Details are indicated in its corresponding FESEM image (Figure 4 (b) of the principal document).

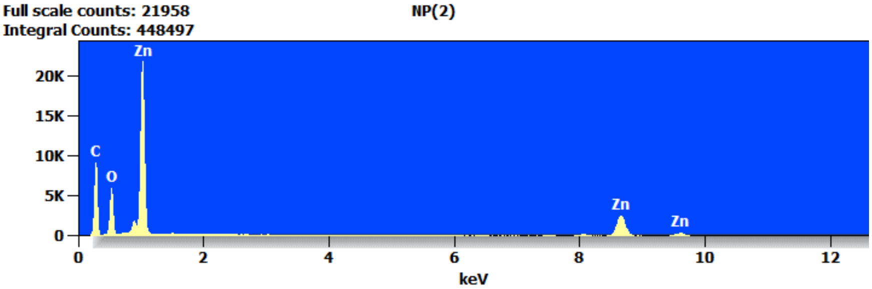

Figure S4: EDX of the nanopillars sample

Live Time: 40.0 sec.

Wed Nov 29 14:49:51 2023

Filter Fit Chi Squared:43.982

Errors: +/- 1 Sigma

Correction Method: Proza (Phi-Rho-Z)

Acc.Voltage: 20.0 kV Take Off Angle: 34.4 deg.

Quantitative Results for: NP(2)

Element	*Weight %*	*Weight % Error*	*Norm. Wt.%*	*Atom %*	*Formula*
C	34.66	± 0.18	34.66	55.17	C
O	28.50	± 0.22	28.50	34.05	O
Zn	36.84	± 0.33	36.84	10.77	Zn
Total	100.00		100.00	100.00	

A higher amount of Zn can be seen because the EDX was performed on top of the nanopillars. Details are indicated in its corresponding FESEM image (Figure 4 (a) of the principal document).

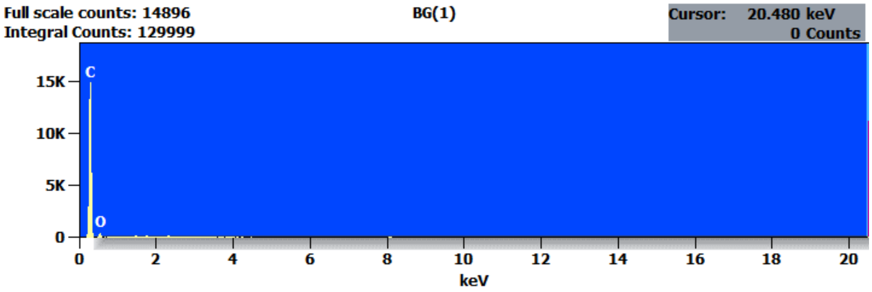

Figure S5: EDX of the bare graphene.

Live Time: 40.0 sec.

Wed Nov 29 14:59:29 2023

Filter Fit   Chi Squared:330.665

Errors: +/- 1 Sigma

Correction Method: Proza (Phi-Rho-Z)

Acc.Voltage: 20.0 kV Take Off Angle: 35.8 deg.

Quantitative Results for: BG(1)

Element	*Weight %*	*Weight % Error*	*Norm. Wt.%*	*Atom %*	*Formula*
C	80.84	± 0.39	80.84	84.89	C
O	19.16	± 0.54	19.16	15.11	O
Total	100.00		100.00	100.00	

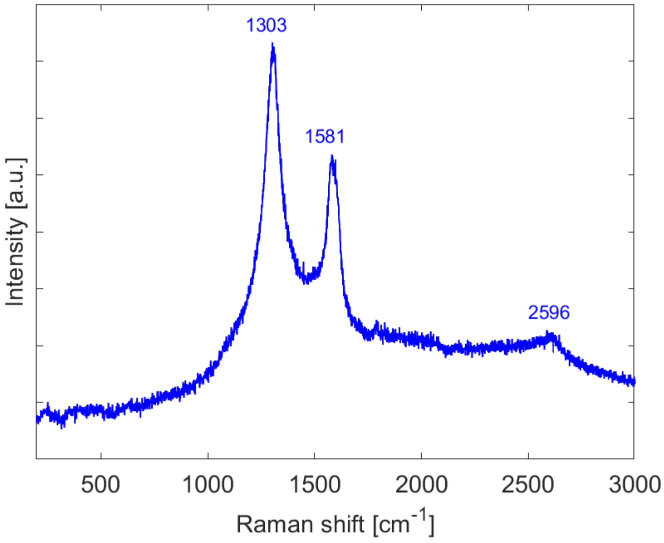

Figure S6: Raman spectroscopy of bare graphene.

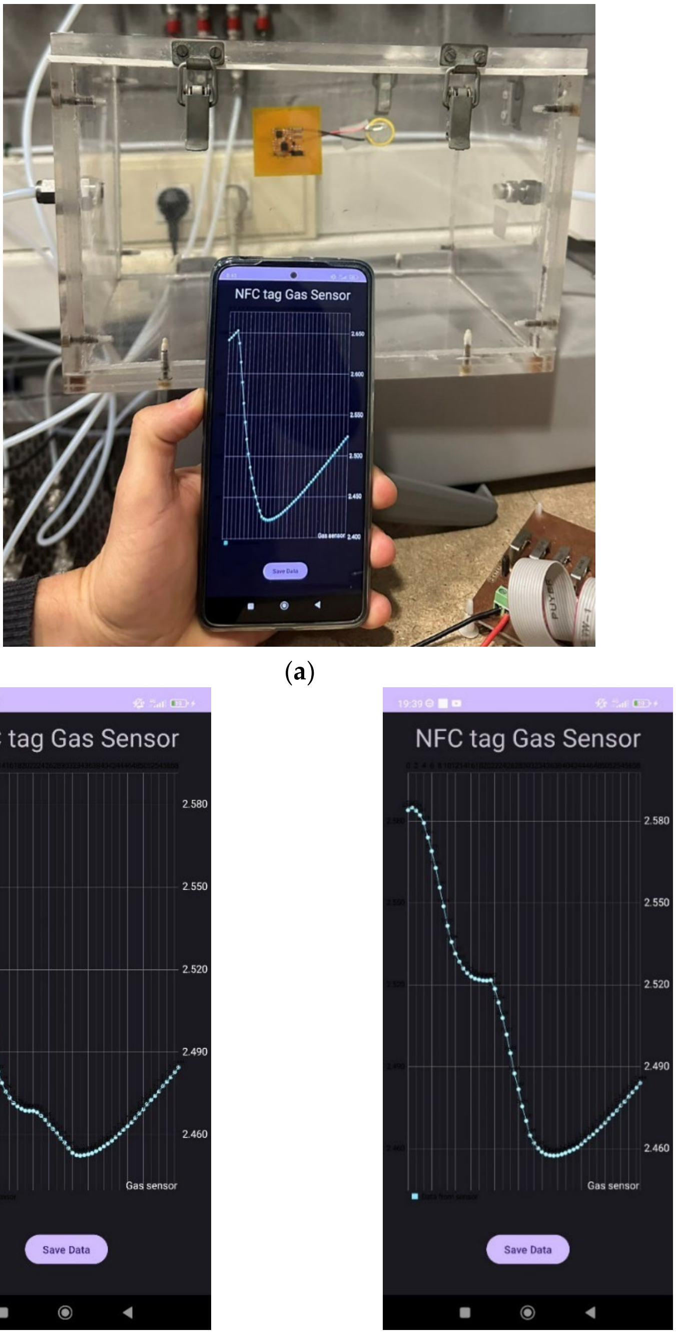

(**a**)

(**b**) (**c**)

Figure S7: (a) Picture of the testbench for the test of the wearable system developed in this work; Screenshots of the Android App (b) capturing the exposure of 1 ppm NO_2 (10 minutes), synthetic dry air (10 minutes), and 500 ppb (10 minutes); and (c) capturing the exposure of 500 ppb NO_2 (10 minutes), synthetic dry air (10 minutes), and 1 ppb (10 minutes).

References

1. Zhang, B.; Cheng, M.; Liu, G.; Gao, Y.; Zhao, L.; Li, S.; Wang, Y.; Liu, F.; Liang, X.; Zhang, T.; et al. Room Temperature NO2 Gas Sensor Based on Porous Co3O4 Slices/Reduced Graphene Oxide Hybrid. Sens Actuators B Chem 2018, 263, 387–399, doi:10.1016/j.snb.2018.02.117.

2. Li, W.; Chen, R.; Qi, W.; Cai, L.; Sun, Y.; Sun, M.; Li, C.; Yang, X.; Xiang, L.; Xie, D.; et al. Reduced Graphene Oxide/Mesoporous ZnO NSs Hybrid Fibers for Flexible, Stretchable, Twisted, and Wearable NO2 E-Textile Gas Sensor. ACS Sens 2019, 4, 2809–2818, doi:10.1021/acssensors.9b01509.

3. Kim, Y.H.; Kim, S.J.; Kim, Y.-J.; Shim, Y.-S.; Kim, S.Y.; Hong, B.H.; Jang, H.W. Self-Activated Transparent All-Graphene Gas Sensor with Endurance to Humidity and Mechanical Bending. ACS Nano 2015, 9, 10453–10460, doi:10.1021/acsnano.5b04680.

4. Luan, Y.; Zhang, S.; Nguyen, T.H.; Yang, W.; Noh, J.S. Polyurethane Sponges Decorated with Reduced Graphene Oxide and Silver Nanowires for Highly Stretchable Gas Sensors. Sens Actuators B Chem 2018, 265, 609–616, doi:10.1016/J.SNB.2018.03.114.

5. Huang, L.; Wang, Z.; Zhang, J.; Pu, J.; Lin, Y.; Xu, S.; Shen, L.; Chen, Q.; Shi, W. Fully Printed, Rapid-Response Sensors Based on Chemically Modified Graphene for Detecting NO2 at Room Temperature. ACS Appl Mater Interfaces 2014, 6, 7426–7433, doi:10.1021/am500843p.

6. Deng, S.; Tjoa, V.; Fan, H.M.; Tan, H.R.; Sayle, D.C.; Olivo, M.; Mhaisalkar, S.; Wei, J.; Sow, C.H. Reduced Graphene Oxide Conjugated Cu2O Nanowire Mesocrystals for High-Performance NO2 Gas Sensor. J Am Chem Soc 2012, 134, 4905–4917, doi:10.1021/ja211683m.

7. Chen, X.; Wang, T.; Han, Y.; Lv, W.; Li, B.; Su, C.; Zeng, M.; Yang, J.; Hu, N.; Su, Y.; et al. Wearable NO2 Sensing and Wireless Application Based on ZnS Nanoparticles/Nitrogen-Doped Reduced

Graphene Oxide. Sens Actuators B Chem 2021, 345, 130423, doi:10.1016/J.SNB.2021.130423.

8. Alouani, M.A.; Casanova-Cháfer, J.; Güell, F.; Peña-Martín, E.; Ruiz-Martínez-Alcocer, S.; de Bernardi-Martín, S.; García-Gómez, A.; Vilanova, X.; Llobet, E. ZnO-Loaded Graphene for NO2 Gas Sensing. Sensors 2023, 23, 6055, doi:10.3390/S23136055/S1.

9. Wang, Z.; Gao, S.; Fei, T.; Liu, S.; Zhang, T. Construction of ZnO/SnO2 Heterostructure on Reduced Graphene Oxide for Enhanced Nitrogen Dioxide Sensitive Performances at Room Temperature. ACS Sens 2019, 4, 2048–2057, doi:10.1021/acssensors.9b00648.

10. Liu, X.; Sun, J.; Zhang, X. Novel 3D Graphene Aerogel–ZnO Composites as Efficient Detection for NO2 at Room Temperature. Sens Actuators B Chem 2015, 211, 220–226, doi:10.1016/J.SNB.2015.01.083.

11. Ugale, A.D.; Umarji, G.G.; Jung, S.H.; Deshpande, N.G.; Lee, W.; Cho, H.K.; Yoo, J.B. ZnO Decorated Flexible and Strong Graphene Fibers for Sensing NO2 and H2S at Room Temperature. Sens Actuators B Chem 2020, 308, 127690, doi:10.1016/J.SNB.2020.127690.

12. Lin, C.S.; Hsieh, H.F.; Ding, C.F.; Li, K.M.; Young, H.T.; Hsiao, W.T. Laser Surface Modification on RGO/ZnO Composite Materials for NO2 Gas Sensing. Mater Chem Phys 2022, 290, 126551, doi:10.1016/J.MATCHEMPHYS.2022.126551.

13. Li, J.; Liu, X.; Sun, J. One Step Solvothermal Synthesis of Urchin-like ZnO Nanorods/Graphene Hollow Spheres and Their NO2 Gas Sensing Properties. Ceram Int 2016, 42, 2085–2090, doi:10.1016/J.CERAMINT.2015.09.134.

14. Zhang, L.; Tan, Q.; Kou, H.; Wu, D.; Zhang, W.; Xiong, J. Highly Sensitive NH3 Wireless Sensor Based on Ag-RGO Composite Operated at Room-Temperature. Scientific Reports 2019 9:1 2019, 9, 1–10, doi:10.1038/s41598-019-46213-9.

15. Zhu, R.; Azzarelli, J.M.; Swager, T.M. Wireless Hazard Badges to Detect Nerve-Agent Simulants. Angewandte Chemie International Edition 2016, 55, 9662–9666, doi:10.1002/ANIE.201604431.

16. Barandun, G.; Soprani, M.; Naficy, S.; Grell, M.; Kasimatis, M.; Chiu, K.L.; Ponzoni, A.; Güder, F. Cellulose Fibers Enable Near-Zero-Cost Electrical Sensing of Water-Soluble Gases. ACS Sens 2019, 4, 1662–1669, doi:10.1021/acssensors.9b00555.

17. Ma, Z.; Chen, P.; Cheng, W.; Yan, K.; Pan, L.; Shi, Y.; Yu, G. Highly Sensitive, Printable Nanostructured Conductive Polymer Wireless Sensor for Food Spoilage Detection. Nano Lett 2018, 18, 4570–4575, doi:10.1021/acs.nanolett.8b01825.

18. Zhu, R.; Desroches, M.; Yoon, B.; Swager, T.M. Wireless Oxygen Sensors Enabled by Fe(II)-Polymer Wrapped Carbon Nanotubes. ACS Sens 2017, 2, 1044–1050, doi:10.1021/acssensors.7b00327.

19. Escobedo, P.; Fernández-Ramos, M.D.; López-Ruiz, N.; Moyano-Rodríguez, O.; Martínez-Olmos, A.; Pérez de Vargas-Sansalvador, I.M.; Carvajal, M.A.; Capitán-Vallvey, L.F.; Palma, A.J. Smart Facemask for Wireless CO2 Monitoring. Nature Communications 2022 13:1 2022, 13, 1–12, doi:10.1038/s41467-021-27733-3.

20. Choi, J.; Visagie, I.; Chen, Y.; Abbel, R.; Parker, K. NFC-Enabled Dual-Channel Flexible Printed Sensor Tag. Sensors 2023, Vol. 23, Page 6765 2023, 23, 6765, doi:10.3390/S23156765.

21. Escobedo, P.; Erenas, M.M.; López-Ruiz, N.; Carvajal, M.A.; Gonzalez-Chocano, S.; de Orbe-Payá, I.; Capitán-Valley, L.F.; Palma, A.J.; Martínez-Olmos, A. Flexible Passive near Field Communication Tag for Multigas Sensing. Anal Chem 2017, 89, 1697–1703, doi:10.1021/acs.analchem.6b03901.

Publications not included in this thesis

The effect of doping rGO with MnO_2 nanomaterial on its gas sensing properties.

M.A. Alouani[1-2-3], J. Casanova-Chafer[4], S. de Bernardi-Martín[5]; A. García-Gómez[5] F. Salehnia[1-2-3], J.C. Santos-Ceballos[1-2-3], A. Santos-Betancourt[1-2-3], X. Vilanova[1-2-3] * and E. Llobet[1-2-3*]

[1]Universitat Rovira i Virgili, MINOS, School of Engineering, Avda. Països Catalans 26, 43007 Tarragona, Spain

[2]IU-RESCAT, Research Institute in Sustainability, Climatic Change and Energy Transition,

Universitat Rovira i Virgili, Joanot Martorell 15, 43480 Vila-seca, Spain

[3]TecnATox - Centre for Environmental, Food and Toxicological Technology, Universitat Rovira i Virgili, Avda. Països Catalans 26, 43007 Tarragona, Spain

[4]Université de Mons, Place du Parc 23, 7000 Mons, Belgium

[5]Gnanomat. C/Faraday 7, 28049 Madrid, Spain

* Correspondence: xavier.vilanova@urv.cat; eduard.llobet@urv.cat

Abstract: Manganese dioxide (MnO_2) has drawn attention as a sensitizer to be incorporated in graphene-based chemoresistive sensors thanks to its promising properties. In this regard, a rGO@MnO_2 sensing material was prepared and deposited on two different substrates (Silicon and Kapton). These sensors were exposed to different dilutions of NO_2 under dry and humid conditions at room temperature. Other gases or vapours such as NH_3, CO, ethanol and H_2 were also tested. FESEM, HRTEM, RAMAN and XRD were used to characterize the prepared sensors. The experimental results showed that the incorporation of MnO_2 in the rGO material enhanced its response towards NO_2. Moreover, this material showed also very good responses toward NH_3 both under dry and humid conditions and showed no cross-responsiveness towards other toxic gases.

Keywords: reduced graphene oxide; manganese dioxide (MnO_2); gas sensor; NO_2 detection; NH_3 detection.

1. Introduction

Technological and economic advances increasingly threaten the environment and air quality, necessitating urgent solutions. The demand for low-cost and effective gas sensors, crucial for detecting toxic agents such as nitrogen dioxide NO_2 [1], ammonia NH_3 [2], and carbon monoxide CO [3] in various fields, has never been more pressing. While traditional methods like infrared spectrophotometry (IRSP) [4], non-dispersive infrared analysis (NDIR) [5], and gas chromatography-mass spectrometry (GC-MS) [6] have been widely used for detecting toxic gases, they are not without significant drawbacks. Their high cost and complexity have underscored the need for a new, more efficient approach. This realization has led to the development of chemoresistive devices, known for their ease of operation, low production cost, fast response time, and ease of miniaturization [7].

Since their first use in the 1960s, metal oxides (MOX) such as ZnO [8], SnO_2 [9], WO_3 [10], and many more [11] have been studied as sensitive films to be used in the fabrication of chemoresistive devices for gas sensing and especially for detecting NO_2. Even though MOX are effective and sensitive, the need for a pervasive, widespread monitoring of air pollutants, has oriented research to the discovery of new, less power-hungry, gas sensitive materials. This has, for example, led to the emergence of graphene-based chemoresistive sensors. The unique and exceptional properties of graphene that made it a solid gas sensing material candidate are thermal stability, mechanical robustness, high conductivity, high carrier mobility at low to room temperatures, a large surface area of up to 2630 m^2/g for single-layer graphene, low electrical noise [12] and, most importantly, the fact that its electronic properties are easily affected by the adsorption of gas molecules [13].

One of the graphene derivatives is reduced graphene oxide (rGO). It was reported in the literature to be the best and most used graphene-based sensing material for detecting NO_2 [14] and NH_3 [15] due to its numerous defect sites and functional groups, which facilitate gas adsorption. rGO has been reported able to detect chemical warfare agents and explosives at trace levels (ppb) [16]. Moreover, the synthesis of rGO can be achieved via straightforward and inexpensive processes that reduce GO via chemical and thermal routes or even using UV light [17]. Studies have shown that pristine rGO gas sensors exhibit slow response and recovery dynamics. Hence, the hybridization of rGO with MOx has been a solution often explored to enhance its sensing properties (e.g. ameliorating response dynamics and extending the number of gases that can be detected), D.Tripathi et al, explored this process and an enhancement of the sensitivity and selectivity of the rGO material towards ammonia by incorporating WO_3 nanomaterial in the sensing layer was achieved [18]. Another reported work of D. Milad et al, where they showed that the synthesis of a TiO_2/rGO composite exhibited an improved gas sensing properties towards methanol and ethanol [19]. This is achieved via the MOX nanoparticles supported on rGO behaving as catalysts or as electronic sensitizers, favouring the occurrence of heterojunctions at the MOX/rGO interface.

Some of the reported MOx nanoparticles used for the loading of the rGO layers for gas sensing are ZnO [20], SnO_2 [21], and WO_3 [22]. Still, in recent years, MnO_2 has gained popularity due to its low toxicity, low cost, high stability, and ease of fabrication. It was also used in a wide range of applications and fields such as energy storage [23], biomedical field [24], and in developing gas sensors [25]. However, in the gas sensing field, there is a limited amount of reported work discussing the incorporation of the MnO_2 nanomaterial into rGO to achieve a sensitive layer towards different toxic gases. One of the few works reported is of Hui Zhang et al., where they successfully synthesized an rGO-coated Ni foam-supported MnO_2 for the enhanced detection of NO_2 at a concentration of 50 ppm while the sensor was operated at room temperature [26]. Meanwhile, Alexander et al. modified rGO with doping of MnO_2 nanoparticles and tested the rGO/MnO_2 composite as gas sensor for different gases such as 25 ppm of NO_2, 500 ppm of H_2 and 1000 ppm of CH_4 under dry conditions with heating at 85 °C [27]. Another reported work was of Ghosal et al. where they prepared different hybrids for alcohol vapor detection, being one of the hybrids rGO/MnO_2 nanoflowers binary composite and it showed good responses towards ethanol and methanol vapours in the range of 5-100 ppm while heating at 150 °C [28]. Lastly, Ahmad et al. made a ternary nanocomposite of PANI@rGO@MnO_2 using a multi-step process for NH_3 detection. The tests were made at 100 °C under dry conditions [29]. The fact that very few works have been reported on rGO@MnO_2 gas sensors so far, makes exploring further its gas sensing properties interesting and worthwhile.

In this paper, rGO@MnO_2 sensitive layers were successfully synthesized and deposited on different transducing substrates (Kapton and silicon with gold electrodes). The gas sensing performance of the rGO@MnO_2 sensors was studied for different reducing and oxidizing species. The effect of ambient moisture on sensor response was evaluated as well. Results are presented and thoroughly discussed. A sensing mechanism for the detection of ammonia and nitrogen dioxide is presented.

2. Materials and Methods

In this section a detailed explanation of the preparation of the doped reduced graphene oxide with MnO_2 nanomaterial with 95/5 wt.% alongside the process of depositing it on the Kapton and silicon substrates via the spray coating technique is presented. The section also describes the techniques employed in the study of the morphology and composition of the hybrid material and in the test of its gas sensing properties.

2.1. Preparation of reduced graphene oxide doped with MnO_2

rGO doped with MnO_2 nanomaterial (rGO/MnO_2 95/5 wt.%) was synthesized using a process based on patented procedures (Patent number ES2678419A1). Briefly, reduced graphene oxide was dispersed in oxalic acid, in which the starting Mn_3O_4 had been previously dissolved at 50 °C. After homogenization, MnO_2 nanomaterials were slowly precipitated on reduced graphene oxide by adding a basic solution (NaOH 5 M) under vigorous agitation. The solid was filtered and dried at 90 °C overnight. Synthesis parameters such as temperature, stirring speed, addition rate, or MnO_2/rGO proportion, were controlled to obtain the desired crystallinity that provides the material the optimal properties. Manganese oxide phase was checked via XRD, Figure S1 (in Supplementary Materials) shows the XRD diffractogram.

2.2 Substrates preparation and material deposition:

10 mg of the rGO@MnO_2 nanomaterial were weighted and suspended in a 10 ml ethanol solution via a 30-min sonication. Subsequently, suspended nanomaterials were deposited by spray coating onto two different substrates (i.e., silicon, and Kapton). During the coating process, substrates were heated at 50 °C to promote the evaporation of the solvent and the formation of a homogeneous film. The interdigitated gold electrodes were deposited on the substrates using different processes. For Kapton substrates, 9 nm of gold were sputtered using a shadow mask to form the electrodes. In contrast, for the silicon substrates, a two-step approach took place. At first, a laser lithography technique **(DWL 66fs, Heildelberg Instruments)** was used to pattern a photoresist that coated an oxidized silicon wafer in the shape of the electrodes. In the second step, a titanium adhesion layer was sputtered with a thickness of 10 nm, and then a gold layer was sputtered on top with a thickness of 100 nm. A final lift off process was conducted to obtain the electrodes. The silicon wafer was then diced. Figure 1 shows two sensors on the two types of substrates used.

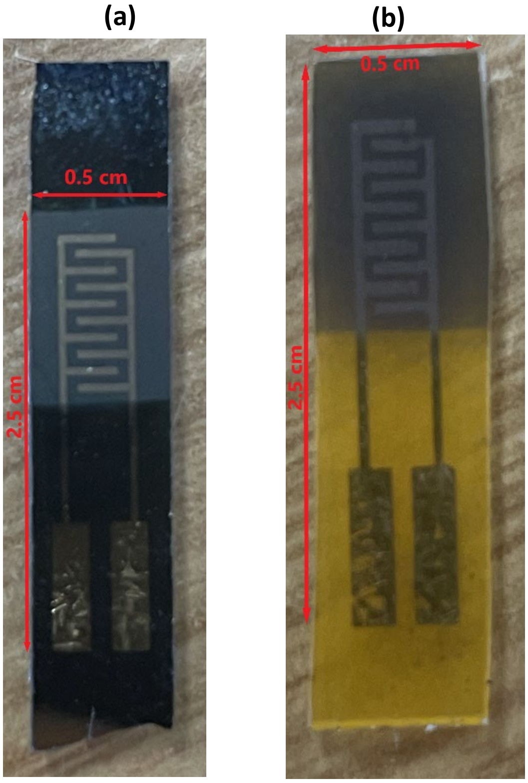

Figure 1. Pictures of the prepared sensors on the (a) Silicon substrate, (b) kapton substrate

2.3 Material characterization and gas sensing measurements

The obtained sensors were characterized using different techniques, such as Raman via a Raman spectrometer (Renishaw, plc., Wotton-under-Edge, UK), with a laser wavelength of 514 nm to check the crystallinity of the materials. A Field Emission Scanning Electron Microscope (FESEM) using a Carl Zeiss AG-Ultra 55 (ZEISS, Jena, Germany) to study the surface morphology and to check the distribution of the nanomaterial on the graphene layer. A JOEL F200 TEM ColdFEG operated at 200 kV was used for the high-resolution transmission electron microscopy (HRTEM) characterization. TEM images and electron diffraction patterns were acquired with a Gatan OneView camera, a CMOS-based and optical fibre-coupled detector of

4096 by 4096 pixels. Gatan Digital Micrograph program was used to process the (S)TEM images. STEM images (1024 x 1024 pixels) were recorded from the JEOL bright-field (BF) and high-angle annular dark-field (HAADF) detectors with a camera length of 200 mm. Samples were inserted in a JEOL beryllium double-tilt holder for energy-dispersive X-ray spectroscopy (EDS). STEM-EDS mapping was recorded from an EDS Centurio detector (silicon drift) with an effective area of 100 mm^2 and 133 eV of energy resolution. STEM-EDS maps (512 x 512 pixels) were processed with the JEOL Analysis software to check the shape of the MnO_2 nanomaterial and its incorporation in the graphene layers. Gas sensing measurements were conducted by placing the different sensors in an airtight Teflon chamber with a volume of 35 cm^3. A continuous stream of dry air (Air Premier, 99.995% purity) and diluted gases were passed through the testing chamber with a 100 mL/min flow via a set of Bronkhorst mass-flow controllers. The target gases from calibrated bottles (NO_2-1 ppm, CO-100 ppm, NH_3-100 ppm, and ethanol-20 ppm balanced in dry air) were further diluted using the mass flow controllers set. The resistance changes were continuously acquired using an Agilent HP 34972A multimeter. The humidity effect on the sensing performance was assessed by humidifying the gas stream through a controller evaporator mixer (CEM) to obtain low humidity levels of maximum 50% RH at 25ºC. For higher values of relative humidity, the flow of the dry air with the corresponding concentration of gas was humidified passing through a bubbling water system at room temperature. The sensing responses were calculated using the formula $R\ (\%) = ((R_g - R_a)/R_a) \times 100$, where R_g and R_a correspond to the resistance level after and before gas exposure, respectively.

3. Results

This section, presents and discusses at first the results of the characterization tests made for the prepared sensitive layers (rGO and rGO@MnO_2), which are based on the RAMAN, FESEM and HRTEM techniques. Secondly, the gas testing results for these sensors towards NO_2 and NH_3 at room temperature under dry conditions are presented, which is followed by the results gathered at different humidity levels.

Additionally, selectivity tests are reported. The results of the gas sensing tests are compared to those found in the literature. Finally, a sensing mechanism for the detection of NO_2 and NH_3 is introduced.

3.1 Sensitive layer characterization

3.1.1. Raman

The study of the molecular structure of carbon products and the assessment of disorders and defects in the material can be done using Raman spectroscopy analysis. Two specific peaks always appear when analysing graphene: the G-band and the D-band. The first one, placed at around 1500 $cm^{-1,}$ corresponds to the first-order scattering of the E_2g phonons at the Brillouin zone centre and originates from the in-plane vibrations of the sp^2 carbon atoms [30]. Meanwhile, the D-band is observed around 1300 cm^{-1} and represents the formation of j-point photons of A_1g symmetry; it is also associated with double bonds C=C, meaning the more intense the band is, the higher the presence of sp^2 domains is. Furthermore, D-band peak intensity depends highly on the presence of disorders and defects like vacancies and edges in the carbon lattice and grain boundaries [31]. To determine the degree of oxidation of the graphene, a simple calculation of the intensity ratio of both the D and G band peaks is enough, i.e., ID/IG; the higher this ratio is, the lower the oxidation level is [32].

Finally, the second-order bands are observed from 2500 cm^{-1} to 3200 cm^{-1}, containing one always visible peak at around 2700 cm^{-1}, known as the 2D band. They are used generally to determine the layers of the graphene since graphene is susceptible to stacking [33]. The chosen name of this band comes from the fact that it is the overtone of the D band, and two of the same phonons responsible for the D band are involved in the 2D band. Two other bands are sometimes reported when studying graphene Raman spectra, which are the D+G band, that can be seen around 2900 $cm^{-1,}$ and the combined overtone of the D and G bands, the 2G band around 3200 cm^{-1}, which is attributed to the overtone of the G band [34]. In our case, we are working with rGO, which means that the stacking of the layers is random, and since the width of the peaks is relative to the disorder, that can lead to an overlapping of the 2D band peak with the D+G and 2G, resulting in a bump like peak observed in the range of 2600 cm^{-1} to 3100 cm^{-1} [35].

Figures 2a and 2b show the Raman spectra of bare rGO and rGO doped with MnO_2 nanomaterial, respectively. For both cases, D bands are located at 1355 cm^{-1} and G bands around 1590 cm^{-1}. For the second-order bands, three visible peaks corresponding to the 2D, D+G, and 2G bands at respectively 2697 cm^{-1}, 2940 cm^{-1}, and 3188 cm^{-1} are present in the Raman spectra of the reduced graphene oxide; meanwhile, in the Raman spectra of the MnO_2 doped reduced graphene oxide we observe a bump-like peak around 2926 cm^{-1}, which is in agreement with the explanation made previously. Moreover, the ID/IG intensity ratio is 0.89 for rGO@MnO_2 and 0.85 for rGO, showing a slightly lower oxidation level in the doped rGO and the presence of higher number of defects, that can be caused by the doping process. Finally, it was noticed that the Raman signal in the rGO@MnO_2 sample shows a higher intensity than the pristine rGO sample, which can be correlated to the presence of the MnO_2 nanomaterial, since the presence of MOX usually leads to this increase in the intensity [36].

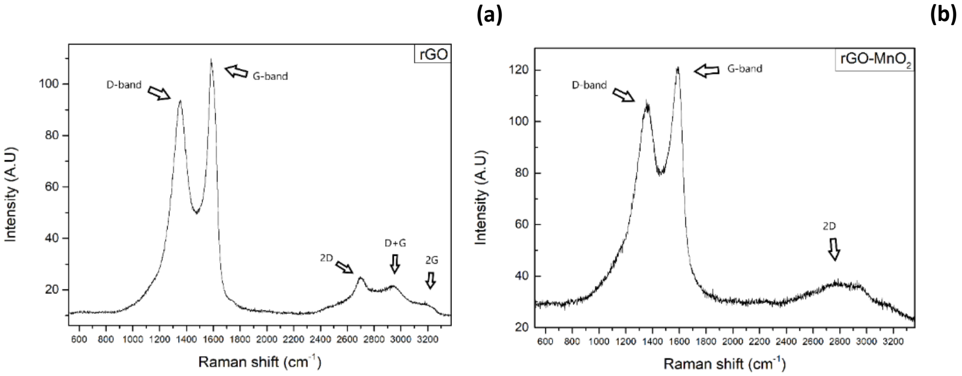

Figure 2. (a) Raman spectra of rGO and (b) Raman spectra of rGO@MnO_2.

3.1.2 FESEM

Figure 3.a. shows the obtained FESEM images of the layers present on the surface of the graphene loaded with MnO_2 on the silicon substrate

using a back-scattered electron detector (BSE). A very homogenous layers is observed covering the totality of the surface inspected. MnO_2 cannot be clearly seen, even when using a BSE detector, because of the low concentration of the nanomaterial and the small size but, when performing an EDS analysis of the surface, its presence was detected (see Figure s2 in the supplementary materials). Figure 3.b shows the FESEM image of the graphene doped with MnO_2 deposited on Kapton. Again, a very good coverage of the substrate surface is seen. However, in this case the surface of the substrate is getting rapidly charged because of the effect of the magnetic field coming from the BSE detector, leading to the formation of very bright areas. Similarly to the samples on silicon, an EDS analysis (see Figure s3 in the supplementary materials), the presence of MnO_2 was detected on the samples deposited over Kapton. Still, the MnO_2 crystals are too small to be seen in the FESEM images, just as for the sensing layer deposited on silicon.

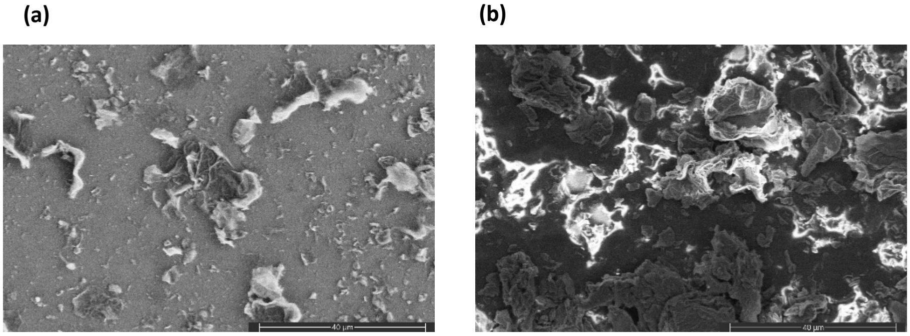

Figure 3. FESEM images of (a) the surface of the graphene doped with MnO_2 deposited on the Silicon substrate and (b) the surface of the graphene doped with MnO_2 deposited on the Kapton substrate.

3.1.3 HRTEM

An HR-TEM analysis was conducted to examine better the morphology of the MnO_2 nanomaterial and its incorporation in the graphene layer. Figure 4 shows an HR-TEM image of layers of graphene in addition to an interesting structure on the top right side; zooming in on this structure (Figure 4.b), a sponge-like shaped nanomaterial was observed, which was attributed to the MnO_2 after performing an EDS analysis.

Moreover, when chemically mapping the chosen area's surface, a high concentration of Mn is located in the same position as the sponge-like structure, proving the presence and the likely shape of the MnO_2 nanomaterial. Figure 4.d shows an EDS map spectrum of the same area, showing the elements present in the mapping appearing Mn with the highest concentration; the other elements, except for C and O, come from the grid of the HRTEM.

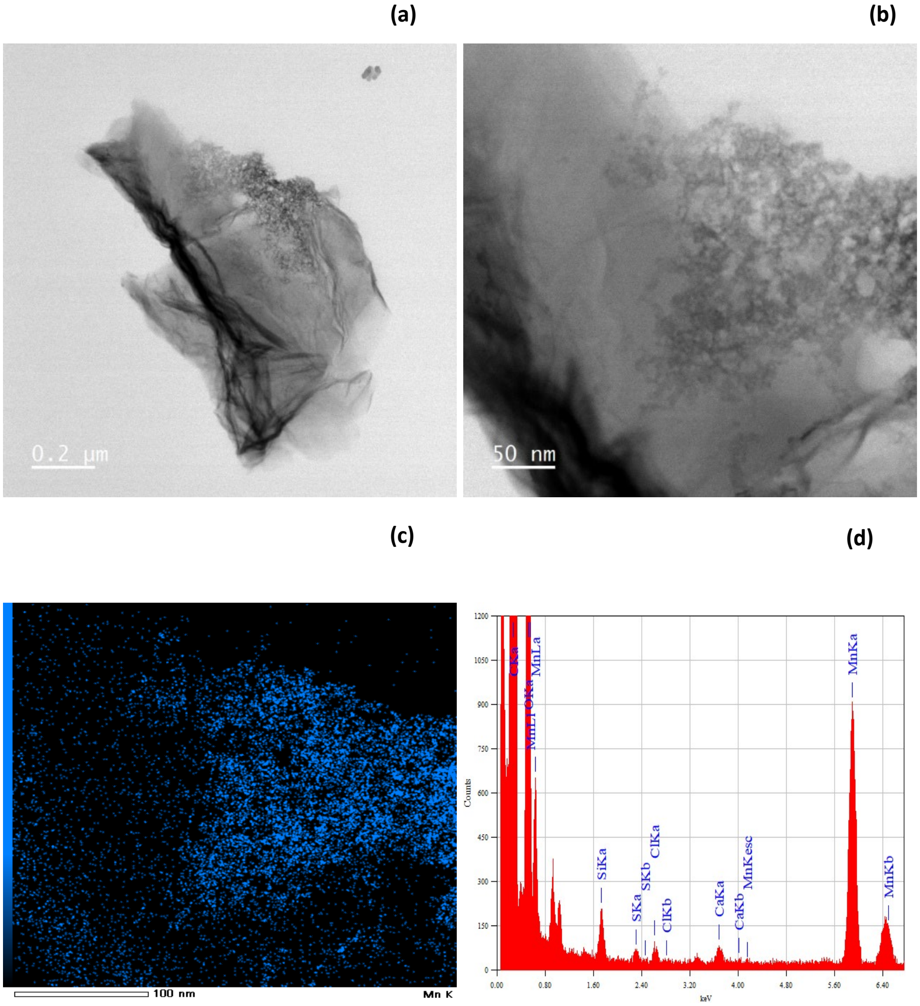

Figure 4. (a) HRTEM image of layered graphene doped with MnO_2 nanomaterial (b) a zoomed HRTEM image of a scale of 50 nm of the same material (c) EDS mapping showing Mn concentration on the area of analysis (d) EDS map spectrum of the studied area.

3.2 Gas sensing results

A selection of different toxic gases and vapours was used to study the sensing properties of the pristine rGO and rGO@MnO_2 sensors. First, NO_2 was thoroughly studied with different dilutions ranging from 200 ppb up to 1000 ppb under dry air as well as under ambient moisture conditions (close to real conditions). Sensors were always operated at room temperature. Then, NH_3 was also tested as an interferent gas with a concentration of 50 ppm under the same conditions used for NO_2. Figure 5.a shows the response of the different sensors towards different concentrations of NO_2. It was noticed that the type of substrate used does not affect the response of the sensitive layer towards the analyte. rGO on silicon and Kapton have almost the same response through the studied range, with an average difference of 0.8%. The same behaviour was also seen for the rGO@MnO_2 sensors, where the average difference between the responses was 0.4%. Moreover, the most important aspect to notice is that the sensors based on rGO incorporating MnO_2 show a superior response than the pristine ones (2-fold increase in response). The loading of rGO with MnO_2 is effective at increasing sensitivity towards NO_2. In fact, rGO@MnO_2 on Kapton exhibits a higher sensitivity of 3 % ppm^{-1} compared to the 1 % ppm^{-1} for the pristine rGO, meanwhile for the materials deposited on silicon the sensitivity of the doped material is slightly better than its pristine counterpart with 1.8 % ppm^{-1} for rGO@MnO_2 on silicon and 1.5 % ppm^{-1} for on rGO silicon. The sensitivity values were evaluated from the slope of the line obtained from the linear regression of the responses of the sensor towards different concentrations of the gas. Figure 5.b shows the resistance changes of the rGO@MnO_2 on silicon substrate for 600 ppb of NO_2 and figure 5.c shows the resistance changes of the rGO@MnO_2 on Kapton substrate for 600 ppb of NO_2 at 25% RH.

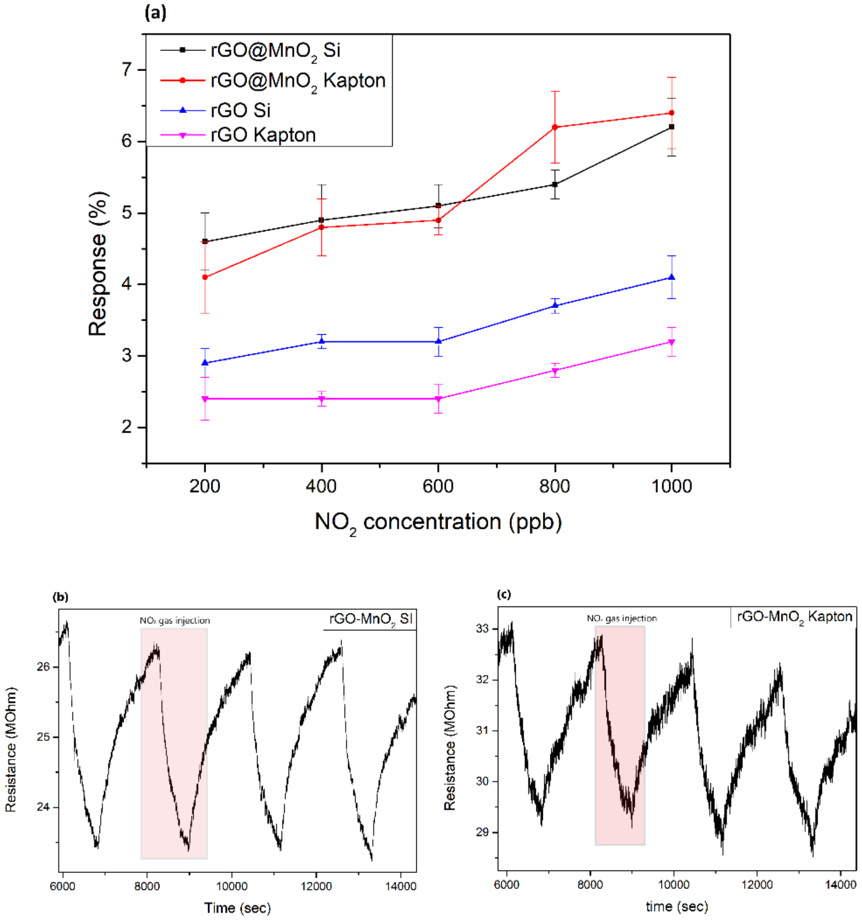

Figure 5. Calibration curve of the responses of the fabricated sensors towards different concentrations of NO_2 at room temperature and under dry conditions (b) resistance changes of the rGO@MnO_2 on silicon substrate for 600 ppb of NO_2 at 25% RH (c) resistance changes of the rGO@MnO_2 on Kapton substrate for 600 ppb of NO_2 at 25% RH.

Further studies were conducted where ambient moisture was introduced via two different methods to check its effect on the sensing properties of the sensors. The first method consisted of using a controller evaporator mixer (CEM) to obtain 25% RH and the second methods consisted of using a bubbling water glass bottle that was installed between the mass flow and the chamber to humidify the air and the gas to reach a maximum RH of 70%. Ambient temperature was kept constant at 25ºC throughout the measurement period. Figures 6.a and 6.b show the calibration curves for the studied sensors at 25 and 70 % of relative humidity, respectively. Comparing the results shown in Figure 6.a (dry conditions) and 6a (25 % RH), one can notice that the response of the MnO$_2$-doped rGO sensors under humid conditions increases by a factor of 2.5 than when under dry conditions. For example, the rGO@MnO$_2$ on Kapton sensor response for NO$_2$ 1000 ppb at 25% humidity is 17.6%, while it is 6.4% under dry conditions. Interestingly, the responses of the pristine rGO sensors at 25% RH were enhanced by factors of 3.5 and 4, reaching similar response intensities than those recorded for MnO$_2$-doped rGO sensors. For example, rGO on silicon and rGO on Kapton responses to NO$_2$ 1000 ppb were 13.8 % and 12.7 % respectively, whereas under dry atmosphere their responses were 4.1 % and 3.2 %, respectively. Sensitivity values were calculated following the slope of the linear regression of the responses values towards different dilutions of NO$_2$ and compiled in Table 1.

Table 1. Sensitivity values of the different sensors under 25% and 70% relative humidity at room temperature

Sensitivity (% ppm^{-1}) RH (%)	rGO-MnO$_2$ Silicon	rGO-MnO$_2$ Kapton	rGO Silicon	rGO Kapton
25	9.8	12.4	10.9	10.2
70	27.2	16.6	13.5	14.5

Meanwhile, figure 6.b reveals the calibration curves of the sensors under 70% ambient moisture. It is noticed that when increasing the concentration of water vapor, the response of the pristine rGO sensors is much more enhanced than the corresponding doped ones but the increase in the sensitivity is not so significant. When measuring 1000 ppb of NO$_2$, increasing the RH levels from 25 to 70 %, the response the pristine rGO sensors are doubled, while the sensitivity just increased in a factor of around 1.3. In the case of the rGO@MnO$_2$ sensors the increase in the response is only in the order of a factor of 1.2, but the increase in the sensitivity is higher than in the previous case especially for the sensor on silicon substrate, as can be seen in table 1.

This behaviour of the pristine rGO layers is expected, since the same material was already reported in the literature as a humidity detector, such as in the work of Muhammed et al. where they fabricated a rGO and rGO/Fe_2O_3 components for humidity detection and the pristine material showed a high sensitivity towards RH and it increased more with the incorporation of Fe_2O_3[37]. Zhou et al. managed also to make humidity sensors with the sensitive layer of rGO/SnO_2, initially they tested the pristine SnO_2 sensitivity and response towards 75% RH and they saw these results improve by adding rGO and making rGO/SnO_2 porous film indicating the fact that rGO is a very sensitive material towards humidity [38]. Although in this work pristine rGO response towards RH increases with the increase of the humidity level, the doping of rGO with MnO_2 made the response less affected by the RH levels but the sensitivity is increased when the level of humidity increases.

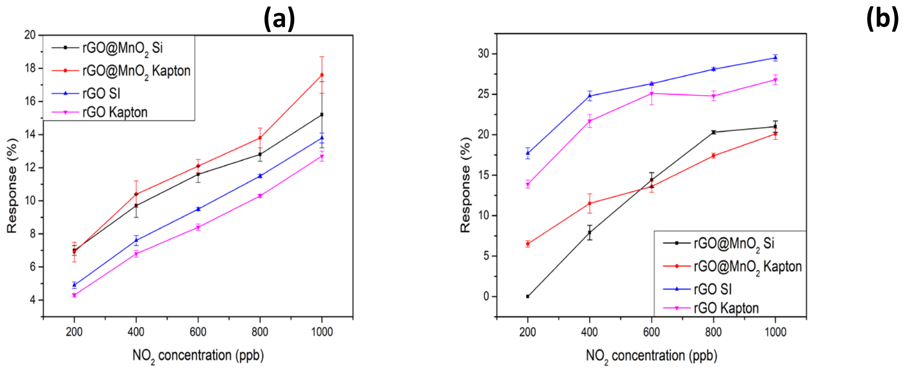

Figure 6. (a) calibration curves of the different sensors under 25% relative humidity at room temperature and (b) calibration curves under 70% relative humidity at room temperature.

Table 2 compares the results reported here with those of the literature. The sensors we report are more sensitive to NO_2 than those found in the literature. In addition, the concentrations tested in the literature are generally higher than the ones reported here, which indicates that our material is more sensitive in the low ppm concentration range. While most works totally overlook the effect of ambient humidity in the sensing properties, our material is shown to be able to detect NO_2 in a wide range of ambient moisture levels.

Table 2. Comparison of the sensing performance to NO_2 of different materials and rGO-based compounds.

Material	NO_2 concentration (ppm)	Response (%)	Condition	Sensitivity (%ppm^{-1})	T (°C)	ref
Nano-MnO_2/xanthan	7	1.21	Dry	0.17	RT	[39]
δ-MnO_2-Epitaxial Graphene-Silicon Carbide Heterostructures	5	0.27	55% RH	0.14	RT	[40]
Porous MnO_2 /rGO	50	5.9	Dry	0.118	RT	[26]
ZnO/rGO	10	5.1	Dry	0.51	RT	[41]
rGO pomegranate peels	1	3.04	Dry	2.94	100	[42]
Phosphate doped rGO	1	4.5	Dry	4.5	RT	[43]
VO_2/rGO	5	1.63	Dry	0.326	RT	[44]
MnO_2 doped rGO	1	6.2	Dry	9.8	RT	This work
MnO_2 doped rGO	1	21	70% RH	27.2	RT	This work

The selectivity of the different sensors we tested was studied under the same experimental conditions used for NO_2 detection. Different species, namely, CO (50 ppm), NH_3 (50 ppm), H_2 (500 ppm) and Ethanol (20 ppm) under dry conditions for sensors operating at room temperature were measured. Figure 7 shows the responses to these different gases or vapours. As can be seen, none of the sensors showed any response to H_2. Noticeably, the inclusion of the MnO_2 reduced the response towards

CO and Ethanol, making it utterly unresponsive to these interfering gases. Therefore, the incorporation of MnO_2 improved the sensors selectivity. Nevertheless, all the sensors showed very significant responses towards 50 ppm of NH_3.

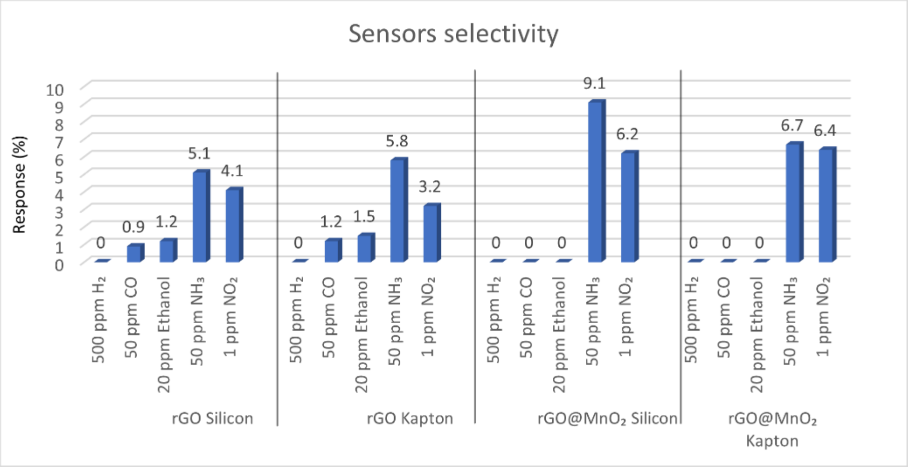

Figure 7. Comparison of the responses of the different sensors towards different gases at dry conditions to study the selectivity of the sensitive layer.

Taking into account the good responses observed for NH_3, the effect of moisture in the sensor responses to this gas was analysed. The sensors were exposed to 50 ppm of NH_3 under different humidity conditions (dry, 25 % RH and 50 % RH), always at room temperature. Figure 8.a shows the responses of the sensors to 50 ppm of ammonia for the three different humidity conditions studied and figure 8.b shows resistance changes of the sensor pristine rGO on Kapton when exposed to NH_3. As seen in the figure, when exposed to ammonia analyte, the sensors resistance decreases in contrast to what is expected for a p-type material, this behaviour was explained later in the mechanism part. It is noticed also that the response of the rGO@MnO_2 on silicon sensor is the highest throughout all the conditions. The response of this sensor reaches a value of 18.5 % at 50 % RH, which is 4 times higher than the response of the pristine rGO on silicon. rGO@MnO_2 and pristine rGO on Kapton show basically the same behaviour and the doped one shows a slightly higher response towards NH_3, with values of 6.7 % and 5.8 % for rGO@MnO_2 and rGO respectively under dry conditions, 7.5 % and 6 % for 25 % RH and 8 % and 6.7 % at 50 % RH. Pristine rGO on silicon shows the lowest response values towards ammonia with a value of 4.6 % at 50 % RH. In essence, pristine rGO on Kapton and on Silicon substrates shows a linear-like behaviour throughout the different RH levels tested with a very little increase in sensitivity with increasing moisture levels. To have a better understanding of the behaviour of the sensors towards ammonia under humidity, it could be explained as following: Since we are working in a humid environment, the sensing layers have already adsorbed water molecules on its surface, saturating to an extent the adsorption sites especially of the pristine rGO layers. Later on, when these layers are exposed to a NH_3 gas flow, another phenomenon happens in the working atmosphere, and it can be attributed to the characteristics of ammonia itself. In fact, both H_2O and NH_3 have a strong tendency to form H bonds. Moreover, the electronegativity of the atoms determines the possibility of forming hydrogen bonds, and since oxygen is more electronegative than nitrogen, the O atom from H_2O rapidly creates a hydrogen bond with NH_3 [45] as shown in figure 8.c. Therefore, when considering the silicon substrate sensors, the response of the pristine rGO sensor remains unchanged practically because of the phenomenon previously explained preventing ammonia molecules from getting adsorbed on the surface. Meanwhile, for the rGO@MnO_2 sensor the significant increase in the response, despite the occurrence of the hydrogen bonding of the ammonia and water molecules, can be explained by the presence of the MnO_2 nanomaterial which plays a compensatory role by creating more adsorption sites in the layer, meaning more space for the ammonia and water molecules to be adsorbed also it has been previously reported as a good NH_3 adsorbing agent [46] which explains the increase of the response of the MnO_2@rGO sensor. As for the sensors deposited on Kapton, both pristine rGO and rGO@MnO_2 showing similar behaviour can be explained by the fact that the substrate is made of a very strong hydrophobic material. Therefore, water molecules are getting repelled off of the surface resulting in a poor

H_2O adsorption hence the low dependency of these sensors to the ambient moisture.

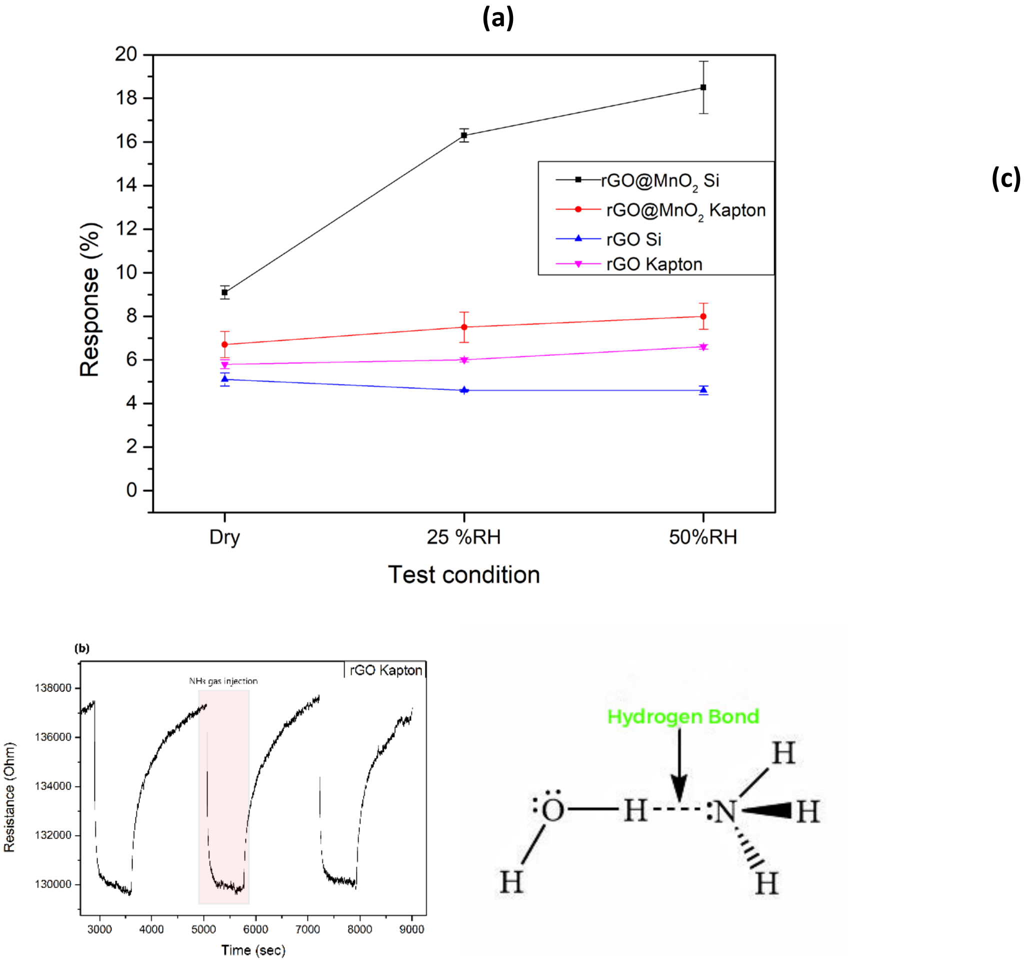

Figure 8. (a) Calibration curve of the responses of the fabricated sensors towards different test conditions (Dry, 25 % RH and 50 % RH) (b) resistance changes of the sensor pristine rGO on Kapton when exposed to NH_3 at 25% RH(c) Hydrogen bonding of water and ammonia molecules.

To check the position of this work in the literature regarding ammonia detection, a set of data such as response and sensitivity of other materials and sensors analysing NH_3 gas were collected and compiled in Table 3 and put in comparison with our results. Considering the same

NH_3 concentration, $NiFe_2O_4$/rGO had a response of 1.17 meanwhile Pani@MnO_2@rGO had a response of 15.5 while heating up to 100°C. Both these materials showed lower responses than our work which is 18.6 % at 50 % RH. It is true that $FeCo_2O_4/WO_3$/rGO have a slightly higher response of 19.8 % at dry conditions, but in this work NH_3 concentration is 100 ppm and the working temperature is 200°C, meanwhile we are working at RT and half of NH_3 concentration.

Table 3. Comparison of the sensing performance to NH_3 of different materials and rGO-based compounds.

Material	**NH_3 concentration (ppm)**	**Response (%)**	**Condition**	**T (°C)**	**ref**
PANI@MnO_2@rGO	50	15.5	Dry	100	[29]
$NiFe_2O_4$/rGO	50	1.17	Dry	0	[47]
rGO/WO_3	40	8.03	55 % RH	35	[48]
$FeCo_2O_4/WO_3$/rGO	100	19.8	Dry	200	[49]
$CoFe_2O_4$/rGO	25	1.06	Dry	RT	[50]
rGO@MnO_2	50	18.6	50% RH	RT	This work

3.3 Sensing mechanism

Graphene and its derivatives, such as rGO, are p-type materials, which implies that usually, the interaction between rGO and oxidizing gases such as NO_2 causes a change in the local carrier concentration and, therefore, a decrease in graphene-based sensor resistance meanwhile when exposed to reducing gas such as NH_3 an increase in the resistance takes place [51]. Meanwhile, MnO_2 is an n-type nanomaterial, and when exposed to an ambient environment, a chemisorption of the oxygen molecules takes place, capturing electrons from it and releasing different oxygen species such as O_2, O^{2-} and O^- [52]. Moreover, the incorporation of the MOx nanomaterial (in our case, MnO_2) in the rGO results in the formation of a p-n heterojunction, causing the flow of the electrons from the MnO_2 to rGO, implying the formation of a depletion layer on the area of contact of both materials, also increasing the electron concentration in the rGO and the hole concentration in MnO_2 [53]. The exposure of the rGO@MnO_2 to air leads to the adsorption of oxygen on the surface of the p-n heterojunction material and the transfer of electrons from its conduction band to the oxygen, resulting in the formation of O_2^- ions following these equations [54]:

$$O_2\,\text{gas} \rightarrow O_2\,(\text{ads})$$

$$O_2\,(\text{ads}) + e^- \rightarrow O_2^-\,(\text{ads})$$

When exposed to NO_2, it gets adsorbed on the rGO@MnO_2 surface and reacts with the oxygen ions and electrons from the layer following this equation, causing the decrease of the resistance of the sensor:

$$NO_2(\text{ads}) + O_2^-\,(\text{ads}) + 2e^- \rightarrow NO_2^- + 2O^-\,(\text{ads}).$$

As expected, our material showed the exact same behaviour explained previously, where the baseline resistance of the sensors decreased when put in contact with NO_2 gas and recovered again when the gas flow stopped.

Although NH_3 is a strong reducing gas, the baseline resistance should increase when in contact with the gas but not in our case where the resistance of our sensors decreased. This kind of behaviour have been reported previously in the literature by A. Umar et al. and it was explained as following:

when exposed to NH_3, the interaction between the analyte and the sensitive layer results in the release of electrons back to the conduction band of the MnO_2 nanomaterial, which is believed to be the cause of the decrease of the resistance of the sensor [29] This abnormal behaviour has been observed also for pristine rGO and was reported in the work of X.Xiao et al. [55]. Finally, it is worth noting that ambient moisture usually enhances the sensitivity of graphene-based sensors [56]. Considering the room temperature detection, the water molecules probably act as a mediated adsorption site for the analyte, causing an increase in sensitivity towards the target gas [57] which is in accordance with the results we obtained where the responses of the sensors increased under the ambient moisture conditions.

4. Conclusions

Incorporating MnO_2 nanomaterial in rGO flakes to form a MnO_2@rGO nanomaterial to be integrated in chemoresistive sensors is a novel approach, since a very limited number of papers exist in the literature reporting the use of this material as a sensitive layer for gas detection. Our nanomaterial exhibits better performance and properties than other approaches previously reported in the literature, showing a set of very promising results and high responses towards low concentrations of NO_2 and NH_3. When deposited either onto rigid (silicon) or flexible (polyimide) transducing substrates, the material shows good response properties when operated at room temperature and even in the presence or ambient humidity. Furthermore, sensors show very small cross-sensitivity to other species such as hydrogen, ethanol vapours or carbon monoxide. All these properties make MnO_2@rGO an excellent candidate nanomaterial for the inexpensive, chemoresistive detection of nitrogen dioxide or ammonia in real life environments.

References

[1] Chao Zhang, Yifan Luo, Jiaqiang Xu, Marc Debliquy, Room temperature conductive type metal oxide semiconductor gas sensors for NO2 detection, Sensors and Actuators A: Physical, Volume 289, 2019, Pages 118-133, ISSN 0924-4247, https://doi.org/10.1016/j.sna.2019.02.027.

[2] Qili Chen, Shan Wang, Shuaishuai Bai, Lihua Shen, Jiaming Peng, Yufeng Zhang, Xiaoni Cui, Chunxia Yu, Runlan Zhang, Yuangang Li, Zhifang Liu, Sub-ppt NH_3 detection by MoS2@sulfur nanosheets, Journal of Alloys and Compounds, Volume 985, 2024, 174070, ISSN 0925-8388, https://doi.org/10.1016/j.jallcom.2024.174070.

[3] Nisa Naseem, Farwa Tariq, Yumna Malik, Waqar Ali Zahid, Ahmed Abd El-Fattah, Khurshid Ayub, Javed Iqbal, Sensing ability of carbon nitride (C6N8) for the detection of carbon monoxide (CO) and carbon dioxide (CO2), Sensors and Actuators A: Physical, Volume 366, 2024, 114947, ISSN 0924-4247, https://doi.org/10.1016/j.sna.2023.114947.

[4] H. Namduri, S. Nasrazadani, Quantitative analysis of iron oxides using Fourier transform infrared spectrophotometry, Corrosion

Science, Volume 50, Issue 9, 2008, Pages 2493-2497, ISSN 0010-938X, https://doi.org/10.1016/j.corsci.2008.06.034.

[5] Jingyang Shi, Yadong Jiang, Zaihua Duan, Juan Li, Zhen Yuan, Huiling Tai, Designing an optical gas chamber with stepped structure for non-dispersive infrared methane gas sensor, Sensors and Actuators A: Physical, Volume 367, 2024, 115052, ISSN 0924-4247, https://doi.org/10.1016/j.sna.2024.115052.

[6] Elvis D. Okoffo, Kevin V. Thomas, Quantitative analysis of nanoplastics in environmental and potable waters by pyrolysis-gas chromatography–mass spectrometry, Journal of Hazardous Materials, Volume 464, 2024, 133013, ISSN 0304-3894, https://doi.org/10.1016/j.jhazmat.2023.133013.

[7] Gaiardo, A.; Novel, D.; Scattolo, E.; Crivellari, M.; Picciotto, A.; Ficorella, F.; Iacob, E.; Bucciarelli, A.; Petti, L.; Lugli, P.; et al. Optimization of a Low-Power Chemoresistive Gas Sensor: Predictive Thermal Modelling and Mechanical Failure Analysis. *Sensors* **2021**, *21*, 783. https://doi.org/10.3390/s21030783

[8] Kai Sun, Guanghui Zhan, Lin Zhang, Zilin Wang, Shiwei Lin, Highly sensitive NO2 gas sensor based on ZnO nanoarray modulated by oxygen vacancy with Ce doping, Sensors and Actuators B: Chemical, Volume 379, 2023, 133294, ISSN 0925-4005, https://doi.org/10.1016/j.snb.2023.133294.

[9] Yulin Kong, Yuxiu Li, Xiuxiu Cui, Linfeng Su, Dian Ma, Tingrun Lai, Lijia Yao, Xuechun Xiao, Yude Wang, SnO2 nanostructured materials used as gas sensors for the detection of hazardous and flammable gases: A review, Nano Materials Science, Volume 4, Issue 4, 2022, Pages 339-350, ISSN 2589-9651, https://doi.org/10.1016/j.nanoms.2021.05.006.

[10] Anna Staerz, Simona Somacescu, Mauro Epifani, Tetsuya Kida, Udo Weimar, and Nicolae Barsan, WO_3-Based Gas Sensors: Identifying Inherent Qualities and Understanding the Sensing Mechanism, *ACS Sensors* **2020** *5* (6), 1624-1633, DOI: 10.1021/acssensors.0c00113

[11] S.Roy Morrison, Semiconductor gas sensors, Sensors and Actuators, Volume 2, 1981, Pages 329-341, ISSN 0250-6874, https://doi.org/10.1016/0250-6874(81)80054-6.

[12] Schedin, F., Geim, A., Morozov, S. *et al.* Detection of individual gas molecules adsorbed on graphene. *Nature Mater* **6**, 652–655 (2007), https://doi.org/10.1038/nmat1967.

[13] Novoselov KS, Geim AK, Morozov SV, Jiang D, Zhang Y, Dubonos SV, Grigorieva IV, Firsov AA. Electric field effect in atomically thin carbon films. Science. 2004 Oct 22;306(5696):666-9. DOI: 10.1126/science.1102896.

[14] Li, D.; Lu, J.; Zhang, X.; Jin, D.; Jin, H. Engineering of ZnO/rGO towards NO_2 Gas Detection: Ratio Modulated Sensing Type and Heterojunction Determined Response. *Nanomaterials* **2023**, *13*, 917. https://doi.org/10.3390/nano13050917

[15] Anna Thomas, B.G. Jeyaprakash, Selective detection of ammonia by rGO decorated nanostructured ZnO for poultry and farm field applications, Synthetic Metals, Volume 290, 2022, 117140, ISSN 0379-6779, https://doi.org/10.1016/j.synthmet.2022.117140.

[16] Fan-Li Meng, Zheng Guo, Xing-Jiu Huang, Graphene-based hybrids for chemiresistive gas sensors, TrAC Trends in Analytical Chemistry, Volume 68, 2015, Pages 37-47, ISSN 0165-9936, https://doi.org/10.1016/j.trac.2015.02.008.

[17] Majhi, S.M.; Mirzaei, A.; Kim, H.W.; Kim, S.S. Reduced Graphene Oxide (rGO)-Loaded Metal-Oxide Nanofiber Gas Sensors: An Overview. *Sensors* **2021**, *21*, 1352. https://doi.org/10.3390/s21041352

[18] Divya Tripathi *et al* 2024 *Nanotechnology* **35** 065503. **DOI** 10.1088/1361-6528/ad090a

[19] Milad Daneshnazar, Babak Jaleh, Mahtab Eslamipanah, Rajender S. Varma, Optical and gas sensing properties of TiO2/RGO for methanol, ethanol and acetone vapors, Inorganic Chemistry Communications, Volume 145, 2022, 110014, ISSN 1387-7003, https://doi.org/10.1016/j.inoche.2022.110014.

[20] Z. U. Abideen, H. W. Kim and S. S. Kim, Chem. Commun., 2015, DOI: 10.1039/C5CC05370F.

[21] Jae-Hyoung Lee, Akash Katoch, Sun-Woo Choi, Jae-Hun Kim, Hyoun Woo Kim, and Sang Sub Kim, *ACS Applied Materials & Interfaces* **2015** *7* (5), 3101-3109, DOI: 10.1021/am5071656.

[22] Gajanan M. Hingangavkar, Sujit A. Kadam, Yuan-Ron Ma, Sushilkumar S. Bandgar, Ramesh N. Mulik, Vikas B. Patil, Tailored formation of WO3-rGO nanohybrids for dependable low temperature NO2 sensing, Ceramics International, Volume 49, Issue 23, Part B, 2023, Pages 38866-38876, ISSN 0272-8842, https://doi.org/10.1016/j.ceramint.2023.09.223.

[23] Zhang QZ, Zhang D, Miao ZC, Zhang XL, Chou SL. Research Progress in MnO-Carbon Based Supercapacitor Electrode Materials. Small. 2018 Jun;14(24) e1702883. DOI:10.1002/smll.201702883. PMID: 29707887.

[24] Muyu, Wu & Hou, Pingfu & Dong, Lina & Cai, Lulu & Chen, Zhudian & Zhao, Mingming & Li, Jingjing. (2019). Manganese dioxide nanosheets: from preparation to biomedical applications. International Journal of Nanomedicine. Volume 14. 4781-4800. DOI: 10.2147/IJN.S207666.

[25] Malook, K., Khan, H., Shah, M. and Haque, I.-U. (2019), Highly selective and sensitive response of Polypyrrole–MnO_2 based composites towards ammonia gas. Polym. Compos., 40: 1676-1683. https://doi.org/10.1002/pc.24917

[26] Zhang, Hui & Ou, Kangtai & Guan, Ruihua & Cao, Yang & Sun, Youyi & Li, Xiao. (2022). A Highly Sensitive Room-Temperature NO 2 Gas Sensor based on Porous MnO 2 /rGO Hybrid Composites. Current Nanoscience. 18. DOI: 10.2174/1573413718666220616154244.

[27] Zöpfl, Alexander & Lemberger, Michael-Maximilian & König, Matthias & Ruhl, Guenther & Matysik, Frank-Michael & Hirsch, Thomas. (2014). Reduced graphene oxide and graphene composite materials for improved gas sensing at low temperature. Faraday discussions. 173. 403-14. DOI:10.1039/c4fd00086b.

[28] S. Ghosal and P. Bhattacharyya, "Fabrication, Characterization, and Gas Sensing Performance of Pd, RGO, and MnO_2 Nanoflowers-Based Ternary Junction Device," in *IEEE Transactions on Electron Devices*, vol. 66, no. 9, pp. 3982-3987, Sept. 2019, doi: 10.1109/TED.2019.2925862

[29] Ahmad Umar, Sheikh Akbar, Rajesh Kumar, Faheem Ahmed, Sajid Ali Ansari, Ahmed A. Ibrahim, Mohsen A. Alhamami, Noura Almehbad, Hassan Algadi, Tubia Almas, Wen Zeng, Unveiling the potential of PANI@MnO_2@rGO ternary nanocomposite in energy storage and gas sensing, Chemosphere, Volume349, 2024, 140657, ISSN 0045-6535, https://doi.org/10.1016/j.chemosphere.2023.140657.

[30] Fenping Yin, Shang Wu, Yanbin Wang, Lan Wu, Peilin Yuan, Xia Wang, Self-assembly of mildly reduced graphene oxide monolayer for enhanced Raman scattering, Journal of Solid-State Chemistry, Volume 237, 2016, Pages 57-63, ISSN 0022-4596, https://doi.org/10.1016/j.jssc.2016.01.015.

[31] R. Britto Hurtado, M. Cortez-Valadez, J.R. Aragon-Guajardo, J.J. Cruz-Rivera, F. Martínez-Suárez, M. Flores-Acosta, One-step synthesis of reduced graphene oxide/gold nanoparticles under ambient conditions, Arabian Journal of Chemistry, Volume 13, Issue 1, 2020, Pages 1633-1640, ISSN 1878-5352, https://doi.org/10.1016/j.arabjc.2017.12.021.

[32] S. Yavuz and P. R. Bandaru, "Ag nanowire coated reduced graphene oxide/n-silicon Schottky junction based solar cell," 2016 IEEE Conference on Technologies for Sustainability (SusTech), Phoenix, AZ, USA, 2016, pp. 265-269, doi: 10.1109/SusTech.2016.7897178.

[33] Md Said, Nur Hidayah & Liu, Wei Wen & Lai, Chin wei & Zulkepli, Nik Noriman & Khe, Cheng-Seong & Hashim, U. & Lee, H Cheun. (2017). Comparison on graphite, graphene oxide and reduced graphene oxide: Synthesis and characterization. AIP Conference Proceedings. 1892. 150002. DOI:10.1063/1.5005764.

[34] Phys. Chem. Chem. Phys., 2019,21, 10125-10134

[35] Meenu Sharma, Sonam Rani, Devesh K. Pathak, Ravi Bhatia, Rajesh Kumar, I.Sameera, Temperature dependent Raman modes of reduced

graphene oxide: Effect of anharmonicity, crystallite size and defects, Carbon, Volume 184, 2021, Pages 437-444, ISSN 0008-6223, https://doi.org/10.1016/j.carbon.2021.08.014.

[36] Girish Murlidhar Rajguru, Rakesh Kumar Mishra, Prashant B. Kharat, Pankaj P. Khirade, Structural, microstructural and optical characteristics of rGO-ZnO nanocomposites via hydrothermal approach, Optical Materials, Volume 154, 2024, 115720, ISSN 0925-3467, https://doi.org/10.1016/j.optmat.2024.115720.

[37] Yaseen Muhammad, Mutabar Shah, Muhammad Asim Safi, Sana Gul Khattak, Aqib Aziz, Hoor Hassan, highly selective and sensitive humidity sensor using reduced graphene oxide based iron oxide nanocomposites, Materials Science and Engineering: B, Volume 303, 2024, 117324, ISSN 0921-5107, https://doi.org/10.1016/j.mseb.2024.117324.

[38] Z. Li, D.W.W. Gardner, Y. Xia, S. Zhao, A. Pan, N. Goel, S. Bart, C. Liu, J. Yi, C. Carraro, R. Maboudian, Ordered porous RGO/SnO2 thin films for ultrasensitive humidity detection, J. Mater. Chem. C Mater. 11 (2023) 9586–9592. http://dx.doi.org/10.1039/D3TC00983A

[39] Alaa Fahmy, Ahmed M. Saeed, Usama Dawood, Hassan Abdelbary, Korinna Altmann, Andreas Schönhals, Nano-MnO_2/xanthan gum composite films for NO_2 gas sensing, Materials Chemistry and Physics, Volume 296, 2023, 127277, ISSN 0254-0584, DOI:10.1016/j.matchemphys.2022.127277

[40] Pedowitz, M. D., Kim, S., Lewis, D. I., Uppalapati, B., Khan, D., Bayram, F., … Daniels, K. M. (2020). Fast Selective Sensing of Nitrogen-Based Gases Utilizing δ -MnO_2-Epitaxial Graphene-Silicon Carbide Heterostructures for Room Temperature Gas Sensing. Journal of Microelectromechanical Systems, 1–7. doi:10.1109/jmems.2020.3007342.

[41] Lu, J., Li, D., Chen, X. et al. ZnO/reduced graphene oxide nanocomposite with synergic enhanced gas sensing performance for the effective detection of NO_2 at room temperature. J Nanopart Res 24, 265 (2022). https://doi.org/10.1007/s11051-022-05642-w.

[42] Kacem, K., Ameur, S., Casanova-Chafer, J. *et al.* Bio-reduction of graphene oxide using pomegranate peels for NO_2 sensing and photocatalysis applications. *J Mater Sci: Mater Electron* **33**, 16099–16112 (2022). https://doi.org/10.1007/s10854-022-08501-5

[43] Bashir E. Hasanov, Juan Casanova-Chafer, Geetanjali Deokar, José D. Gouveia, Saidkhodzha Nematulloev, José R.B. Gomes, Eduard Llobet, Pedro M.F.J. Costa, Amplified sensing of nitrogen dioxide with a phosphate-doped reduced graphene oxide powder, Carbon, Volume 226, 2024, 119207, ISSN 0008-6223, https://doi.org/10.1016/j.carbon.2024.119207.

[44] Liang, J., Wu, W., Lou, Q. *et al.* Room temperature NO_2 sensing performance enhancement of VO_2(B) composited rGO structure. *J Mater Sci: Mater Electron* **33**, 15473–15482 (2022). https://doi.org/10.1007/s10854-022-08454-97

[45] Tripathi, Divya & Chauhan, Pratima & Rawat, Ravindra. (2023). A synergistic approach to enhance sensitivity and selectivity of room temperature operable ammonia gas sensor with humidity assistance using RGO/WO3 nanocomposite. Nanotechnology. 35. DOI:10.1088/1361-6528/ad090a.

[46] Mohammad Reza Sovizi, Somayeh Mirzakhani, highly sensitive detection of ammonia gas by 3D flower-like ɤ-MnO2 nanostructure chemiresistor, Journal of the Taiwan Institute of Chemical Engineers, Volume 111, 2020, Pages 293-301, ISSN 1876-1070, https://doi.org/10.1016/j.jtice.2020.04.017.

[47] Marimuthu Ganesan, Bharathi Ganapathi, Balaji Parasuraman, Pazhanivel Thangavelu, Sensitivity enhancement of ammonia gas sensor based on NiFe2O4/rGO nanocomposite, Chemical Physics Impact, Volume 8, 2024, 100616, ISSN 2667-0224, https://doi.org/10.1016/j.chphi.2024.100616.

[48] Jeevitha G, Abhinayaa R, Mangalaraj D, Ponpandian N, Meena P, Mounasamy V, Madanagurusamy S. Porous reduced graphene oxide (rGO)/WO_3 nanocomposites for the enhanced detection of NH_3 at room

temperature. Nanoscale Adv. 2019 Feb 27;1(5):1799-1811. doi: 10.1039/c9na00048h.

[49] H. Zhang, Y. Li, Z. Yuan, Y. Lei, X. Li and F. Meng, "Enhanced Ammonia Sensing Performance Based on FeCo2O4/WO3/rGO Ternary Nanocomposites," in *IEEE Sensors Journal*, vol. 23, no. 21, pp. 25698-25707, 1 Nov.1, 2023, doi: 10.1109/JSEN.2023.3318210.

[50] Marimuthu Ganesan, Bharathi Ganapathi, Palanisamy Govindasamy, Balaji Parasuraman, Paramasivam Shanmugam, Rajender Boddula, Ramyakrishna Pothu, Pazhanivel Thangavelu, CoFe2O4/rGO nanocomposite: Synthesis and enhanced ammonia gas sensing properties at room temperature, Results in Chemistry, Volume 7, 2024, 101342, ISSN 2211-7156, https://doi.org/10.1016/j.rechem.2024.101342.

[51] Alouani, M.A.; Casanova-Cháfer, J.; Güell, F.; Peña-Martín, E.; Ruiz-Martínez-Alcocer, S.; de Bernardi-Martín, S.; García-Gómez, A.; Vilanova, X.; Llobet, E. ZnO-Loaded Graphene for NO_2 Gas Sensing. *Sensors* **2023**, *23*, 6055. https://doi.org/10.3390/s23136055

[52] Ahmad Umar, Ahmed A. Ibrahim, R. Kumar, H. Albargi, Wen Zeng, Mohsen Ali M. Alhmami, Mabkhoot A. Alsaiari, S. Baskoutas, Gas sensor device for high-performance ethanol sensing using α-MnO_2 nanoparticles, Materials Letters, Volume 286, 2021, 129232, ISSN 0167-577X, https://doi.org/10.1016/j.matlet.2020.129232.

[53] Shyamasree Gupta Chatterjee, Somenath Chatterjee, Ajoy K. Ray, Amit K. Chakraborty, Graphene–metal oxide nanohybrids for toxic gas sensor: A review, Sensors and Actuators B: Chemical, Volume 221, 2015, Pages 1170-1181, ISSN 0925-4005, https://doi.org/10.1016/j.snb.2015.07.070.

[54] Zhang, Dongzhi and Liu, Aiming and Chang, Hongyan and Xia, Bokai, Room-temperature high-performance acetone gas sensor based on hydrothermal synthesized SnO2-reduced graphene oxide hybrid composite, RSC Adv., 2015 , Volume 5, issue 4, 3016-3022, DOI: 10.1039/C4RA10942B

[55] Xiao, Xue & Jin, Wei & Tang, Cao & Qi, Xin & Li, Rui & Zhang, Yi & Zhang, Wusheng & Yu, Xue & Zhu, Xiaodong & Ma, Yanqing & Ma, Lei. (2023). Thermal reduced graphene oxide-based gas sensor for rapid detection of ammonia at room temperature. Journal of Materials Science. 58. 1-13. 10.1007/s10853-023-08696-w.

[56] Lv, C.; Hu, C.; Luo, J.; Liu, S.; Qiao, Y.; Zhang, Z.; Song, J.; Shi, Y.; Cai, J.; Watanabe, A. Recent Advances in Graphene-Based Humidity Sensors. *Nanomaterials* **2019**, *9*, 422. https://doi.org/10.3390/nano9030422. PMID: 30871077; PMCID: PMC6474033.

[57] Casanova-Cháfer, J.; Navarrete, E.; Noirfalise, X.; Umek, P.; Bittencourt, C.; Llobet, E. Gas Sensing with Iridium Oxide Nanoparticle Decorated Carbon Nanotubes. *Sensors* **2019**, *19*, 113. https://doi.org/10.3390/s19010113.

Supporting information of the Publications not included in this thesis

The effect of doping rGO with MnO_2 nanomaterial on its gas sensing properties.

M.A. Alouani[1-2-3], J. Casanova-Chafer[1-2-3], S. de Bernardi-Martín[4]; A. García-Gómez[4] F. Salehnia[1-2-3], J.C. Santos-Ceballos[1-2-3], A. Santos-Betancourt[1-2-3], X. Vilanova[1-2-3] * and E. Llobet[1-2-3]*

[1]Universitat Rovira i Virgili, MINOS, School of Engineering, Avda. Països Catalans 26, 43007 Tarragona, Spain

[2]IU-RESCAT, Research Institute in Sustainability, Climatic Change and Energy Transition, Universitat Rovira i Virgili, Joanot Martorell 15, 43480 Vila-seca, Spain

[3]TecnATox - Centre for Environmental, Food and Toxicological Technology, Universitat Rovira i Virgili, Avda. Països Catalans 26, 43007 Tarragona, Spain

[4]Gnanomat. C/Faraday 7, 28049 Madrid, Spain

*Corresponding authors e-mails: xavier.vilanova@urv.cat; eduard.llobet@urv.cat

XRD for rGO@MnO_2:

To identify the crystalline phase of the manganese oxide present on the powders synthesized, an XRD analysis was conducted via a Bruker D8-DISCOVER (Germany). The diffractogram is shown in Figure S1. The diffractogram can be interpreted using the JCPDS card no. 00-065-1528 for rGO and JCPDS card no. 00-042-116, confirming that manganese oxide is MnO_2.

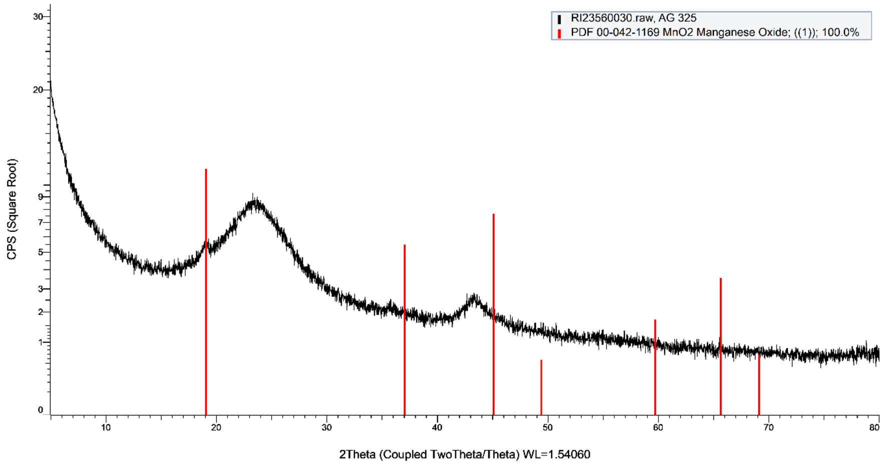

Figure S1. XRD diffractogram of rGO@MnO_2 powder showing the presence and crystalline phase of manganese oxide.

EDS for rGO@MnO_2 deposited on silicon substrate:

A qualitative and semi-quantitative analysis performed on the surface of the rGO@MnO_2 deposited on silicon substrate via the energy dispersive spectroscopy (EDS) technique, the results obtained shown in the spectrum of the analysis. Quantitatively, carbon and oxygen have the strongest peaks since carbon is coming from the graphene layer, oxygen is abundant on the surface of the studied area, and silicon have a weak peak coming from the substrate which the layers were deposited on top. The Si peak is weak because of the parameters used for the EDS analysis. Mn element also has a weak peak since its concentration on the surface is too low especially in a small chosen area but still it was proven to be present with an atomic % of 3.28%. The presence of sulfur, Na and Cl peaks can be attributed to an analysis error since this method is not completely accurate.

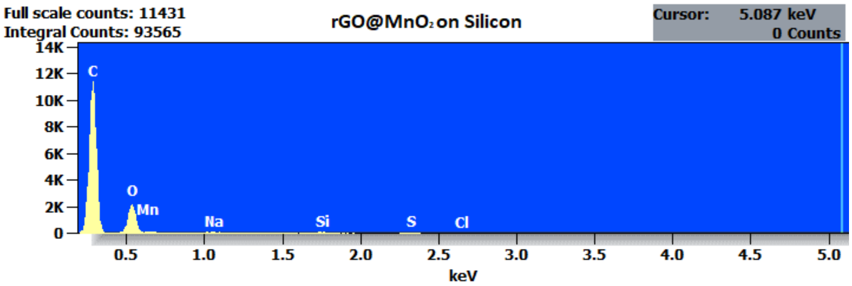

Figure s2. The extracted spectrum from the EDS analysis.

Table S1. Characteristics of the elements present in the studied sensitive layer.

Element	*Weight %*	*Weight % Error*	*Norm. Wt.%*	*Atom %*	*Formula*
C	53.43	± 0.27	53.43	66.79	C
O	28.74	± 0.36	28.74	26.97	O
Na	0.68	± 0.08	0.68	0.45	Na
Si	2.17	± 0.12	2.17	1.16	Si
S	1.90	± 0.18	1.90	0.89	S
Cl	1.10	± 0.23	1.10	0.46	Cl
Mn	11.99	± 1.39	11.99	3.28	Mn
Total	100.00		100.00	100.00	

EDS for rGO@MnO$_2$ deposited on Kapton substrate:

Same EDS analysis was performed on the surface of the rGO@MnO$_2$ deposited on Kapton sensor. Since the materials are the same, we have again carbon and oxygen with the strongest peaks, Mn with a very weak peak and atom % of 3.66 %. Sulfur element was found again and can be an analysis error.

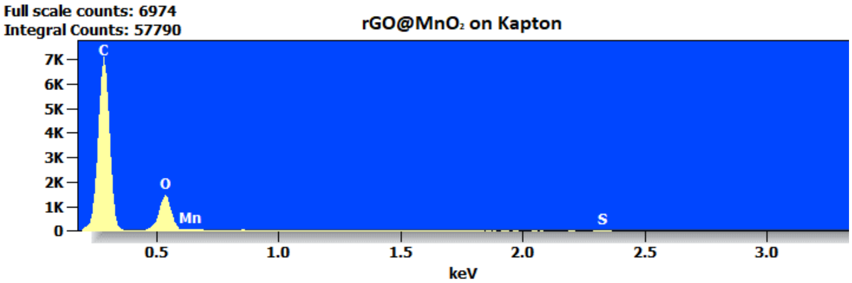

Figure s3. The extracted spectrum from the EDS analysis for rGO@MnO_2 on Kapton

Table S2. Characteristics of the elements present in the studied sensitive layer.

Element	*Weight %*	*Weight % Error*	*Norm. Wt.%*	*Atom %*	*Formula*
C	52.94	± 0.29	52.94	65.66	C
O	32.32	± 0.48	32.32	30.09	O
S	1.26	± 0.23	1.26	0.59	S
Mn	13.48	± 1.96	13.48	3.66	Mn
Total	100.00		100.00	100.00	

UNIVERSITAT
ROVIRA i VIRGILI